REPORT DOCUMENTATION PAGE

Form Approved OMB NO. 0704-0188

The public reporting burden for this collection of information is estimated to average 1 hour per response, including the time for reviewing instructions, searching existing data sources, gathering and maintaining the data needed, and completing and reviewing the collection of information. Send comments regarding this burden estimate or any other aspect of this collection of information, including suggesstions for reducing this burden, to Washington Headquarters Services, Directorate for Information Operations and Reports, 1215 Jefferson Davis Highway, Suite 1204, Arlington VA, 22202-4302. Respondents should be aware that notwithstanding any other provision of law, no person shall be subject to any oenalty for failing to comply with a collection of information if it does not display a currently valid OMB control number.
PLEASE DO NOT RETURN YOUR FORM TO THE ABOVE ADDRESS.

1. REPORT DATE (DD-MM-YYYY)	2. REPORT TYPE	3. DATES COVERED (From - To)
10-01-2013	Final Report	15-Aug-2009 - 28-Feb-2013

4. TITLE AND SUBTITLE	5a. CONTRACT NUMBER
Final Report of work for Hierarchical Engineered Materials and Structures	W911NF-09-1-0380
	5b. GRANT NUMBER
	5c. PROGRAM ELEMENT NUMBER 622618
6. AUTHORS Anthony M. Waas	5d. PROJECT NUMBER
	5e. TASK NUMBER
	5f. WORK UNIT NUMBER

7. PERFORMING ORGANIZATION NAMES AND ADDRESSES	8. PERFORMING ORGANIZATION REPORT NUMBER
University of Michigan - Ann Arbor Regents of the University of Michigan 3003 S. State St Ann Arbor, MI 48109 -1274	
9. SPONSORING/MONITORING AGENCY NAME(S) AND ADDRESS(ES)	10. SPONSOR/MONITOR'S ACRONYM(S) ARO
U.S. Army Research Office P.O. Box 12211 Research Triangle Park, NC 27709-2211	11. SPONSOR/MONITOR'S REPORT NUMBER(S) 56026-EG.2

12. DISTRIBUTION AVAILIBILITY STATEMENT

Approved for Public Release; Distribution Unlimited

13. SUPPLEMENTARY NOTES

The views, opinions and/or findings contained in this report are those of the author(s) and should not contrued as an official Department of the Army position, policy or decision, unless so designated by other documentation.

14. ABSTRACT

This project is concerned with a new class of light-weight, hierarchical engineered material systems designed to mitigate effects due to high intensity short duration loads, such as blast. A fundamental research program that combines elements of experiments, analysis and the conception of novel numerical tools to tackle several challenging issues are described. The proposed work will be focused on engineered materials and structures that are exposed to

15. SUBJECT TERMS

High Speed Cameras, Fracture, Honeycombs, Crushing, Dynamic, Imaging, Digital, Correlation

16. SECURITY CLASSIFICATION OF:			17. LIMITATION OF ABSTRACT	15. NUMBER OF PAGES	19a. NAME OF RESPONSIBLE PERSON
a. REPORT	b. ABSTRACT	c. THIS PAGE			Anthony Waas
UU	UU	UU	UU		19b. TELEPHONE NUMBER 734-764-8227

Standard Form 298 (Rev 8/98)
Prescribed by ANSI Std. Z39.18

Report Title

Final Report of work for Hierarchical Engineered Materials and Structures

ABSTRACT

This project is concerned with a new class of light-weight, hierarchical engineered material systems designed to mitigate effects due to high intensity short duration loads, such as blast. A fundamental research program that combines elements of experiments, analysis and the conception of novel numerical tools to tackle several challenging issues are described. The proposed work will be focused on engineered materials and structures that are exposed to loads of high intensity and short duration. As a result, the design of the material will occur simultaneously with the design of the structure. The overarching issues this research addresses are the lack of fundamental understanding of the response of a structure made of a combination of materials and structural concepts (multi-material structures) at high strain rates. Towards achieving this goal, the static and dynamic response of honeycombs and filled honeycombs ave been studied. The filler material chosen is a elastomer. Several new results have been obtained as shown in the contents of this final report and these results shed new light on the utility of filled honeycombs as efficient energy absorbers under dynamic crush conditions.

Enter List of papers submitted or published that acknowledge ARO support from the start of the project to the date of this printing. List the papers, including journal references, in the following categories:

(a) Papers published in peer-reviewed journals (N/A for none)

Received Paper

TOTAL:

Number of Papers published in peer-reviewed journals:

(b) Papers published in non-peer-reviewed journals (N/A for none)

Received Paper

TOTAL:

Number of Papers published in non peer-reviewed journals:

(c) Presentations

1) L. Hansen, S. Guntupalli, R.J. D'Mello, A. Salvi and A. Waas, "The Effects of Defects and Loading Rate on the Compressive Crushing Response of Honeycombs", ASME International Congress, 2010, Vancouver, BC.
2) Royan J. D'Mello, Sophia Guntupalli and Anthony M. Waas, "Response of honeycombs to crush loading," ASME Applied Mechanics and Materials Division Conference (McMAT), May 30th to June 1st, Chicago, IL, 2011. (Abstract Accepted)

3) Sophia Guntupalli, Royan J. D'Mello, Amit Salvi, Lucas R. Hansen and Anthony M. Waas, "The effects of defects and loading rate on the compressive crushing response of honeycombs," ASME International Mechanical Engineering Congress and Exposition, Nov 12 – 18, 2010, Vancouver, B.C.

4) Royan J. D'Mello, Sophia Guntupalli and Anthony M. Waas, "Response of honeycombs to crush loading," ASME Applied Mechanics and Materials Division Conference (McMAT), May 30th to June 1st, Chicago, IL, 2011.

5) D'Mello R. J. and Waas A. M., "Synergistic energy absorption in the axial static compressive response of filled honeycombs," EMI/PMC, Notre Dame, June 17–20, 2012.

6) D'Mello R. J and Waas A. M., "Synergistic energy absorption in the in-plane static compression response of filled honeycombs," ACMSM 22, Sydney, Australia, December 11–14, 2012.

Number of Presentations: 6.00

Non Peer-Reviewed Conference Proceeding publications (other than abstracts):

Received Paper

TOTAL:

Number of Non Peer-Reviewed Conference Proceeding publications (other than abstracts):

Peer-Reviewed Conference Proceeding publications (other than abstracts):

Received Paper

TOTAL:

Number of Peer-Reviewed Conference Proceeding publications (other than abstracts):

(d) Manuscripts

Received		Paper
03/12/2010	1.00	P. podsiadlo, M. Qin, M. Cuddihy, J. Zhu, K. Critchley, E. Kheng, A. Kaushik, Y. Qi, H. Kim, S. Noh, E. Arruda, A. Waas, N. Kotov. Highly Ductile Multilayered Films by Layer-by-Layer Assembly of Oppositely Charged Polyurethanes for Biomedical Applications, (08 2009)

TOTAL: 1

Number of Manuscripts:

Books

Received	Paper

TOTAL:

Patents Submitted

Patents Awarded

Awards

1) Royal Aeronautical Society Literature Award (Silver Award 2012) for paper, " Ng, W., Friedmann P.P., Waas A.M., and McNamara, J.J., Thermomechanical behavior of a damaged thermal protection system: experimental correlation and influence of hypersonic flow, The Aeronautical Journal, Vol 115, No 1165 pp 69-82, 2011".
2) Ted Kennedy Family Collaborative Research Award, CoE, University of Michigan, 2012.
3) Harry and Lois Hilton Best Paper Award, AIAA 53rd SDM 2012, paper co-authored by Pineda (student) and Waas.
4) American Society of Composites Best Paper Award, AIAA 53rd SDM 2012, paper co-authored by Wang Jie (student), Hai Wang and Waas.
5) Recipient of the United States Army Director's Award for Excellence, Grad. Student Brian Justusson – summer 2011.
6) Amelia Earhart Award to Grad. Student Pavana Prabhakar, 2011.

Graduate Students

NAME	PERCENT_SUPPORTED	Discipline
Royan DMello	1.00	
FTE Equivalent:	**1.00**	
Total Number:	**1**	

Names of Post Doctorates

NAME	PERCENT_SUPPORTED
FTE Equivalent:	
Total Number:	

Names of Faculty Supported

NAME	PERCENT_SUPPORTED	National Academy Member
Anthony Waas	0.05	
FTE Equivalent:	**0.05**	
Total Number:	**1**	

Names of Under Graduate students supported

NAME	PERCENT_SUPPORTED
FTE Equivalent:	
Total Number:	

Student Metrics

This section only applies to graduating undergraduates supported by this agreement in this reporting period

The number of undergraduates funded by this agreement who graduated during this period:	0.00
The number of undergraduates funded by this agreement who graduated during this period with a degree in science, mathematics, engineering, or technology fields:.....	0.00
The number of undergraduates funded by your agreement who graduated during this period and will continue to pursue a graduate or Ph.D. degree in science, mathematics, engineering, or technology fields:.....	0.00
Number of graduating undergraduates who achieved a 3.5 GPA to 4.0 (4.0 max scale):	0.00
Number of graduating undergraduates funded by a DoD funded Center of Excellence grant for Education, Research and Engineering:	0.00
The number of undergraduates funded by your agreement who graduated during this period and intend to work for the Department of Defense	0.00
The number of undergraduates funded by your agreement who graduated during this period and will receive scholarships or fellowships for further studies in science, mathematics, engineering or technology fields:	0.00

Names of Personnel receiving masters degrees

NAME
S. Guntupalli
L. Hansen
R. D'Mello
Total Number: 3

Names of personnel receiving PHDs

NAME
Total Number:

Names of other research staff

NAME	PERCENT SUPPORTED
FTE Equivalent:	
Total Number:	

Sub Contractors (DD882)

Inventions (DD882)

Scientific Progress

report is attached

Technology Transfer

Hierarchical Engineered Materials and Structures

Composites Structures Laboratory
Department of Aerospace Engineering
University of Michigan, Ann Arbor, MI 48109-2140

ARO Number: W911NF-09-1-0380

Final report

Date: November 30, 2012

Researcher(s)

Faculty:

1. Anthony M. Waas, PI
   Felix Pawlowski Collegiate Professor of Aerospace Engineering
   Professor of Mechanical Engineering
   University of Michigan - Ann Arbor
   Ph: (734)-764-8227, Email: dcw@umich.edu

Student(s):

1. Royan J. D'Mello
   Graduate Student Research Assistant
   Department of Aerospace Engineering
   University of Michigan - Ann Arbor
   Ph: (734)-660-0612, Email: rjdmello@umich.edu

Former Student(s):

1. Sophia Guntupalli
   Graduate Student
   Department of Aerospace Engineering
   University of Michigan - Ann Arbor
   Ph: (734)-660-9690, Email: gsophia@umich.edu

2. Lucas R. Hansen
   Graduate Student Research Assistant
   Department of Aerospace Engineering
   University of Michigan - Ann Arbor
   Ph: (517)-980-5210, Email: lrhansen@umich.edu

Abstract

This project is concerned with a new class of light-weight, hierarchical engineered material systems designed to mitigate effects due to high intensity short duration loads, such as blast. A fundamental research program that combines elements of experiments, analysis and the conception of novel numerical tools to tackle several challenging issues are described. The proposed work will be focused on engineered materials and structures that are exposed to loads of high intensity and short duration. As a result, the design of the material will occur simultaneously with the design of the structure. The overarching issues this research addresses are the lack of fundamental understanding of the response of a structure made of a combination of materials and structural concepts (multi-material structures) at high strain rates. Towards achieving this goal, the static and dynamic response of honeycombs and filled honeycombs ave been studied. The filler material chosen is a elastomer. Several new results have been obtained as shown in the contents of this final report and these results shed new light on the utility of filled honeycombs as efficient energy absorbers under dynamic crush conditions.

Contents

1 Introduction **9**

2 Static in-plane crush response of honeycomb **13**
2.1 Introduction 13
2.2 Static experiments 13
2.3 Quasi static experiments with defects 17
2.4 Defects: Symmetric defects 17
2.5 Defects: Asymmetric defects 18
2.5.1 Type I defect 19
2.5.2 Type II defect 23

3 Dynamic out-of-plane crush response of honeycomb **30**
3.1 Introduction 30
3.2 Review of static out-of-plane crushing 34
3.3 Test Preparation 37
3.3.1 Honeycomb Dimensions 37
3.3.2 Polycarbonate elastic properties & static axial crush load 38
3.3.3 Measurement of experimental data 39
3.4 Experiments: Wave loading device (WLD) method 40
3.4.1 Setup & Procedure 40
3.4.2 Results 43
3.5 Experiments: Direct impact method 44
3.5.1 Setup & Procedure 44
3.5.2 Results 46
3.6 Finite Element Model 51
3.6.1 Introduction 51
3.6.2 Eigenbuckling Analysis 52
3.7 Dynamic Crush Simulation 54
3.7.1 Introduction 54
3.7.2 Simulation Results and Discussion: Wave loading device (WLD) method 56
3.7.3 Simulation Results and Discussion: Direct impact method 57
3.7.4 Variation of local strain rates and plateau stress with crush velocity . . 61
3.8 Conclusions 63

4 Static out-of-plane crush response of filled honeycomb 66
4.1 Introduction . . . 66
4.2 Sample preparation & test setup . . . 68
4.3 Experiments: Polyurethane as the Filler Material . . . 69
4.3.1 Static Uniaxial Compression of Polyurethane . . . 69
4.3.2 Static crush response of filled honeycombs . . . 69
4.3.3 Load contribution of the honeycomb-infill cylinders . . . 76
4.3.4 Finite Element Simulation . . . 79
4.4 Effect of filler stiffness on the crush response . . . 86
4.4.1 Summary & Conclusion . . . 89
4.5 APPENDIX: Axial crush of filled hexagonal aluminum honeycomb . . . 90

5 Static inplane crush response of circular cell honeycomb filled with elastomer 94
5.1 Introduction . . . 94
5.2 Material Properties . . . 96
5.2.1 Polycarbonate properties . . . 96
5.2.2 Filler Properties . . . 96
5.3 Inplane crushing of unfilled honeycomb . . . 97
5.3.1 Inplane crush response of filled honeycomb . . . 99
5.3.2 Introduction . . . 99
5.3.3 Pre-failure regime . . . 101
5.3.4 Failure regime . . . 101
5.3.5 Synergistic response . . . 103
5.4 Digital image correlation study . . . 105
5.4.1 Introduction . . . 105
5.4.2 Stage I: Initial up to pre-failure regime . . . 106
5.4.3 Stage II: In the vicinity of first failure . . . 107
5.5 Finite element simulation of the experiment . . . 110
5.5.1 Model Description . . . 110
5.5.2 Application of the Smeared Crack Approach . . . 112
5.5.3 Simulation Results . . . 114
5.6 Conclusion . . . 119

6 Summary & Future Work 121

List of Figures

2.1 Schematic of honeycomb and in-plane direction 14
2.2 Plot showing static crush response of a 10×10 sized honeycomb. The four stages of crushing are also shown. 15
2.3 Defining parameters of interest in the study are shown. 16
2.4 Influence of fraction of cells removed on δP and energy absorbed 16
2.5 Honeycomb with Type I defect 19
2.6 Load response and deformation pattern for $e = 0$ 20
2.7 Load response and deformation pattern for $e = 1$ 20
2.8 Load response and deformation pattern for $e = 3$ 21
2.9 Load response and deformation pattern for $e = 5$ 21
2.10 Load response and deformation pattern for $e = 7$ 21
2.11 Load response and deformation pattern for $e = 9$ 22
2.12 Load response and deformation pattern for $e = 11$ 22
2.13 Load response and deformation pattern for $e = 13$ 22
2.14 Summary of response of honeycomb with type I defects 24
2.15 Honeycomb with Type II defect 24
2.16 Load response and deformation pattern for $e = 0$ 25
2.17 Load response and deformation pattern for $e = 1$ 26
2.18 Load response and deformation pattern for $e = 3$ 26
2.19 Load response and deformation pattern for $e = 5$ 26
2.20 Load response and deformation pattern for $e = 7$ 27
2.21 Load response and deformation pattern for $e = 9$ 27
2.22 Load response and deformation pattern for $e = 11$ 27
2.23 Load response and deformation pattern for $e = 13$ 28
2.24 Summary of response of honeycomb with type II defects 29

3.1 Diagram of the 3 and 7-cell circular polycarbonate honeycomb. 31
3.2 Sketch of honeycomb specimen under displacement controlled loading (left). The macroscopic stress-strain response shows a prominent peak and a lengthy plateau region (center). Localized concertina-diamond buckling mode seen in the deformed specimen (right). 35

3.3 The macroscopic maximum stress and plateau stress shown for varying number of cell number N (left). The number of symmetry axes for 3-cell and 7-cell specimens (right). (Mellquist & Waas, 2004) 35
3.4 An imperfection seeded mesh of a 7 cell specimen (left). The deformed structure obtained from static Riks crush simulation with concertina-diamond mode of deformation (right). (Mellquist & Waas, 2004) 36
3.5 Micro-section of the contact site of two cells in the polycarbonate honeycombs as seen under an optical microscope. 38
3.6 Schematic showing the experimental setup of the wave loading device (WLD) . The honeycomb specimen is positioned between the incident bar and the end cap of the force sensor. 41
3.7 Typical rest-ramp displacement of the incident bar at the specimen end. The time interval ΔT_{EXP} for two successive ramp motion is shown. As the stress waves get weaker as time progresses, the velocity of the specimen end of the incident bar tends to that of the rigid body motion of the incident bar. 43
3.8 Plot showing the initial deformation response of the 3-cell specimen under dynamic crush loading using the WLD method. Load-time plot (top) and ramp-rest displacement of the transmitter bar (bottom). Observe that the crushing takes place during successive ramping phases. The first ramp ends at t = 0.14 milliseconds (ms). The load at time t = 0, t = 0.2 ms, t = 0.4 ms, t = 0.6 ms, t = 0.8 ms, t = 0.12 ms and t = 0.14 ms is shown in green (top). 45
3.9 Images of the initial stages of deformation in a 3-cell specimen loaded in the WLD setup from t = 0 to t = 0.2 ms. The last image shows the deformed state of the specimen at a later time t = 5.2 ms. In this sample, crushing took place with folds progressively forming at either ends of the specimen 46
3.10 Plot showing the initial deformation response of the 7-cell specimen under dynamic crush loading using the WLD setup. Load-time plot (top) and ramp-rest displacement of the transmitter bar (bottom). Observe that the crushing takes place during successive ramping phases. The first ramp ends at t = 0.14 milliseconds (ms). The load at time t = 0, t = 0.2 ms, t = 0.4 ms, t = 0.6 ms, t = 0.8 ms, t = 0.12 ms and t = 0.14 ms is shown in green (top). 47
3.11 Images of the initial stages of deformation in a 7-cell specimen loaded in the WLD setup from t = 0 to t = 0.2 ms. The last image shows the deformed state of the specimen at a later time t = 4.2 ms. In this sample, crushing took place with folds progressively forming at either ends of the specimen 48
3.12 Schematic showing the setup for the direct impact method. The honeycomb specimen is positioned sufficiently close to and directly in front of the striker bar. The specimen is bonded to the end cap of the force sensor. 48
3.13 Load-time plot of the 3-cell specimen when impacted directly by the striker bar. The first fold occurs at the impact end and clear peak is observed at 0.1 ms. The fold formation continues progressively from the impact end of the specimen as the striker bar crushes the specimen. 50

3.14 Load-time plot of a 3-cell specimen when directly impacted by a striker bar. There is no prominent peak. The first fold starts soon after the linear region ends (t = 0.07 ms) at the far end of the specimen. Folds continue to form progressively from the far end of the specimen. 50
3.15 Load-time plot of a 7-cell specimen when directly impacted by a striker bar. The first fold starts soon after the linear region ends (t = 0.07 ms) at the far end of the specimen. Folds continue to form progressively from the far end of the specimen. 51
3.16 Diagram showing the boundary conditions used on the honeycomb during eigenbuckling analysis. These boundary conditions are also used for crush simulations. x_1, y_1 and z_1 are the local shell co-ordinates on a single cell corresponding to axial (u), circumferential (v) and radial (w) displacements. x_G, y_G and z_G are the global co-ordinates for the model. 52
3.17 Eigenmodes for 3-cell and 7-cell honeycomb models that are chosen to perturb the mesh for explicit FE simulations. Mode A corresponds to the lowest eigenmode and Mode B is chosen corresponding to higher buckling load. 54
3.18 The rate dependent compressive behavior of polycarbonate taken from Mulliken & Boyce (2006). Note the two regions where polycarbonate exhibits different rate dependent behavior. 55
3.19 Images from the FE dynamic crush simulation of 3-cell and 7-cell models with WLD inputs. The folds appear soon after the peak load is attained. The collapse occurs through the localized concertina-diamond mode. 58
3.20 Load-time plot for 7-cell specimen FE simulation with the ramp-rest WLD input. The mean plateau load level (120 N) for static crush of 7-cell honeycomb is shown for comparison. 58
3.21 Images from the FE dynamic crush simulation of 3-cell and 7-cell models with loading velocity 5,000 mm/s (DIM simulation). Crushing occurs through the concertina-diamond mode. 60
3.22 Load-time plot obtained from FE simulation for 7-cell specimen being crushed at the rate of 5,000 mm/s (DIM simulation). The mean plateau load level (120 N) for static crush of 7-cell honeycomb is shown for comparison. 60
3.23 Plot showing the FE simulated crush and peak load values that are normalized by number of cells for 3-cell, 4-cell, 7-cell, 13-cell and 19-cell specimens. Each of the specimens were crushed at the rate of 5,000 mm/s (DIM simulation) to study the effect of cells-per-specimen on the crush and peak load. 62
3.24 Plot showing the variation of material strain rate and normalized plateau load per cell with crush velocity for 3 and 7-cell models. For crush velocity of 5,000 mm/s (Direct impact method), the experimental normalized plateau stresses for the 3 and 7-cell are also shown. The normalized plateau stress, a non-dimensional quantity, is calculated as $P_{plateau}/NAE$ where $P_{plateau}$ is the plateau load, $A = 2\pi Rt$ is the true contact area and E is the polycarbonate Young's modulus for an N-cell honeycomb. Also shown is the normalized plateau stress for 3-cell and 7-cell static crush experiments. 63
3.25 Plot showing the load response for the outer cell for a 3-cell model and outer and innermost cells in 7-cell model and pointing towards the influence of lateral constraints at the double-wall site on the plateau load. 64

4.1 Schematic of a 3-cell specimen showing the cell length (L), wall thickness (t) and cell diameter (D) is shown to the left. The out-of-plane loading direction is in the 3-direction. The double wall contact over a line is shown in a diagram to the right. . . 67
4.2 Cross section of the 3-cell, 7-cell and 19-cell specimens filled with polyurethane. . . . 68
4.3 Image sequence taken from the quasi-static uniaxial compression test of polyurethane block corresponding to macroscopic strains of 0, 0.22, 0.48 and 0.70. 69
4.4 Load-deflection curve of polyurethane sample undergoing compression loading followed by unloading. 70
4.5 Load response of a filled 3-cell specimen shown against that of an unfilled 3-cell specimen. The crush response of the polyurethane block is also shown. 71
4.6 Load response of a filled 7-cell specimen shown against that of an unfilled 3-cell specimen. The crush response of the polyurethane block is also shown. 72
4.7 Load response of a filled 19-cell specimen shown against that of an unfilled 3-cell specimen. The crush response of the polyurethane block is also shown. 73
4.8 The green curve shows the response of the polyurethane block added to the response of the 3-cell unfilled honeycomb. The shaded portion shows synergy in load response for the filled specimen. 75
4.9 The green curve shows the response of the polyurethane block added to the response of the 7-cell unfilled honeycomb. The shaded portion shows synergy in load response for the filled specimen. 76
4.10 The green curve shows the response of the polyurethane block added to the response of the 19-cell unfilled honeycomb. The shaded portion shows synergy in load response for the filled specimen. 77
4.11 The images comparing the deformations of filled and unfilled 7-cell and 19-cell honeycombs. The unfilled specimens are shown on the left column and the filled specimens on the right column. Notice the progressive localized failure spread over a continuous region in the unfilled specimens. In contrast, the localized folds in the filled specimens occur in a random fashion. Longitudinal tearing is seen in both the filled honeycombs. In the filled 7-cell specimen, notice some global deformation that is not present in the filled 19-cell specimen due to lower aspect ratio. 78
4.12 Plot showing the normalized load response of honeycomb-infill cylinder for a 3-cell, 7-cell and 19-cell specimens. The normalized load per cell for the corresponding unfilled honeycomb is also shown. 80
4.13 The finite element mesh (top view), showing the honeycomb filled with polyurethane (Inner Fill) and surrounding it (Outer Fill). The space formed where three cells meet is not filled to make the explicit crush simulation more computationally affordable by reducing the surface-to-surface constraints. 81
4.14 Plot showing the comparison of the load response of 7-cell honeycomb experiments and finite element simulation for both filled and unfilled honeycombs. 83

4.15 Deformation of filled and unfilled 7-cell honeycombs obtained from explicit finite element simulation. The folding in the filled model is more spread out in a random fashion compared to the unfilled model where the failure is localized near an end. Also, the filled model shows cells deforming globally and this behavior is not present in the unfilled specimen. Overall, the deformations seen for filled and unfilled models are in good agreement with the deformation observed from experimental images. 85
4.16 Finite element model of the filled honeycomb (left). Nominal stress vs. strain curves of elastomers considered in the study. The curve B corresponds to polyurethane and curve D corresponds to PDMS. 87
4.17 Load response of filled honeycomb with varying elastomeric properties and corresponding response of an equal sized elastomer. 87
4.18 Load carried by the honeycomb during the axial crushing of the filled honeycomb for varying filler stiffness 88
4.19 The mode of collapse in the honeycomb for the five cases considered. 88
4.20 Load-deflection plot of 7-cell filled and unfilled hexagonal aluminum honeycomb. The load response plot of PDMS is also shown for comparison. 91
4.21 Image showing first fold formation at first peak (center) and localized folding (right) at the bottom of the specimen, beyond the peak in the unfilled honeycomb experiment. . 91
4.22 Image showing first fold formation at first peak (center) and diffused folding (right) beyond the peak in the filled honeycomb experiment. 91
4.23 Plot showing the synergistic response of the filled honeycomb. The end-shortening value (Δ_C) is at the end of the plateau region, where filled load response rises with further increase in end-shortening. 93

5.1 Sketch of a 11×11 size circular cell honeycomb (left). Details of the microsection with relevant dimensions, R: cell radius, t: wall thickness, L: cell length, t_d: double-wall thickness, L_d: bond length (right). 95
5.2 Load vs. displacement curve for PDMS cylindrical block along with images during compression. 97
5.3 Load-displacement plot obtained from the static inplane compression of an 11×11 size unfilled honeycomb specimen. 98
5.4 Row-wise collapse (right) mode in inplane compression of unfilled honeycomb (left). 99
5.5 Load vs. displacement plot of the compression response of 11×11 size filled honeycomb. Also shown is the load response of a PDMS block of identical size. To make a comparison, the plateau load in the 11×11 size unfilled honeycomb is approximately 42 N. 100
5.6 Undeformed filled specimen (left). Image prior to first failure showing first and second localization sites (right). Notice the ovalization in the cells (right). . . . 102
5.7 Images showing the first localization site prior to localization (left) and at the onset of localization (right). 102
5.8 Specimen unloaded immediately after catastrophic failure. Notice the global shear-like failure to the left. 103

5.9 Tables comparing some average statistics between the unfilled and the filled honeycomb specimens under static inplane loading. 104
5.10 Displacement field along the x-direction. 107
5.11 Normal strain field along the x-direction. 108
5.12 Normal strain field along the y-direction. 108
5.13 Shear strain field showing diagonal band formation. 109
5.14 Shear strain field at first failure. The arrows show sense of rotation of two adjacent rows near the failure site. 109
5.15 Finite element model of the filled honeycomb specimen is shown along with the top loading plate and bottom plate (left). The portion of the front view (right) . 110
5.16 Stress strain curve for polycarbonate (Ref: Mulliken & Boyce, 2006) shown against exponential curve fit for the plastic part to be used in SCA model. Also shown is the critical stress value σ_{cr} = 55 MPa, and exponential softening curve that is a function of Mode I fracture toughness G_{IC}. 113
5.17 Schematic showing 11×11 honeycomb model with crack band (shown in red) being applied in Model A and Model B. 114
5.18 Load vs. displacement curve of the simulations and the experiment. Simulations for Model A is shown in red, whereas that for Model B is shown in blue. 115
5.19 Compressive normal strain (ϵ_x) map along the direction perpendicular to the direction of loading. The nature of strains along the center of the cells in the filler is tensile. 117
5.20 Normal strain (ϵ_y) map along the direction of loading. 117
5.21 Normal stress distributions S_{11} (left) and S_{22} (right) along the x and y directions respectively, for the filler located at the center of the model. Units are in MPa. 118
5.22 Image showing events (a) prior to localization (left), (b) onset of localization (right) 118
5.23 Image showing strains in the honeycomb walls (a) prior to localization (left), (b) onset of localization (right) 118

Chapter 1

Introduction

The energy absorption mechanism of lightweight cellular materials (such as honeycombs and foams) which are commonly used in "hierarchically designed" structural materials, especially at high loading rates, are the subject of this ARO sponsored project. When cellular materials are used as a multi-material structural composite, core crushing and transverse shearing comes into play thus contributing to significant energy absorption. In the past, the PI and his students have developed a response model for honeycombs when subjected to in-plane and biaxial loads (see Chung & Waas, 2000, 2002a, b, c, d). In Chung & Waas, 2002a, b, c, d, circular cell polycarbonate honeycombs were subjected to in-plane static loading in the axial and biaxial loading conditions. The work reported several new results and identified key results that influence the deformation response. Several analytical studies were also carried out (Chung & Waas 2000; Chung & Waas 2002e) that energy absorption capability is related to the non-linear stress-strain response of the base material, amount of initial geometrical imperfections at the cell walls and cell packing. They have also extended their analytical work recently to model honeycombs as micropolar solids (Chung & Waas 2008). The PI has also conducted study on the static out-of-plane crush response of circular cell honeycomb (Mellquist & Waas 2002, 2004) where it was found that concertina-diamond buckling mode was controlling the plateau stress. This local-

ized collapse mode was the mechanism of energy absorption. They also found the absence of scaling effects with regard to number of cells in the honeycomb cluster undergoing crushing. In the present work, the focus is on two novel aspects relating to the overall goals of the project (a) Understanding and characterizing mechanisms of collapse of honeycombs (out-of- plane crushing) as a function of loading rate and initial geometrical imperfections, (b) Understanding the mechanism of core crushing and amplification of energy absorption as a function of loading rate and filler material in the in-plane as well in the out-of-plane directions. The work described in this report accompanies work carried out during Jan 2011 - present and is briefly described in the following:

1. Static in-plane response of honeycombs with defects

   The objective of this study was to study the influence of defects (symmetric and asymmetric) on the in-plane crush response of honeycomb. In general, the collapse initiated in the layers with defects accompanied by a load depending on the extent of defect. Thereafter, once the layers containing the defects had completely collapsed, the plateau load of the corresponding non-defective specimen was attained. This work is described in Chapter 2 of this report.

2. Dynamic out-of-plane crush response of circular polycarbonate honeycombs

   Using two dynamic loading devices conceived in our lab namely, the *Wave loading device* (WLD) and the *Direct impact method* (DIM), we have shown that the plateau stress increases with increase in loading rate when circular cell honeycombs are crushed in the out-of-plane direction. The mode of collapse was similar to the corresponding static crush response, i.e. localized concertina-diamond fold formation. The chief reason for plateau stress elevation is the rate dependency of the base material (polycarbonate). Finite element simulations incorporating the rate dependent behavior of polycarbonate agreed fairly well with the experimental mode of collapse and crush load for WLD and DIM methods. This work is described in Chapter 3.

3. Static out-of-plane crush response of filled circular polycarbonate honeycombs

   Here, polyurethane, a soft elastomer used as filler in the honeycomb. Synergistic energy absorption was observed as the mode of collapse was altered due to the presence of the filler material. The folds here were diffused as opposed to localized folding observed in unfilled out-of-plane crushing. Longitudinal wall tearing (Mode I crack) was other form of failure observed. The experimental results compared well with the finite element model with respect to mode of collapse and crush load. Synergistic effects were also observed for a different honeycomb-elastomer system, i.e. hexagonal aluminum honeycomb with PDMS as the filler material. Again, the mode of collapse was diffused folding of the "flat" cell walls. We also show load response and mode of deformation for soft to stiff elastomeric fillers. This work is reported in Chapter 4.

4. In-plane crush response of circular polycarbonate honeycombs

   Here, PDMS elastomer was used as the filler material in the honeycomb. Very high loads were attained, with filler material resisting the row-wise collapse (recall that row-wise collapse due to cell buckling is mode of collapse in an unfilled specimen) of the cells and also due to the constrained deformation of the filler material within individual cells. The failure is initiated locally due to longitudinal wall tearing (Mode I crack) that is accompanied by cell rotations in the vicinity of the tearing site. This onset of failure also reduces the stiffness. This localized failure spreads to other regions before the specimen fails catastrophically in shear (most of the dissipation occurs during this event). Digital image correlation (DIC) study has been conducted to monitor strain and displacement fields in the pre-failure and in the vicinity of first failure. This work is reported in Chapter 5.

Accomplishments

Journal Articles

1. R. J. D'Mello and A. M. Waas, "Static inplane crush response of circular cell honeycomb filled with elastomer," (In Preparation).

2. R. J. D'Mello, S. Guntupalli, L. R. Hansen and A. M. Waas, "Dynamic crush response of circular cell honeycombs," Proceedings of the Royal Society A, London, 468, pp. 2981-3005, 2012, .

3. R. J. D'Mello and A. M. Waas, "Synergistic energy absorption in the axial crush response of filled circular cell honeycombs," Composite Structures, Vol. 94, Issue 5, pp. 1669-1676, April 2012.

Conference Presentations

1. R. J. D'Mello and A. M. Waas, "Synergistic energy absorption in the axial static compressive response of filled honeycombs," ASCE EMI/PMC Joint conference, University of Notre Dame, June 17-20, South Bend, IN, 2012.

2. R. J. D'Mello and A. M. Waas, "Response of honeycombs to crush loading," ASME Applied Mechanics and Materials Division conference (McMAT), May 30-June 1, Chicago, IL, 2011.

3. S. Guntupalli, R. J. D'Mello, L. R. Hansen, A. Salvi and A. M. Waas, "Strain rate dependence on the out-of-plane compressive response of circular cell honeycombs," ASME International Congress (IMECE), Vancouver, Canada, 2010.

Conference with Proceedings

1. R. J. D'Mello and A. M. Waas, "Synergistic energy absorption in the in-plane compression response of filled honeycombs," 22nd Australasian Conference on the Mechanics of Structures and Materials (ACMSM), December 11-14, Syndey, Australia, 2012.

Chapter 2

Static in-plane crush response of honeycomb

2.1 Introduction

2.2 Static experiments

The in-plane direction of the honeycomb is defined along the 2-3 plane as shown in Figure 2.1. The honeycomb panels used in the in-plane crush response study (static and dynamic cases) were of dimensions: The single wall thickness (t) was 0.064 $\pm$ 0.005 mm, the double wall thickness was 0.133 $\pm$ 0.006 mm, the cell adhesion length was 0.237 $\pm$ 0.027 mm and the cell radius (R) was 2.108 $\pm$ 0.39 mm. The Young's modulus (E) obtained was 2600 $\pm$ 200 N/mm.

Quasi-static tests were performed in-plane ($x - y$ plane) and the setup used is shown below in Figure 2.1. The base of the specimen is kept fixed and the top face is subjected to compression loading using displacement controlled loading as schematically shown in Figure 2.1. The top face is displaced at a slow rate of 2 mm/min in an INSTRON machine. The load is measured

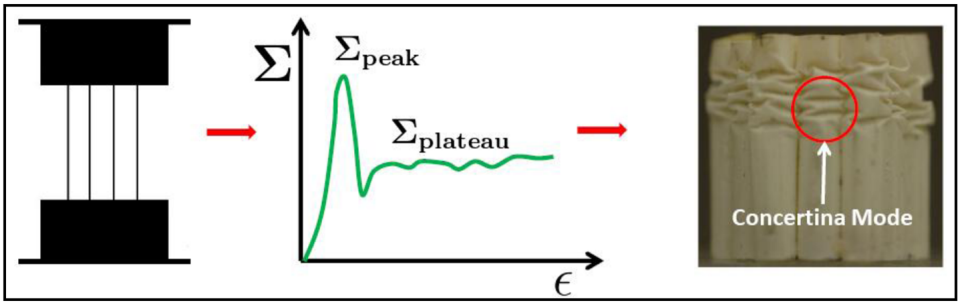

Figure 2.1: Schematic of honeycomb and in-plane direction

using a 250 lbf capacity load cell. The deformation pattern is captured using a high speed camera that takes images at 5 images per second. Tests have been performed on specimens of different sizes. The sizes are defined by the number of cells along the width (2-direction) and height (3- direction) (sizes will be defined as P $\times$ Q henceforth).

The deformation mechanisms of all the specimens has been observed to be the same, (Chung & Waas, 2002a), and can be described as follows. The specimen carries load and under goes a fairly uniform deformation until the load reaches a critical value (peak load). Up to this point, the load recorded varies linearly with the amount of displacement. When the peak load is attained, a layer of cells starts to deform more than the rest of the cell layers. This layer starts to collapse by buckling. This layer collapses by deforming into an anti-symmetric mode as shown in Figure 2.2. This causes the load to drop. As soon as one layer collapses completely, there is a slight relaxation in the specimen where all the remaining cells approximately recover their original shape. The load increases until the next collapse event takes place in the adjacent layers. This type of deformation pattern progressively continues until all the layers collapse. This results in a series of crests and troughs as seen in Figure 2.1. The average value of the near constant state of load is referred to as the plateau load. After all the layers have collapsed completely, the specimen enters the densification phase where the load increases indefinitely. For example, the load-displacement curve and the corresponding deformation pattern for a 10 $\times$ 10 specimen are shown in Figure 2.1. Here, attention is drawn to deformed shapes of the

cells and the corresponding location on the load displacement plot.

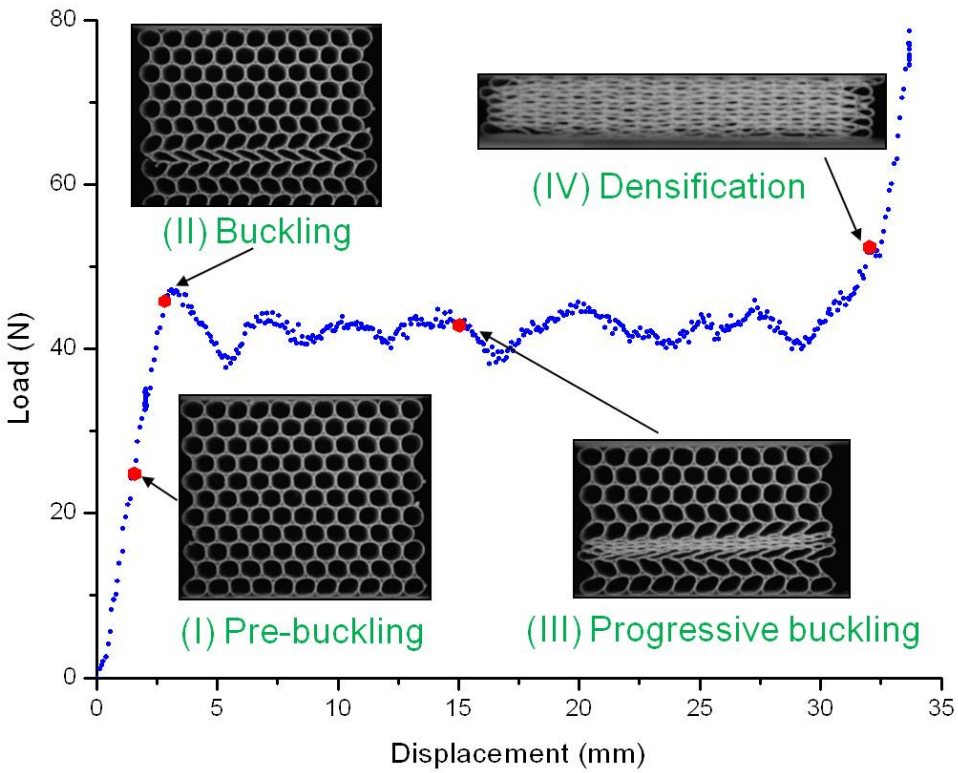

Figure 2.2: Plot showing static crush response of a 10×10 sized honeycomb. The four stages of crushing are also shown.

Similarly the tests were done on different sizes of specimens. The initial stiffness, plateau load and energy absorbed are defined as shown in Figure 2.3. Volume of the honeycomb is defined as the product of width (2 direction), height (3-direction) and cell length (1-direction) as shown in Figure 2.1. The quasi static results for all the tests carried out on various specimen sizes are reported in Table 2.1. Based on the experiments conducted we observe the following:

1. The initial stiffness of the honeycomb decreases with increase in the height of the specimen for a given width of the specimen.

2. The plateau load remains constant for different heights for a given width. Thus, it is only a function of width.

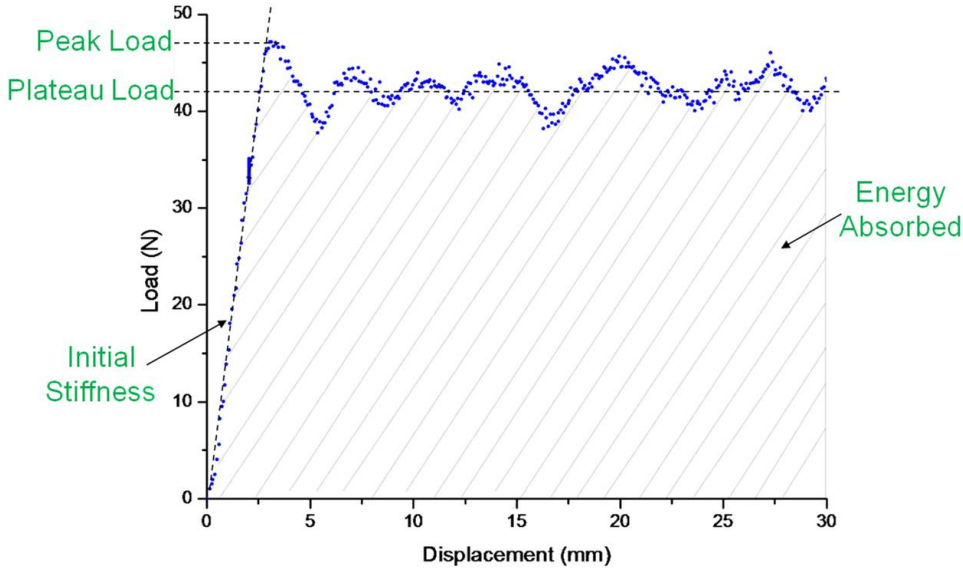

Figure 2.3: Defining parameters of interest in the study are shown.

Size (Width × Height)	Initial stiffness (N/mm)	Plateau Load (N)	Energy absorbed per volume (N/mm^3)
10×10	16.0 ± 1.34	40.88 ± 3.06	0.0337 ± 0.0024
10×20	10.2 ± 0.50	40.94 ± 0.54	0.0342 ± 0.0006
20×10	27.9 ± 0.62	81.26 ± 1.73	0.0354 ± 0.0005
20×20	20.5 ± 0.61	85.26 ± 2.56	0.0372 ± 0.0012
20×40	11.4 ± 0.50	83.89 ± 0.43	0.0378 ± 0.0005
40×20	30.6 ± 2.45	167.70 ± 4.40	0.0364 ± 0.0005

Table 2.1: Influence of specimen size on initial stiffness, plateau load and energy absorbed per volume

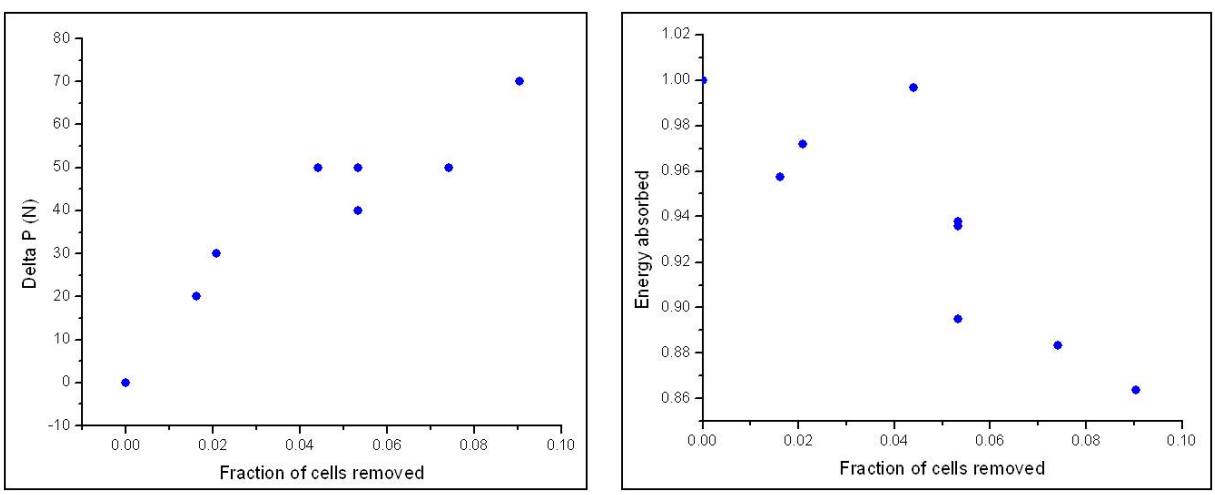

Figure 2.4: Influence of fraction of cells removed on δP and energy absorbed

3. The plateau load appears to increase linearly with the width of the specimen. Thus, the plateau stress is a constant and shall be termed a material property that depends on cell geometry, cell material properties and perhaps cell geometrical imperfections

4. The energy absorbed per unit volume is almost constant.

2.3 Quasi static experiments with defects

The effect of defects on the deformation pattern and crush response was also studied. The motivation behind this test was to see if we have control over the deformation pattern and the direction of propagation of failure and thus the energy absorption. Defects can be introduced in the specimen in various ways. Defects are introduced by removing cells from the specimen in a particular pattern and observing its effect on the response of the specimen. The tests were carried out on the INSTRON machine at a rate of 10 mm/min and images were taken at 5 images per second.

2.4 Defects: Symmetric defects

We considered a specimen of size 20×20 and various patterns of defects were studied and were described in detail in the previous report. It was observed that regardless of the defect size, shape and location of the defect the specimen finally attained the same plateau load as observed for the homogeneous specimen. There is an initial slope which was the same as that of the homogeneous specimen and then collapse of the layers containing the defect starts, then load at which this occurs is less than that of the homogeneous specimen and depends on the size of the defect. After the layers containing the defect have collapsed completely the load attains the value of the homogeneous specimen. This pattern was observed for all the defect shapes and

Model #	Fraction of cell removed	Normalized energy absorbed	δP (N)
1	0.0000	1.0000	0
2	0.0162	0.9575	20
3	0.0209	0.9720	30
10	0.0441	0.9966	50
4	0.0534	0.9356	50
5	0.0534	0.8950	40
6	0.0534	0.9377	50
7	0.0905	0.8638	70
8	0.0742	0.8832	50

Table 2.2: Influence of symmetric defect amount on energy absorption and δP

sizes considered.

The summary of quasi-static tests with symmetric defect is given in Table 2.2. The characterizing parameters are the fraction of cells removed which is defined as the number of cells removed to the total number of cells in a homogeneous specimen of the exact size. Define δP which is the difference between the initial collapse load and the final plateau load. The energy absorbed and the δP values are plotted for the fraction of cells removed and is shown in Figure 2.4. The energy absorbed decreases with an increase with the increase in the fraction of cells removed.

2.5 Defects: Asymmetric defects

The effect of asymmetric defects was also studied. The defect is of the same size and shape on the two sides of the specimen and the eccentricity of these defects was varied. The defects were created by removing cells from the specimen. We also allow for any axial displacement (2-direction in Figure 2.5) by placing ball bearings on the top surface. Polycarbonate ball bearings were used so as to not pre-load the specimen. Two types of defects of the same shape are considered for this study. In the type I defect we consider a defect size of 4 cells and in the type II defect we consider a size of 7 cells.

2.5.1 Type I defect

The type I defect of size 4 cells and with eccentricity between the defects defined as shown in Figure 2.5 was studied. Several tests were done for each case and the results the representative results are provided here. The load response and deformation pattern for different eccentricities are shown below.

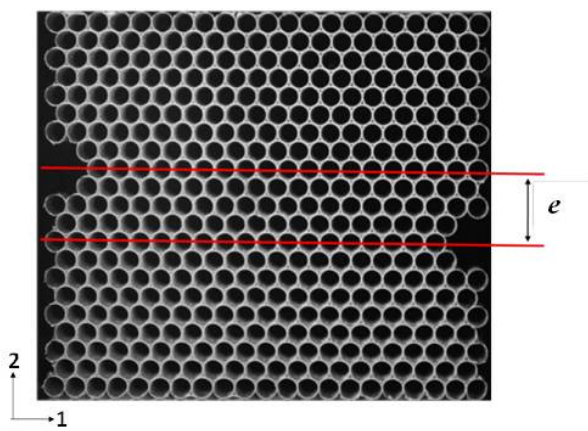

Figure 2.5: Honeycomb with Type I defect

For e = 0, the deformation starts at the layer containing the defect and the corresponding to a lower collapse load. After the layers containing the defect have collapsed completely the collapse load steps up to the plateau load observed in a homogeneous specimen as shown in Figure 2.6. For e = 1, the deformation pattern is similar to the previous case and is shown in Figure 2.7. For e = 3, the initial deformation starts in the layers with the defect but as the loading increases shear band forms in the specimen which indicates a possible interaction between the defects. Also in the load response, the initial collapse load is lower and then finally attains the plateau load. But the strain at which it attains the plateau is higher than observed for previous eccentricities as shown in Figure 2.8. For e = 5, the response is the same as observed for the case e = 3 and is shown in Figure 2.9. For e = 7, the deformation starts in the layer containing the defect but as the loading increases, there is a prominent increase in the interaction between

the two defects owing to the formation of larger shear bands as shown in Figure 2.10. For $e = 9$, the response is similar to the case $e = 7$ and is shown in Figure 2.11.For $e = 11$, the deformation starts in the layer with the defect but since the eccentricity is too large there is lesser interaction between them as the loading increases as shown in Figure 2.12. For $e = 13$, the eccentricity as so large that the defects do not interact at all and the deformation starts at the defect layer and progresses consecutively to the rest of the specimen as shown in Figure 2.13.

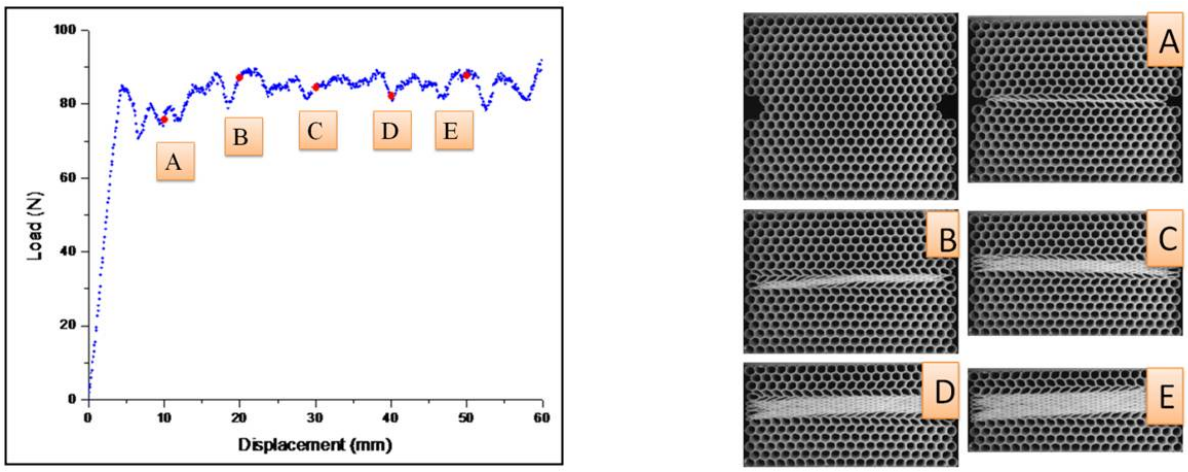

Figure 2.6: Load response and deformation pattern for $e = 0$

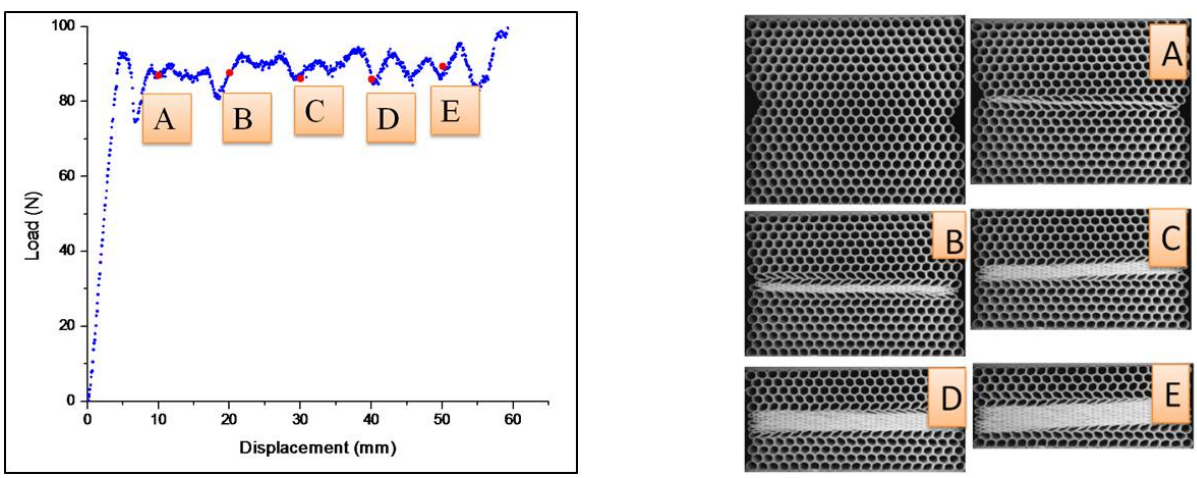

Figure 2.7: Load response and deformation pattern for $e = 1$

The summary of all the type I defects studied is shown in Figure 2.14. The final plateau load

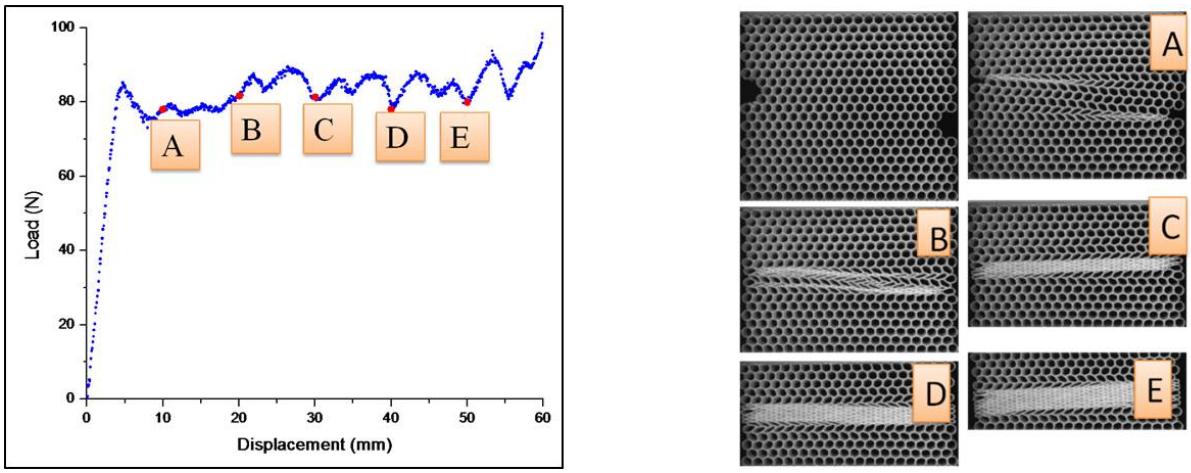

Figure 2.8: Load response and deformation pattern for $e = 3$

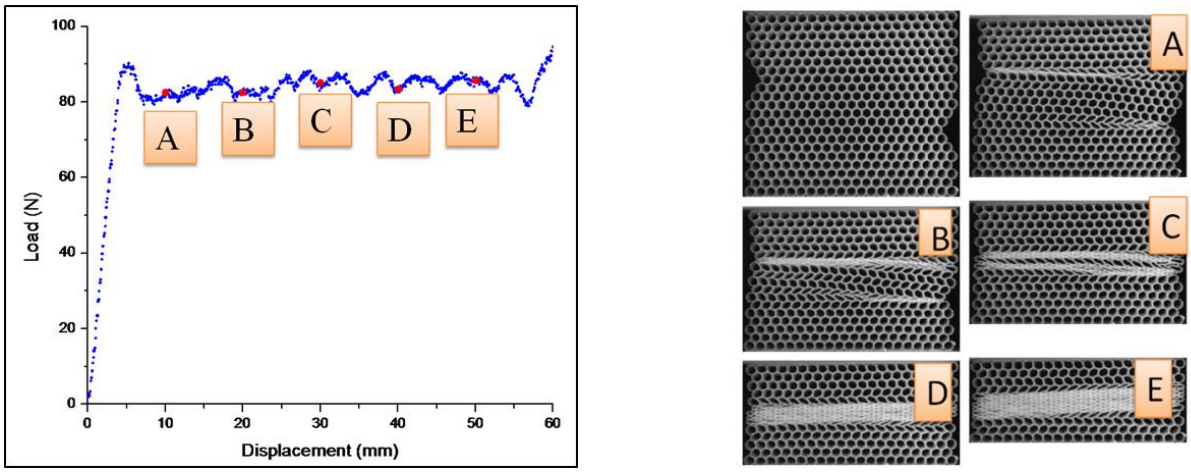

Figure 2.9: Load response and deformation pattern for $e = 5$

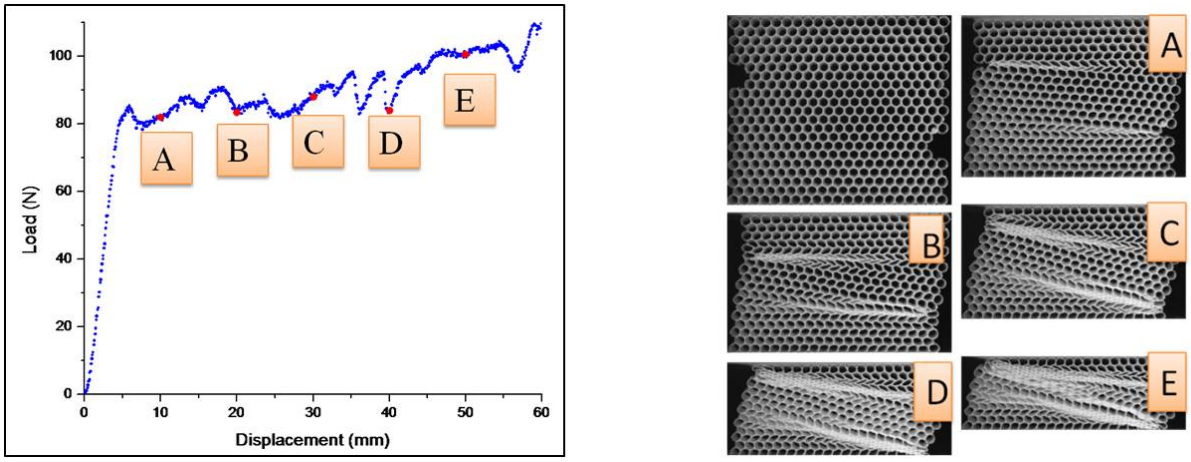

Figure 2.10: Load response and deformation pattern for $e = 7$

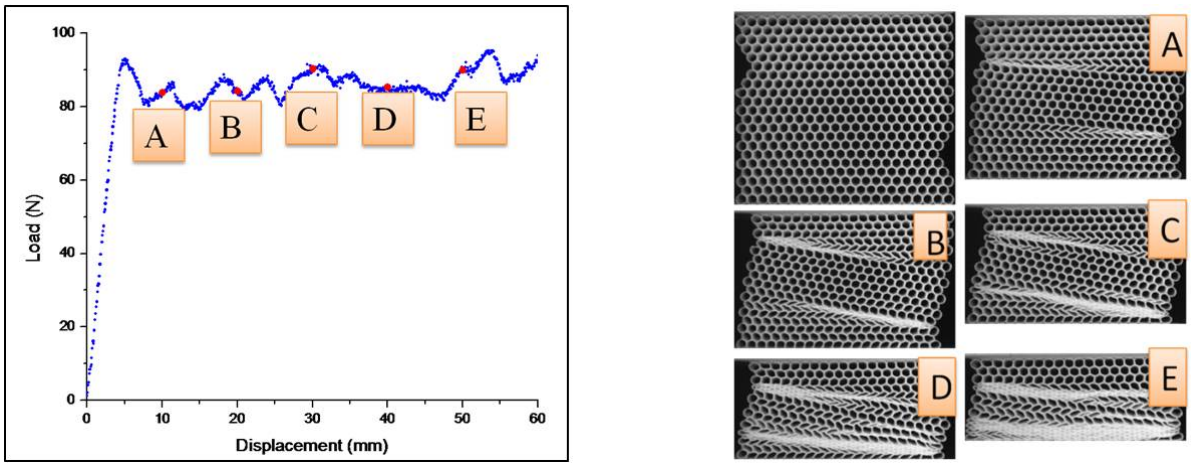

Figure 2.11: Load response and deformation pattern for $e = 9$

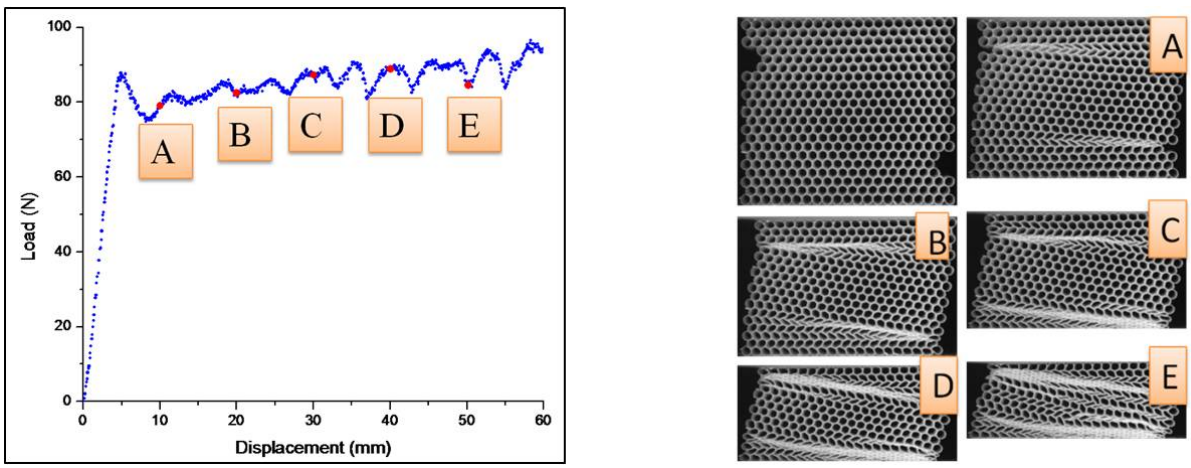

Figure 2.12: Load response and deformation pattern for $e = 11$

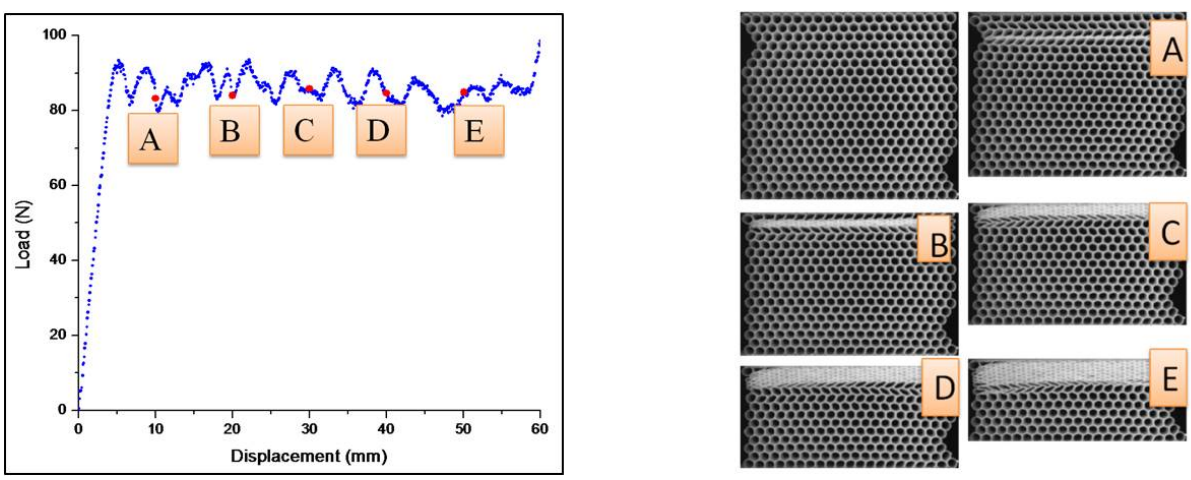

Figure 2.13: Load response and deformation pattern for $e = 13$

observed for all the defects matches that obtained for a homogeneous specimen. The second plot shows a representative plot for a few values of eccentricity. It can be observed clearly that as the eccentricity increases the strain at which it attains the plateau load increases. Also, for the defects in which shear bands are forming during the deformation, the load increases gradually as opposed to lower eccentricities where the load rises in a step fashion. To summarize:

1. The plateau load of the specimens always reaches a fixed value regardless of the defect location.
2. Typically the load starts off at a lower value (compared against the non-defective specimen) and finally attains the plateau load (equal to that for a homogeneous specimen) as soon as the layers containing the defect collapse.
3. It was also observed that as the eccentricity increases the load attains the plateau load at a higher strain.
4. For very small eccentricity the specimen attains the plateau in a stepwise pattern, and for higher eccentricities the plateau load is attained gradually.
5. For the type-1 defect we observe that for medium eccentricities (e = 5 to 11) we observe shear bands in the specimen which vanishes for higher (e > 11) and lower (e < 5) eccentricities.

2.5.2 Type II defect

The type II defect of size 4 cells and with eccentricity between the defects defined as shown in Figure 2.15 was studied. Several tests were done for each case and the results the representative results are given. The load response and deformation pattern for different eccentricities are shown below.

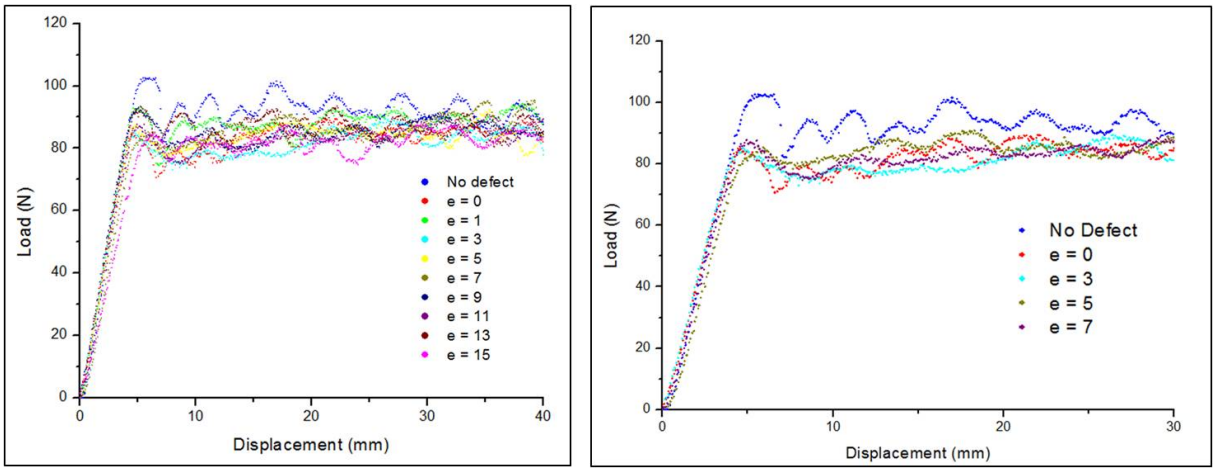

Figure 2.14: Summary of response of honeycomb with type I defects

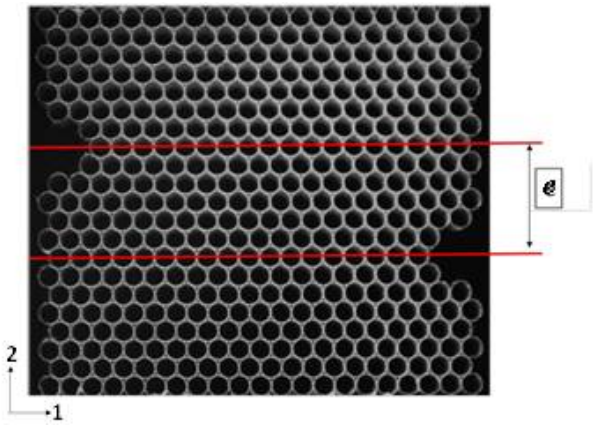

Figure 2.15: Honeycomb with Type II defect

For e = 0, the deformation starts at the layer containing the defect and the corresponding to a lower collapse load. After the layers containing the defect have collapsed completely the collapse load steps up to the plateau load observed in a homogeneous specimen as shown in Figure 2.16. For e = 1, the deformation pattern is similar to the previous case and is shown in Figure 2.17. For e = 3, the initial deformation starts in the layers with the defect but as the loading increases, a shear band forms in the specimen which indicates a possible interaction between the defects. Also in the load response, the initial collapse load is lower and then finally attains the plateau load. But the strain at which it attains the plateau is higher than observed for previous eccentricities as shown in Figure 2.18. For e = 5, the response is the same as observed for the case e = 4 and is shown in Figure 2.19. For e = 7, the deformation starts in the layer containing the defect but as the loading increases, there is a prominent increase in the interaction between the two defects owing to the formation of larger shear bands as shown in Figure 2.20. For e = 9, the response is similar to the case e = 7 and is shown in Figure 2.21. For e = 9, the response is similar to the case e = 9 and is shown in Figure 2.22. For e = 9, the response is similar to the case e = 11 and is shown in Figure 3 24.

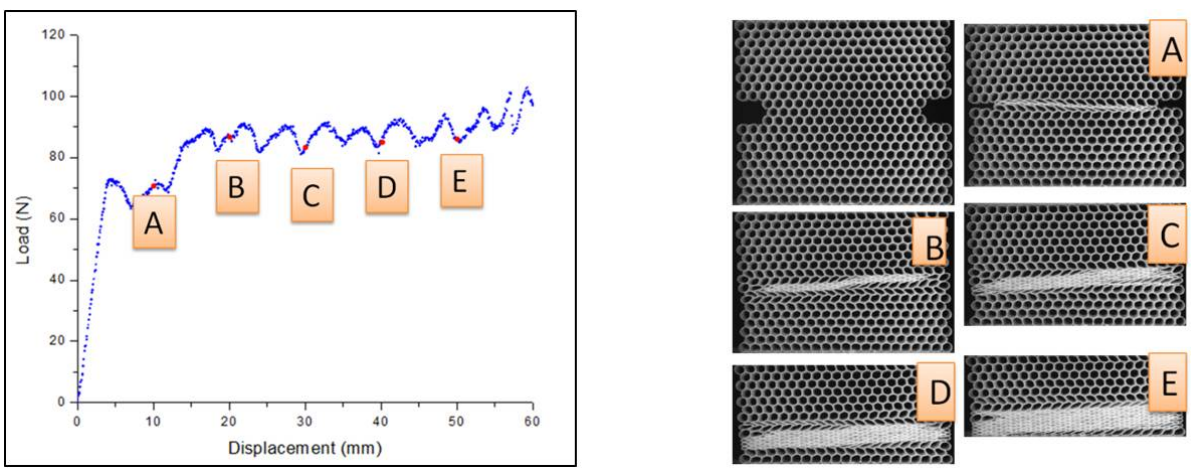

Figure 2.16: Load response and deformation pattern for e = 0

We summarize all the type II defects in Figure 2.24. We can observe that the final plateau load

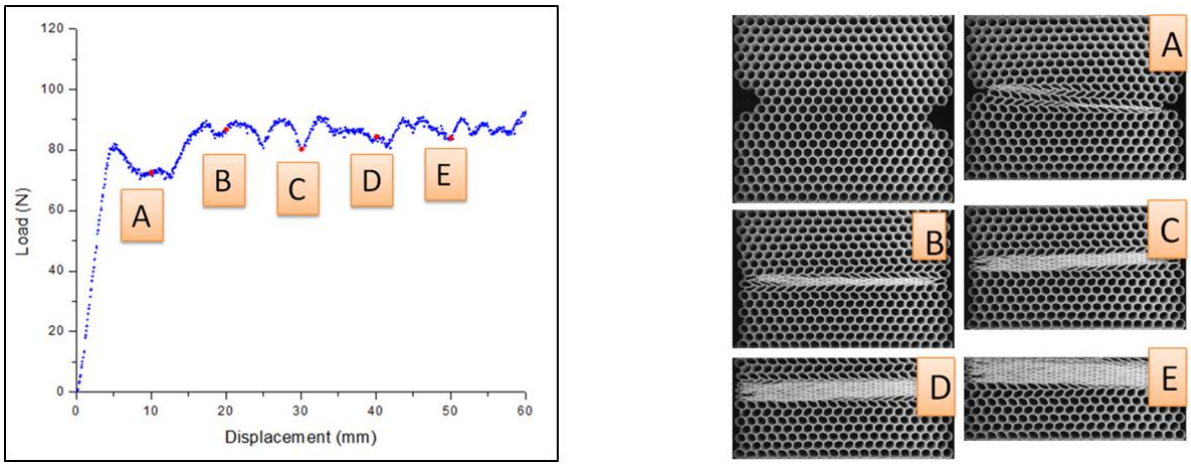

Figure 2.17: Load response and deformation pattern for $e = 1$

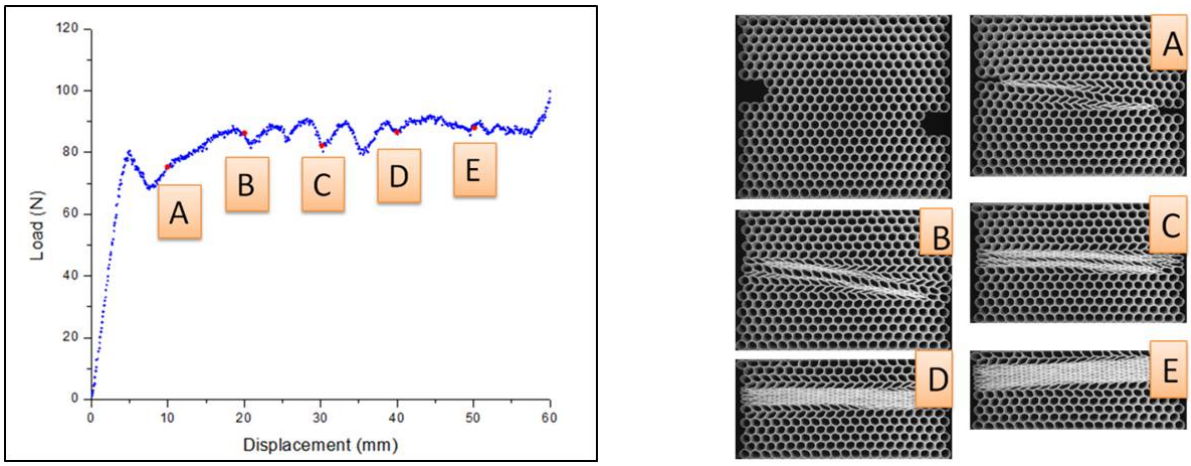

Figure 2.18: Load response and deformation pattern for $e = 3$

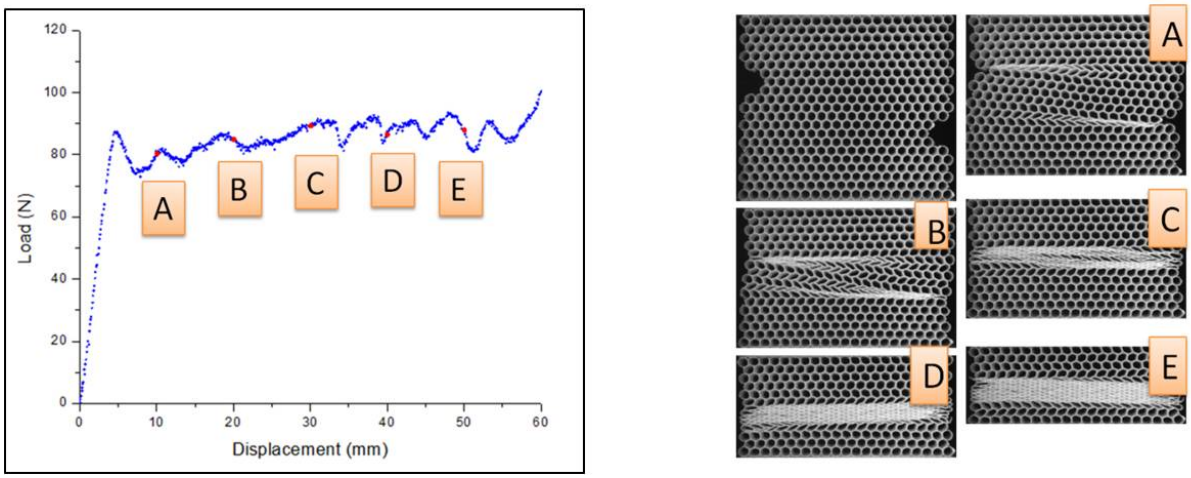

Figure 2.19: Load response and deformation pattern for $e = 5$

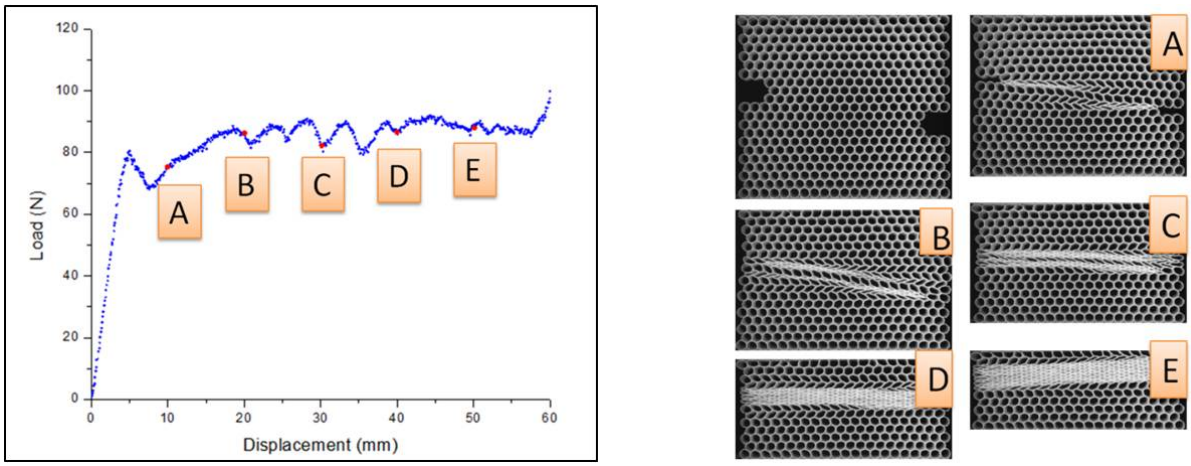

Figure 2.20: Load response and deformation pattern for $e = 7$

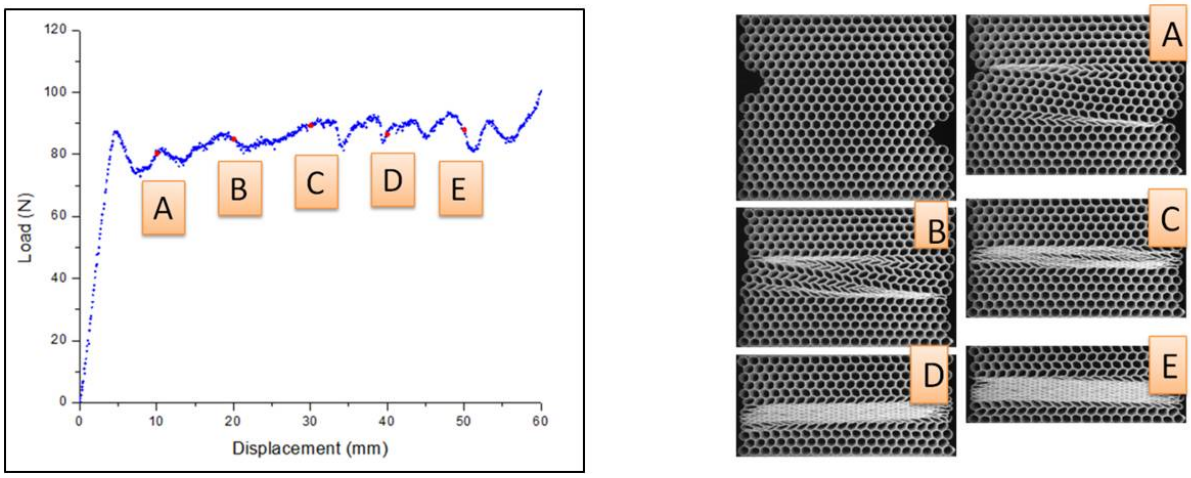

Figure 2.21: Load response and deformation pattern for $e = 9$

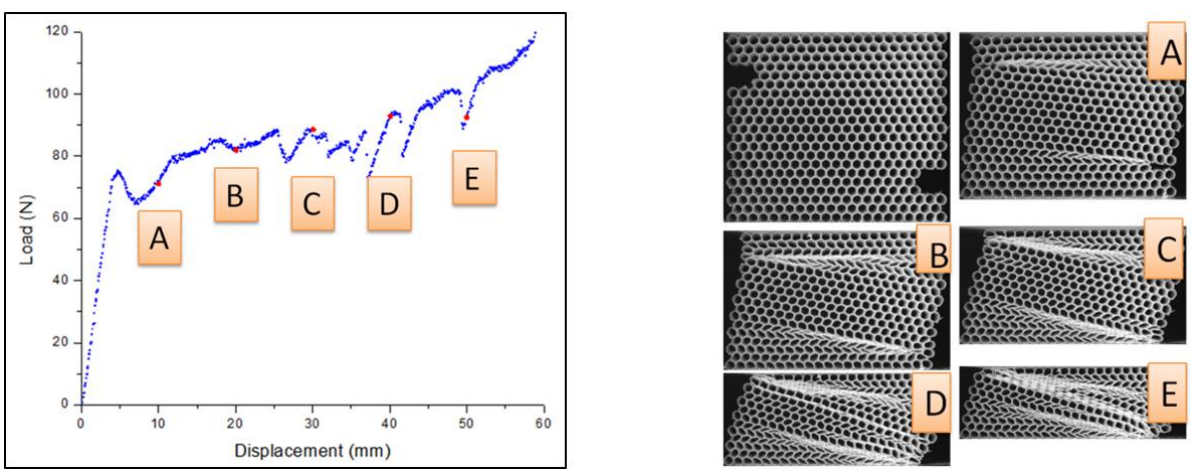

Figure 2.22: Load response and deformation pattern for $e = 11$

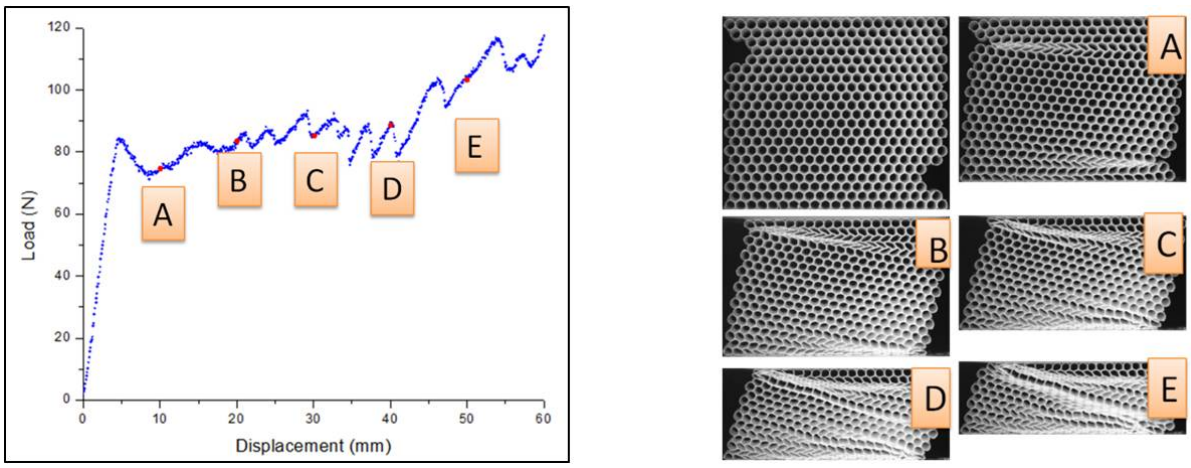

Figure 2.23: Load response and deformation pattern for e = 13

observed for all the defects matches that obtained for a homogeneous specimen. The second plot shows a representative plot for a few values of eccentricity, it can be seen clearly that as the eccentricity increases, the strain at which it attains the plateau load increases. Also the defects in which shear bands are forming during the deformation the load increases gradually as opposed to lower eccentricities where the load raises in a step fashion. The initial crush load for type II defect specimens is lower than that those with type I defect. Also, the interaction between the defects is more pronounced here and thus the shear bands are larger than in the type 1 defect honeycomb. In summary

1. The plateau load of the specimens always reaches a fixed value regardless of the defect location as seen in type I defect.

2. Typically the load starts off at a lower value and finally attains the homogeneous plateau load as soon as the defect layers collapse. And the value at which the deformation starts is lower than in type I.

3. It was also observed that as the eccentricity increases the load attains the plateau load at a higher strain.

4. For very small eccentricity the specimen attains the plateau in a stepwise pattern, and for

higher eccentricities the plateau load is attained by an increasing slope.

5. As the eccentricity increases we see shear bands forming in the specimen which are more prominent than those seen in type I defect.

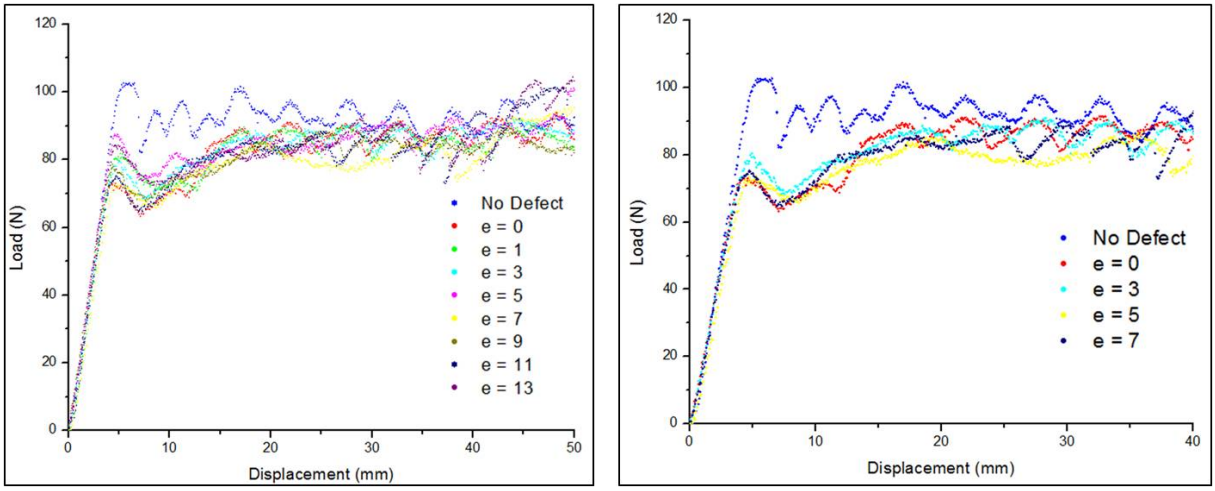

Figure 2.24: Summary of response of honeycomb with type II defects

Chapter 3

Dynamic out-of-plane crush response of honeycomb

3.1 Introduction

Light-weight honeycomb structures are commercially manufactured from metals like aluminium and stainless steel or from synthetic polymers such as polycarbonate, polypropylene and aramid. They are widely used in sandwich panels as the core material due to their high out-of-plane stiffness to weight ratio. They are also capable of absorbing large amounts of energy when subjected to static or impact loading and are hence used as energy absorption devices in the automotive and aerospace engineering industries (Goldsmith & Sackman 1992, McFarland Jr. 1964, Gibson & Ashby 1997). A variety of cell shapes, sizes and cell wall thicknesses are now available for commercial use. These honeycombs fall into the broad category of cellular solids, and their mechanics, including random microstructures are described in Ostoja-Starzewski (2008). In the present study, the axial crush response of circular cell polycarbonate honeycombs is the subject of investigation. Structurally, the constituent repeating unit, referred to as the *cell* can

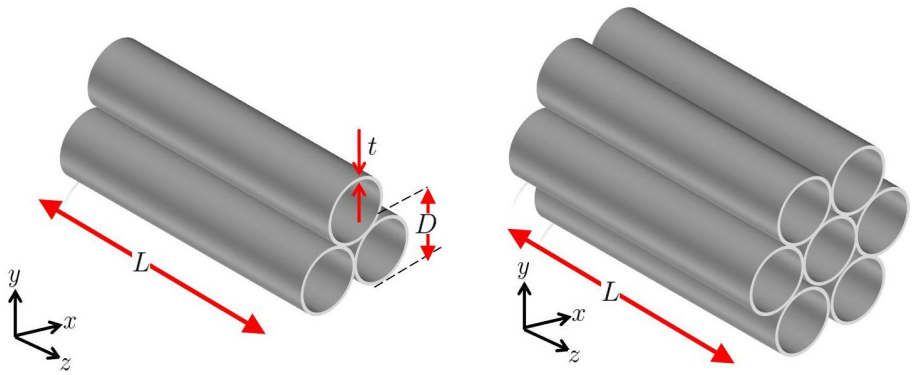

Figure 3.1: Diagram of the 3 and 7-cell circular polycarbonate honeycomb.

be classified as a thin circular shell with radius to wall thickness ratio $R/t >> 1$. Therefore, the mechanics of energy absorption of the basic repeating unit has close association with the classical problem of shell buckling (Brush & Almroth 1975). Naturally, the understanding of honeycomb structural response is more complicated than that of its basic repeating shell unit. The axial direction, which is parallel to the cell generators, also referred to as the out of plane direction of the honeycomb panel, exhibits a much higher stiffness when compared to the in-plane direction. Consequently, the macroscopic characterization of a honeycomb structure does not conform to an isotropic model. Several analytical and experimental methods to determine anisotropic honeycomb material properties are reviewed by Schwingshackl *et al.* (2006).

A key parameter that characterizes the crashworthiness and which gives a measure of the energy absorption capacity of these structures is the axial *crush load*. The crush load (also referred to as the plateau load in some studies, for example, Papka & Kyriakides 1994) is defined as a state of near constant load where progressive collapse of the structure occurs. The effect of crush load of circular polycarbonate honeycombs with respect to scaling in terms of the number of cells per specimen under quasi-static axial loading was experimentally studied by Mellquist & Waas (2002). They concluded that scaling in terms of number of cells had no significant effect on the axial crush load per cell. Wierzbicki & Abramowicz (1983) studied the axial crushing of metallic tubes and reported that the mean crush force depends on the thickness (t) of the shell

as $t^{5/3}$. Wilbert *et al.* (2011) studied the quasi-static axial crush response of hexagonal cell Al-5052-H39 honeycomb panels experimentally and through explicit finite element simulations. They reported that the fold initiation starts at the center of the specimen and the specimen progressively crushes towards either ends. Wu & Jiang (1997) studied static and dynamic axial crush response of metallic honeycombs and reported that the crush load was proportional to the impact velocity. Baker *et al.* (1998) studied the static and dynamic response of high density metal honeycombs. They reported that the dynamic plateau stress was about 50% higher than the quasi-static value. Vural & Ravichandran (2003) studied the dynamic compressive response of balsa wood (a naturally occurring cellular material) along the grain direction using a modified split Hopkinson pressure bar. They showed that initial failure stress was highly sensitive to loading rate and that the plateau stress was insensitive to the strain rate. Recently, Hou *et al.* (2011) used a nylon split Hopkinson pressure bar system with beveled ends of different angles to study the combined shear-compression dynamic response of hexagonal honeycombs. They concluded that for a given angle of loading, there was strength enhancement when compared with the quasi-static loading. Hong *et al.* (2008) conducted quasi-static and dynamic crush tests of 5052-H38 honeycomb specimens under out-of-plane inclined loads. They reported that as the impact velocity increased, the normal crush strength increased but the shear strength was relatively unaffected. Xue & Hutchinson (2006) proposed a continuum constitutive model to simulate the dynamic strengthening behavior of square honeycomb cores during multi-axial dynamic loading. Their model takes into account inertial resistance, inertial stabilization of webs and material strain-rate dependence. Mohr & Doyoyo (2006) developed a constitutive model (finite strain, orthotropic and rate-independent) for metallic honeycombs based on the plateau stress.

The foregoing literature review indicates a gap in analytical and computational studies related to the deformation response of honeycombs at high loading rates, validated by experimental data, with respect to assessing energy absorption and collapse. The studies of Hong *et al.* (2008),

and Hou *et al.* (2011) on aluminum hexagonal cell honeycombs, show an increase in energy absorbing capacity at elevated crush rates, but similar findings with respect to circular cell honeycombs and for direct axial crush at elevated rates are absent. A central goal of this study is to extend the findings reported in Mellquist & Waas (2002) to the elevated strain rate regime and to understand the dynamic crush response of a non-metallic honeycomb material with a view to increasing the specific energy absorption (energy absorbed per unit weight). To this end, note that hexagonal and square cell honeycombs are essentially flat plates arranged vertically as a collection whereas, the circular cell is a vertical thin shell, with curvature, which provides a rich plethora of folding dynamics during the axial collapse stage. While the circular shell has been studied in isolation in many prior studies, Brush & Almroth (1975), the interaction of many connected shells and the significance of tailoring this interaction to exploit energy absorption has not been studied before in the dynamic regime. This is an area that requires further study and understanding because of its practical significance related to use in the design of efficient energy absorbing devices in the automotive and aerospace engineering sectors.

We present experimental and associated numerical results of the axial dynamic crush response of 3-cell and 7-cell polycarbonate honeycombs with emphasis on the crush load, fold initiation, fold progression and mode of collapse. The deformation response of specimens with larger number of cells can be gleaned from the 7-cell specimen results as will be discussed later. To the best knowledge of the authors, this study is the first of its kind concerning the dynamic out-of-plane crush response of circular polycarbonate specimens over a range of crush velocities. The features of axial collapse in circular cell honeycombs are important for development of a macroscopic continuum theory (Xue & Hutchinson 2006), which can adequately predict collapse stresses in honeycombs of given physical and material properties. Even though localization of deformation may preclude such a task, a continuum model is indispensable in the analysis of sandwich panels which may contain thousands of cells. To this end, we discuss the dynamic axial crushing of honeycombs that is carried out using two methods, each providing

a unique set of loading characteristics and facilitating a range of input crush velocity; (a) the wave loading device (WLD) method , and (b) the direct impact method (DIM). From the details to follow, the loading from the WLD setup is primarily due to stress waves, particularly during initial stages of loading, whereas the loading in the DIM setup is from inertia loads.

3.2 Review of static out-of-plane crushing

We briefly review the work done by PI and his student (see Mellquist & Waas 2002, 2004) on the static out-of-plane crushing of circular cell honeycombs. They studied the static out-of-plane crush response of polycarbonate honeycombs through experiments and finite element simulation. They studied specimens composed of cells ranging from 1 to 169. The honeycomb cells were of radius (R) 1.588 mm having wall thickness (t) of 0.128 mm. The length (L) of the cell was 25.4 mm in the out of plane direction. The Young's modulus of the polycarbonate material was 2420 N/mm^2 and Poisson's ratio (ν) 0.3. Axial static tests were conducted to understand the response of honeycomb specimens containing different number of cells. The specimens were rigidly mounted on the loading frame by bonding with flat pieces of aluminum. The specimens were subjected to compression using displacement controlled loading. The initial part of the macroscopic stress-strain plot was characterized by a region of stiff linear response. A maximum stress Σ_{peak} called peak stress was attained (Figure 3.2). Macroscopic strain [1] (ϵ) of 0.02 was reached and there was no noticeable radial deformation until this point. Immediately thereafter, a well defined localized concertina buckling mode was formed around the circumference of the specimen leading to a drop in the load. More folds were formed at a constant state of stress, called the plateau stress $\Sigma_{plateau}$ until the specimen was fully crushed. This type of failure was observed in all the specimens containing different number of cells N. A plot showing the values of Σ_{peak} and $\Sigma_{plateau}$ for cell number N per specimen is shown in Figure 3.3.

[1] Macroscopic strain (ϵ) of a honeycomb specimen of undeformed length L having undergone a crushed length of ΔL is defined as $(\epsilon) = \Delta L/L$

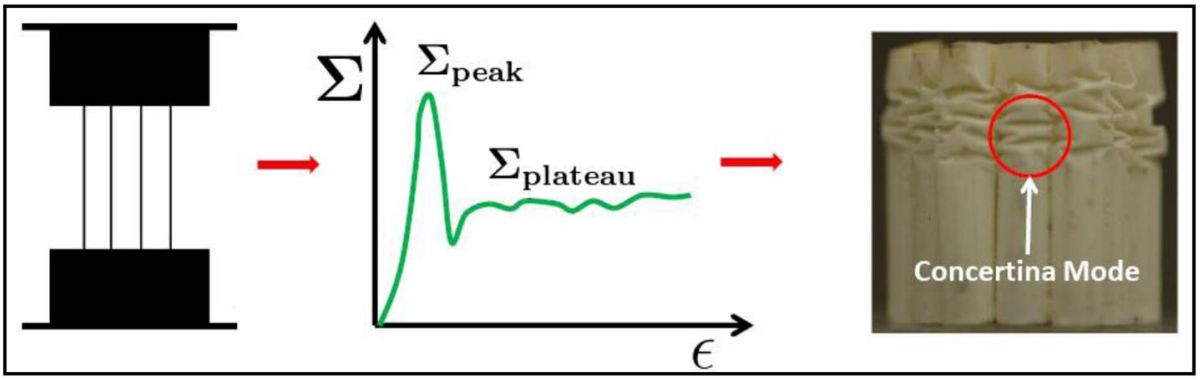

Figure 3.2: Sketch of honeycomb specimen under displacement controlled loading (left). The macroscopic stress-strain response shows a prominent peak and a lengthy plateau region (center). Localized concertina-diamond buckling mode seen in the deformed specimen (right).

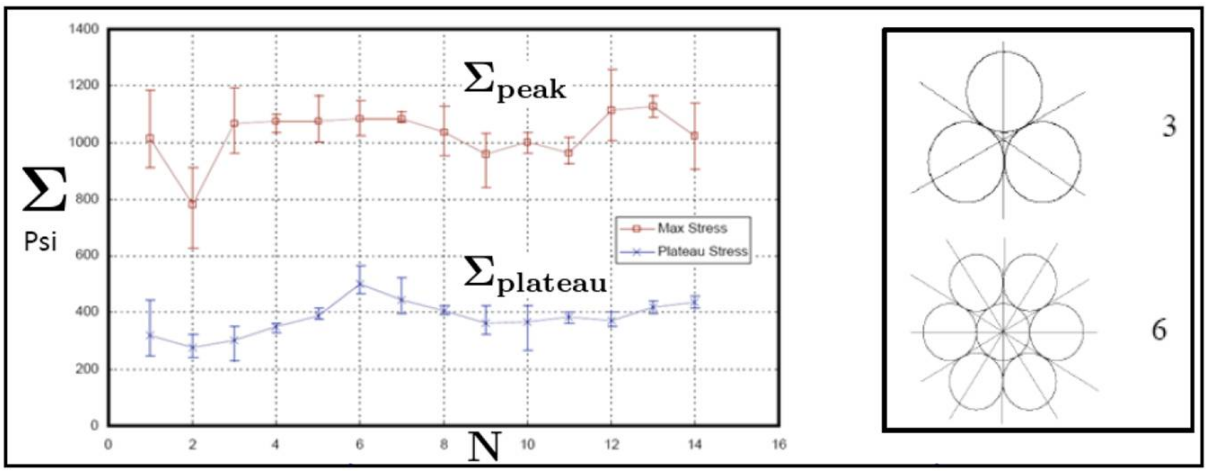

Figure 3.3: The macroscopic maximum stress and plateau stress shown for varying number of cell number N (left). The number of symmetry axes for 3-cell and 7-cell specimens (right). (Mellquist & Waas, 2004)

A finite element model of the honeycomb was developed using ABAQUS® to simulate the axial static crush response of polycarbonate honeycombs. Thin shell, eight-node elements were used to create 1-cell, 3-cell, 4-cell, 5-cell and 9-cell models. The simulations were carried using nonlinear geometry and the modified Riks method. The modified Riks method recalculates the model stiffness matrix at every specified time step thus capturing all stable as well as unstable equilibrium solutions. The boundary conditions used in the model were identical to those used

in the experiments. Both the end faces were constrained against rotations. The bottom face was constrained against translations. The top face was constrained against translations except along the length of the honeycomb. Geometric imperfections were introduced by seeding the perfect mesh with the first three eigenbuckling modes. They found that an imperfection magnitude of 0.2% of the shell thickness produced the best agreement with the experimental results. Material nonlinearity was introduced in the model by using the $J2$ incremental theory of plasticity. The material response was modeled using the uniaxial stress strain curve of the polycarbonate material, which is given in Figure 2a in Chung & Waas (2002). The simulations predicted maximum loads which was in the range of the experimentally measured values but was not able to correctly predict the plateau load seen in the experiments. The concertina-diamond mode of deformation obtained from the simulation closely matched with that observed in their experiment (Figure 3.4).

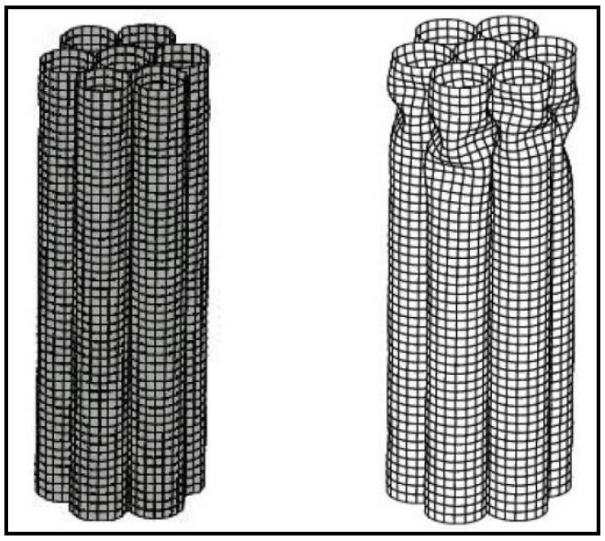

Figure 3.4: An imperfection seeded mesh of a 7 cell specimen (left). The deformed structure obtained from static Riks crush simulation with concertina-diamond mode of deformation (right). (Mellquist & Waas, 2004)

Mellquist & Waas (2002, 2004) concluded that scaling in terms of the number of cells per specimen had no influence on the crush load per cell. Also, the average of the peak stress Σ_{peak} and

the plateau stress $\Sigma_{plateau}$ per cell, for the various specimens was constant. They also observed that, for a specimen with a given number (N) of cells, the variations in maximum and plateau stress for various experimental trials depended strongly on the axes of symmetry of the loading face of the specimen. The more the number of symmetry axes, lesser the fluctuations in the values of Σ_{peak} and $\Sigma_{plateau}$. Therefore, it was inferred that the specimens with higher number of symmetry axes where stable and were less sensitive to imperfections.

We now proceed to the study on the dynamic out-of-plane crushing of circular cell polycarbonate honeycombs.

3.3 Test Preparation

3.3.1 Honeycomb Dimensions

3-cell and 7-cell circular honeycomb specimens made out of polycarbonate were used in this study (Figure 3.1). An accurate measurement of physical properties of polycarbonate material and geometric properties of the honeycomb cell respectively is crucial to correctly characterize the dynamic crush response of the honeycomb panels and also to create finite element models. First, samples were prepared with 7-cell specimens cast in cylindrical molds using epoxy resin and hardener at room temperature. The top face of the hardened sample was polished carefully with dry emery papers of increasing grit sizes in a polishing wheel and was finally polished with a diamond paste with particle size of 5 μm. Several samples were prepared and their micro-section of the cell was studied under an optical microscope (Figure 3.5). As can be seen in Figure 3.5, the cells in the honeycomb panel are in contact with each other not at a point, but over a finite length, which is referred to as the cell adhesion length (l). Variations in the cell dimensions were observed across the samples and the mean value appended with the standard

deviation is provided. Cell wall thickness (t) was 78 $\pm$ 3 μm, the double wall thickness (t_D) was 166 $\pm$ 4 μm, the cell adhesion length (l) was 245 $\pm$ 23 μm and the cell radius (R) was 2.026 $\pm$ 0. 025 mm. The length (L) of the specimen along the axial direction, measured separately was 25.4 mm.

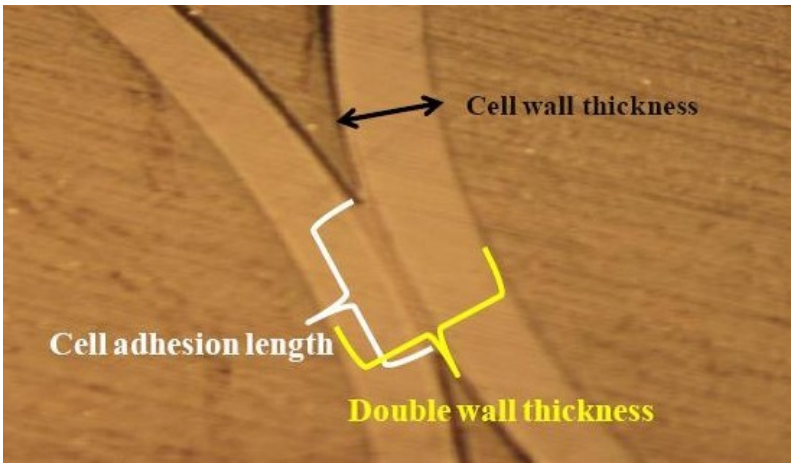

Figure 3.5: Micro-section of the contact site of two cells in the polycarbonate honeycombs as seen under an optical microscope.

3.3.2 Polycarbonate elastic properties & static axial crush load

Next, the elastic modulus of the polycarbonate material was determined using the measured cell dimensions. A single cell was carefully isolated from the honeycomb panel and was mounted to a table-top uniaxial compression test setup. This cell was subjected to displacement controlled compression loading in the in-plane direction to obtain the stiffness data. Such a test was carried out on 10 samples. The experiments gave a consistent measure of the stiffness measuring 24.1 $\pm$ 2.3 N/mm. The factors that amount to the uncertainty in stiffness measurements arise from uncertainty in the cell dimensions (radius, thickness) and also due to the presence of geometric imperfections. A cell subjected to this type of loading is one where the boundary conditions of contact change with the extent of deformation. Therefore, finding an analytical solution form to match the experimentally obtained stiffness is difficult. The problem configuration was

simulated using finite elements using the commercially available software ABAQUS/Standard in performing the modulus extraction. The value of the elastic modulus of polycarbonate was assumed to be same in the in-plane as well as in the out of plane direction. Different trial elastic modulus values were used to match the honeycomb cell stiffness from this analysis to the honeycomb cell stiffness that was experimentally measured. The elastic modulus (E) backed out from this analysis was 2,330 $\pm$ 222 N/mm^2. Next, axial static crush experiments were conducted on 3-cell and 7-cell specimens. The specimens were crushed at a rate of 0.033 mm/s using an INSTRON machine. The crushing occurred via concertina-diamond folds, the folds propagating from one end of the specimen to the other. The plateau load obtained for the 3-cell specimen was 44 $\pm$ 4 N whereas for the 7-cell, the value was 120 $\pm$ 7 N. The crush loads obtained will be used to compare with the dynamic crush experiments, in order to determine whether loading rate influences the crush response.

3.3.3 Measurement of experimental data

The dynamic force sensor is a PCB Piezotronics model 208C02. The force sensor was calibrated by the manufacturer. In the experiments that are described in the following sections, the data from the force sensor was acquired at the rate of 1.6×10^6 samples per second. The raw data was first filtered to remove the high frequency noise such that only the frequencies above the upper limit of the design frequency (90 KHz) of the sensor were eliminated. This data is called *raw data* in the load response plots to follow. The raw data was additionally smoothened using the basic 3rd order Savitzky-Golay averaging filter in MATLAB. This data, which is referred to as *filtered data*, will be plotted alongside the raw data. The raw data will be used to compute estimates of crush/plateau loads and plateau stresses. The discharge time constant of the force sensor was greater than 120 seconds, a duration which is orders of magnitude higher than the time scale of the crush event. The displacement information and mode of collapse was obtained using a high speed camera. Images were collected at the rate of 50,000 frames per second. The

images acquired had spatial resolution of 0.33 mm and 0.2 μs temporal resolution which was adequate in obtaining the displacement information through pixel measurements.

3.4 Experiments: Wave loading device (WLD) method

3.4.1 Setup & Procedure

A *wave loading device* (WLD) was utilized to study the dynamic crush response of 3-cell and 7-cell honeycomb specimens. The experimental setup of the WLD is shown in Figure 3.6. The transmitter bar far end was held against a thick rigid immovable steel plate to prevent its movement when the honeycomb specimen was being loaded. The specimen was carefully mounted between the incident bar and the force sensor that was instrumented on the transmitter bar. The end faces of the specimen were positioned at the geometrical center of the incident bar face and the end-cap face to avoid misalignment during impact. The striker bar was fired from the gas gun at a known pressure (200 - 1000 psi range) and it impacted the incident bar head on. A compressive stress pulse traveled from the impacted end along the length (L_s) of the incident bar with a longitudinal stress wave velocity c_s. When the stress pulse reached the specimen end of the incident bar, the pulse reflected back as a tensile pulse in the incident bar and a part of it traveled as a compressive pulse in the specimen. The specimen was thus loaded in compression. The time taken to crush the entire specimen (L = 24.5 mm) was much longer compared to the crush duration due to the stress wave. Limited crush length ($\approx$ 1.3 mm) was attained in the first period of crushing due to stress waves.

The time taken for the next cycle of crushing was equal to the roundabout trip of the stress wave, i.e. time taken to cover a distance equal to $2L_s$. The motion of the incident bar was found to be a ramp-rest sequence (Figure 3.7). The plot in Figure 3.7 was obtained by tracking the position of

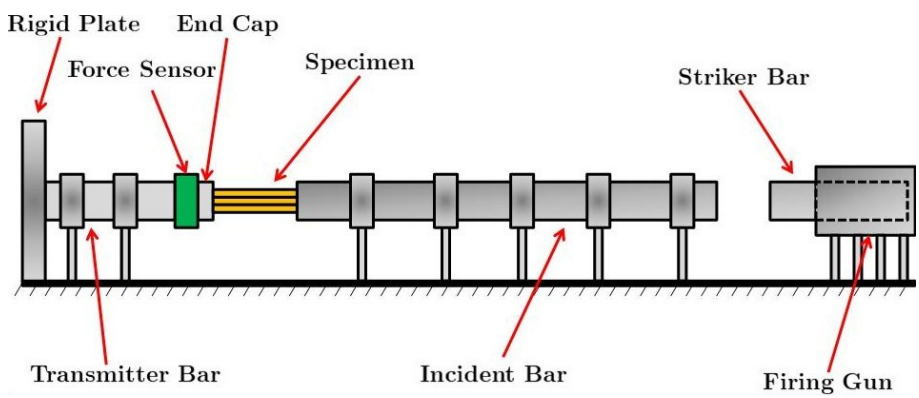

Figure 3.6: Schematic showing the experimental setup of the wave loading device (WLD) . The honeycomb specimen is positioned between the incident bar and the end cap of the force sensor.

the incident bar end in contact with the honeycomb, by performing pixel measurements of the high speed images obtained. The cross-sectional diameter of the hardened steel bars was 12.7 mm. This dimension is much smaller compared to the length (L_s = 1,828.8 mm) of the incident bar. The diameter of the hardened steel striker bar was 12.7 mm and had a length of 304.8 mm. One dimensional wave theory states that the fundamental longitudinal wave velocity (c_s) in a material depends on the elastic modulus (E_s) and density (ρ_s) and is given by the relation (see Kolsky 2003)

$$c_s = \sqrt{\frac{E_s}{\rho_s}} \tag{3.1}$$

where the elastic modulus (E_S) of the bar material is 210 GPa and the mass density (ρ_s) is 7,800 kg/m^3. From Equation (1), the stress wave velocity was calculated to be 5,225 m/s. Utilizing Equation (1), the time interval (ΔT_{1-D}) between successive tensile stress waves to reflect from the specimen end of the incident bar was 0.70 milliseconds. This time interval agreed very well with the time interval ($\Delta T_{EXP} \approx$ 0.68 milliseconds) between two successive loading events measured from the experiment (Figure 3.7). Note that this time interval is independent of the gas gun firing pressure or the striker bar velocity. This time interval depends on the stress wave velocity, which is a function of the physical properties of the incident bar material. However, the velocity of impact of the striker bar has a direct relation with the velocity of crushing during the ramping motion of the incident bar. The ramp-rest motion ceased to exist as time progressed

because the stress waves in the incident bar gradually waned out due to damping losses and due to wave interference resulting from multiple reflections in the incident bar. Thereafter, the motion of the bar was mainly due to rigid body motion with lower crush velocities as is seen clearly in Figure 3.7. Therefore, the 1-D wave theory is sufficient to satisfactorily explain the mechanics of ramp-rest motion that was encountered in this study. Note that one is not concerned with the wave interactions in the incident bar beyond the first reflection at the specimen end. In other words, the incident bar mainly serves as a projectile with ramp-rest loading profile. Also, from the high speed images, it was observed that the transmitter bar did not move when the specimen was being loaded. This observation can be explained due to two reasons: (1) the rigid, immovable plate acts as a momentum trap thus absorbing any stress waves that get transmitted through the specimen, and (2) the high mechanical impedance[2] mismatch at the specimen-transmitter bar interface curtails the ability of the stress waves to pass from the specimen into the transmitter bar. Moreover, note that the intensity of the initial stress pulse that was transmitted through the specimen, till this point, was significantly reduced due to high impedance mismatch at the incident bar-specimen interface. Hence, unlike in a regular SHPB setup, the transmitter bar plays no active role in the WLD experiment, except for restraining the honeycomb in the out-of-plane direction. In summary, the success of the WLD method is due to making use of a momentum trap (via the thick, immovable plate) and due use of SHPB material (hardened steel) that has high impedance mismatch with the test specimen (polycarbonate) such that, in effect, the load that the specimen experiences is that arising from the stress waves in the incident bar.

[2]Mechanical impedance at any point in a structure is the ratio of the applied force at the point to the particle velocity at the same point. Qualitatively, it is a measure of how much a structure resists motion when subjected to force.

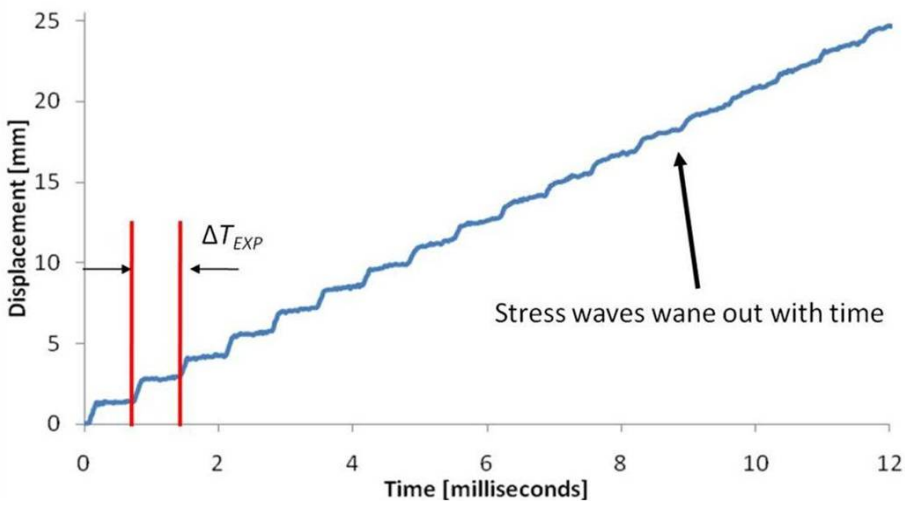

Figure 3.7: Typical rest-ramp displacement of the incident bar at the specimen end. The time interval ΔT_{EXP} for two successive ramp motion is shown. As the stress waves get weaker as time progresses, the velocity of the specimen end of the incident bar tends to that of the rigid body motion of the incident bar.

3.4.2 Results

When the 3-cell and 7-cell specimens were subjected to crush velocities ($v_c \approx 11,000 - 12,000$ mm/s range) in the WLD setup, a characteristic deformation response was observed. The load-time plot for the 3-cell specimen is shown in Figure 3.8 and the images of corresponding deformation sequence is shown in Figure 3.9. For the 7-cell specimen, the load-time plot is shown in Figure 3.10 and the corresponding images during the initial stages of deformation is shown in Figure 3.11. A steep near-linear rise was seen initially and the load rose to a maximum value, referred to as the peak load. Up to this point, the deformation in the specimen was purely axial and the stiff resistance to the moving bar gave rise to the initial peak load. Thereafter, the first localized axisymmetric concertina-diamond folding began accompanied by a drop in the load. The preference of fold initiation immediately after the peak load is attained depends on the inherent geometrical imperfections present. Fold initiation was typically observed at both ends of the specimen. The folds continued to form as long as the incident bar was in motion. Also, transient elastic folds were observed near the ends of the specimens, which recovered

back to the undeformed state in the rest period. After the end of the initial ramp step, the bar was momentarily at rest. Here, the load recorded fluctuated about a mean value with smaller amplitude due to the residual stress waves in the specimen. No folds were formed during the rest period. However, the specimen exhibited hoop-like or breathing vibration modes (these are clearly visible in high-speed movies of the experiment). During the second ramp step, the load momentarily rose with fold formation and dropped at the end of the ramp step. This process continued until the specimen was completely crushed as new folds were formed progressively along the length of the honeycomb cell. The load recorded, beyond the initial phase where fold formation takes place, is referred to as the crush load. The crushing process was observed to occur either (a) from one end with folds formed up to the other end, or (b) simultaneously at both ends. The deformation characteristics explained above holds for both the 3-cell and 7-cell specimens. For the 3-cell specimens, the peak load recorded was approximately 150 N and the crush load measured was 54 $\pm$ 14 N compared to the static crush load of 44 $\pm$ 4 N. For the 7-cell specimens, the peak load recorded was 335 N and the crush load measured was 159 $\pm$ 22 N compared to the static crush load of 120 $\pm$ 7 N. Here, the mean crush load estimate was calculated as the integral average for the loads recorded over successive ramp sections except for the first ramp movement (corresponding to the initial linear response). The uncertainty indicates standard deviation in this load level across various experimental trials.

3.5 Experiments: Direct impact method

3.5.1 Setup & Procedure

In order to observe the behavior of honeycombs at lower crush velocities, the specimens were impacted directly with the striker bar (Figure 3.12). This experimental procedure is referred to as the *direct impact method* (DIM). The DIM was used to achieve crushing in the honeycomb

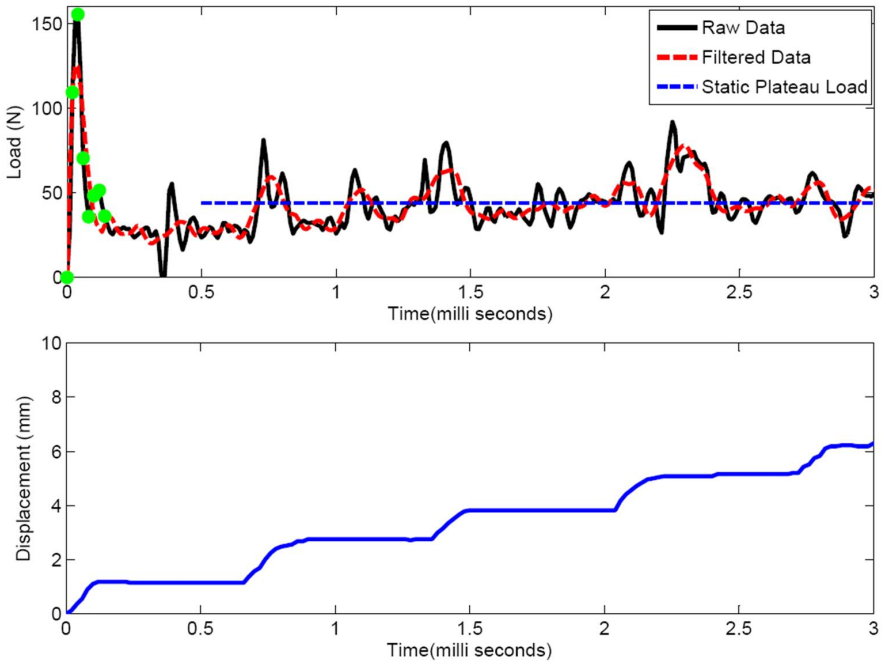

Figure 3.8: Plot showing the initial deformation response of the 3-cell specimen under dynamic crush loading using the WLD method. Load-time plot (top) and ramp-rest displacement of the transmitter bar (bottom). Observe that the crushing takes place during successive ramping phases. The first ramp ends at t = 0.14 milliseconds (ms). The load at time t = 0, t = 0.2 ms, t = 0.4 ms, t = 0.6 ms, t = 0.8 ms, t = 0.12 ms and t = 0.14 ms is shown in green (top).

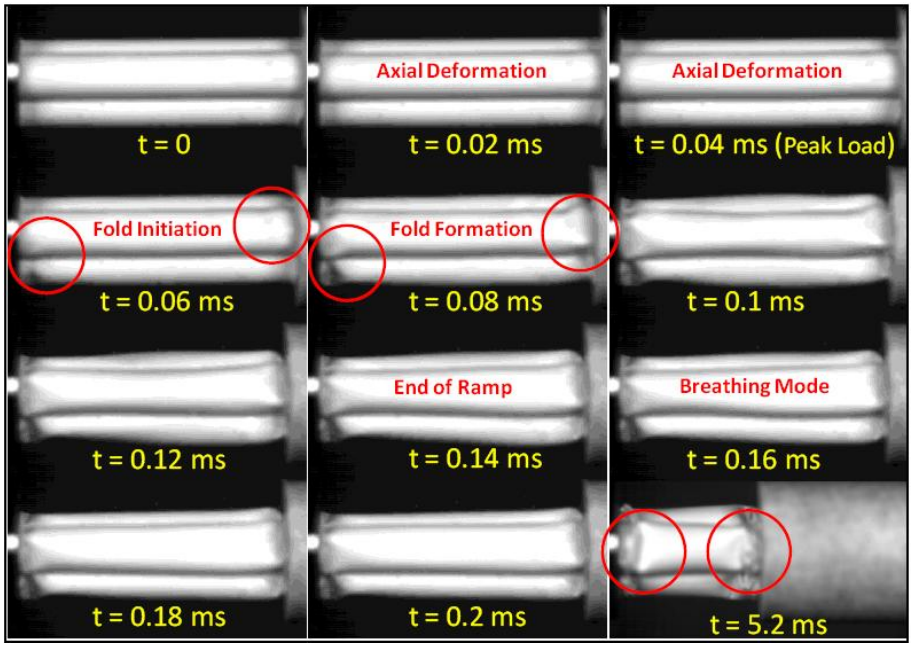

Figure 3.9: Images of the initial stages of deformation in a 3-cell specimen loaded in the WLD setup from t = 0 to t = 0.2 ms. The last image shows the deformed state of the specimen at a later time t = 5.2 ms. In this sample, crushing took place with folds progressively forming at either ends of the specimen

cell by a striker bar moving at a uniform velocity. The specimens were bonded to the end-cap of the force sensor at its geometrical center, and positioned directly in front of the gas gun. The striker bar was fired from the gas gun and it crushed the sample head-on with uniform velocity ($v_c \approx$ 4,000 – 5,000 mm/s). Various firing pressures were utilized as inputs for striker bar firing. A piezoelectric force sensor was instrumented on the transmitter bar. The far end of the transmitter bar was fastened tightly to a rigid, immovable steel plate to avoid any movement of the bar before the specimen had crushed completely. The DIM produces lower crush velocities than the WLD. Between the WLD and DIM, a disparate range of crush velocities can be obtained.

3.5.2 Results

During the initial stages of deformation of the 3-cell and 7-cell specimens loaded by the DIM, the load rose nearly linearly during the stage where the deformation was dominated by axial motion with little or no radial deformation. For the 3-cell specimens, it was observed that when

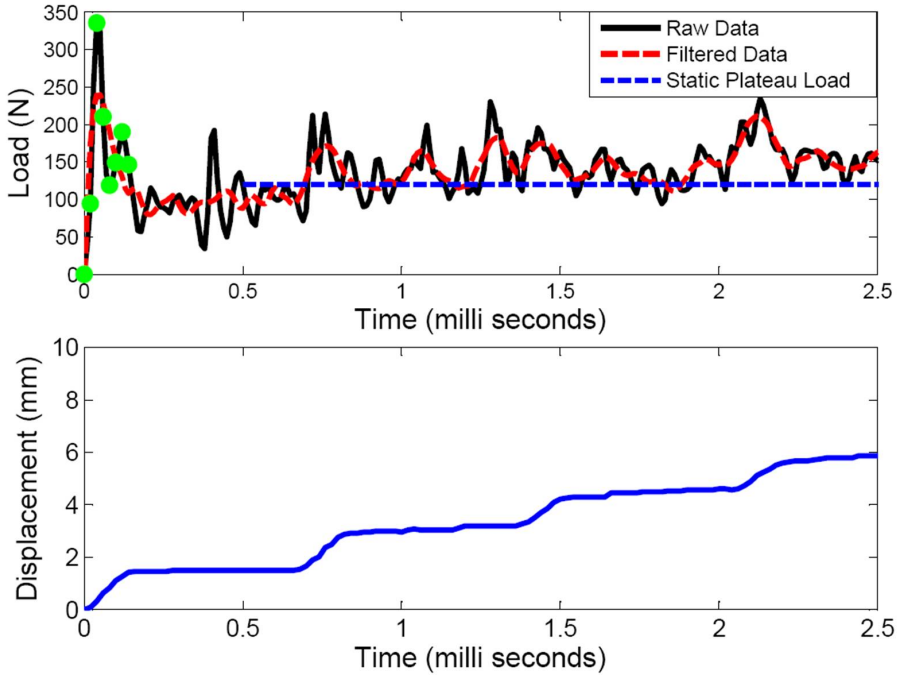

Figure 3.10: Plot showing the initial deformation response of the 7-cell specimen under dynamic crush loading using the WLD setup. Load-time plot (top) and ramp-rest displacement of the transmitter bar (bottom). Observe that the crushing takes place during successive ramping phases. The first ramp ends at t = 0.14 milliseconds (ms). The load at time t = 0, t = 0.2 ms, t = 0.4 ms, t = 0.6 ms, t = 0.8 ms, t = 0.12 ms and t = 0.14 ms is shown in green (top).

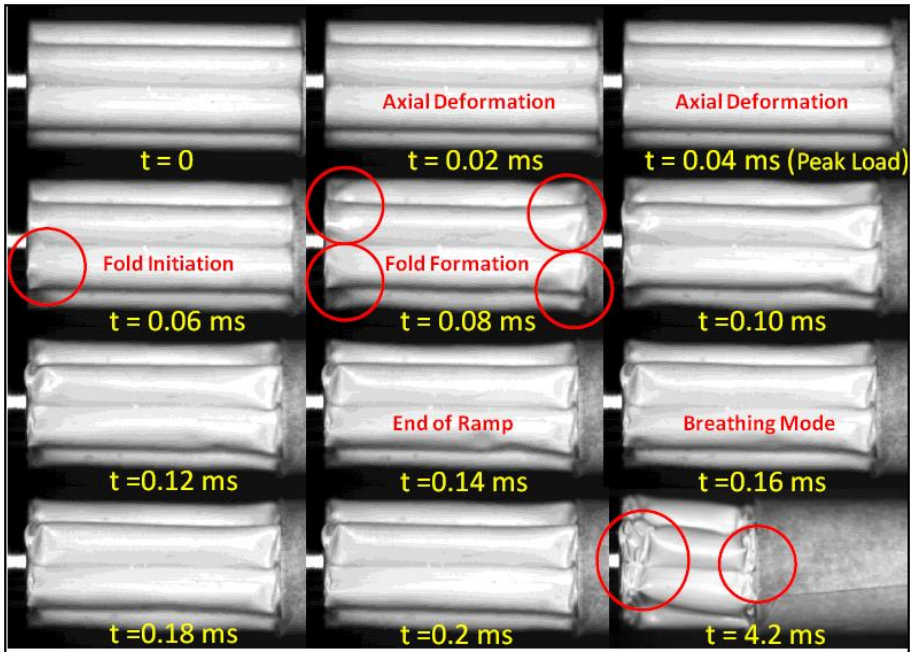

Figure 3.11: Images of the initial stages of deformation in a 7-cell specimen loaded in the WLD setup from $t = 0$ to $t = 0.2$ ms. The last image shows the deformed state of the specimen at a later time $t = 4.2$ ms. In this sample, crushing took place with folds progressively forming at either ends of the specimen

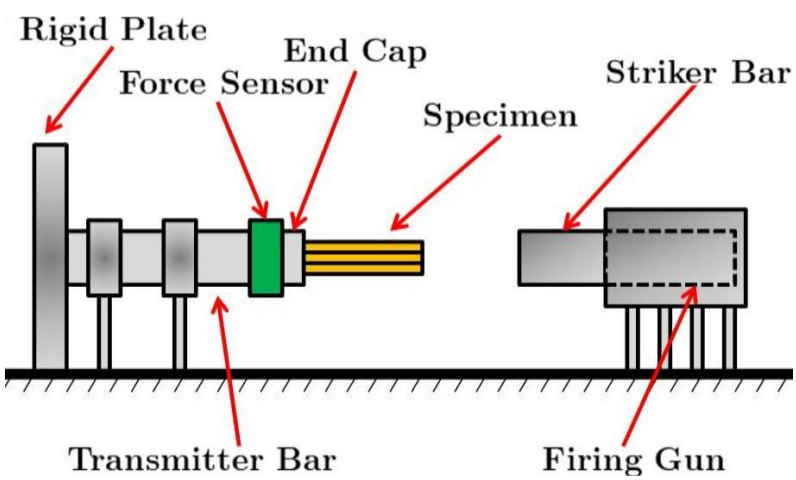

Figure 3.12: Schematic showing the setup for the direct impact method. The honeycomb specimen is positioned sufficiently close to and directly in front of the striker bar. The specimen is bonded to the end cap of the force sensor.

the first fold initiated at the crushing end, there was a prominent peak at the end of the initial rise (Figure 3.13). In contrast, there was no peak at the end of the initial rise when the fold formation initiated at the far end of the specimen (Figure 3.14). For the 7-cell specimens, the load plot and the images from the high speed camera are provided in Figure 3.15. Here, there was no prominent peak at the end of the initial region. Since collapse due to fold formation results in a drop in the crush load, the effect of fold formation at a particular end has an effect on the presence or absence of a peak in the load history that is recorded by the force sensor at the far end of the specimen. If folding initiates at the far end of the specimen, the drop in load is instantly captured by the force sensor, as the far end is in contact with it. Thus, no prominent peak is seen in this case. During crushing at high velocities, the specimen is not in dynamic equilibrium. If the fold formation starts at the impact end, the effect of this collapse does not reflect immediately at the far end of the specimen, which is still stiff. Therefore, a prominent peak is seen at the end of the initial region if fold initiation takes place at the impacted end of the specimen. Soon after the initial rise, fold formation occurred causing the load to drop. This pattern was observed for both the 3-cell and 7-cell specimens. Thereafter, as the striker bar was crushing the specimen, the folding progressed from the fold initiation end to over the length of the specimen. The crush load measured for the 3-cell specimens was 51 ± 7 N (compared to the static crush load of 44 ± 4 N) while that for the 7-cell specimen was 157 ± 15 N compared to the static crush load of 120 ± 7 N). The mean crush load value is calculated as the integral average of points in the plateau region and the uncertainty is the standard deviation of the crush load.

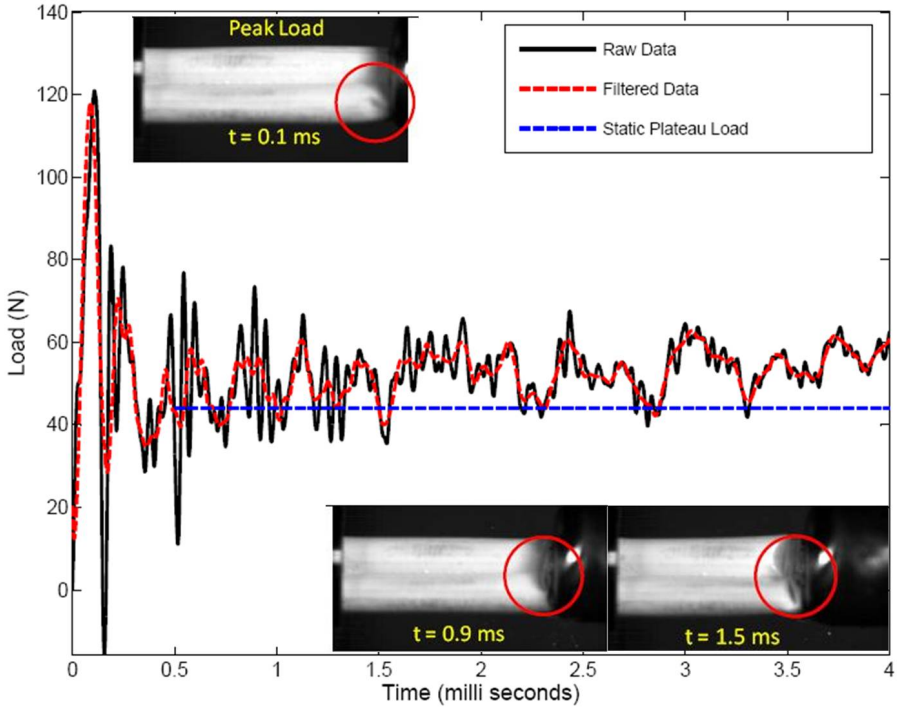

Figure 3.13: Load-time plot of the 3-cell specimen when impacted directly by the striker bar. The first fold occurs at the impact end and clear peak is observed at 0.1 ms. The fold formation continues progressively from the impact end of the specimen as the striker bar crushes the specimen.

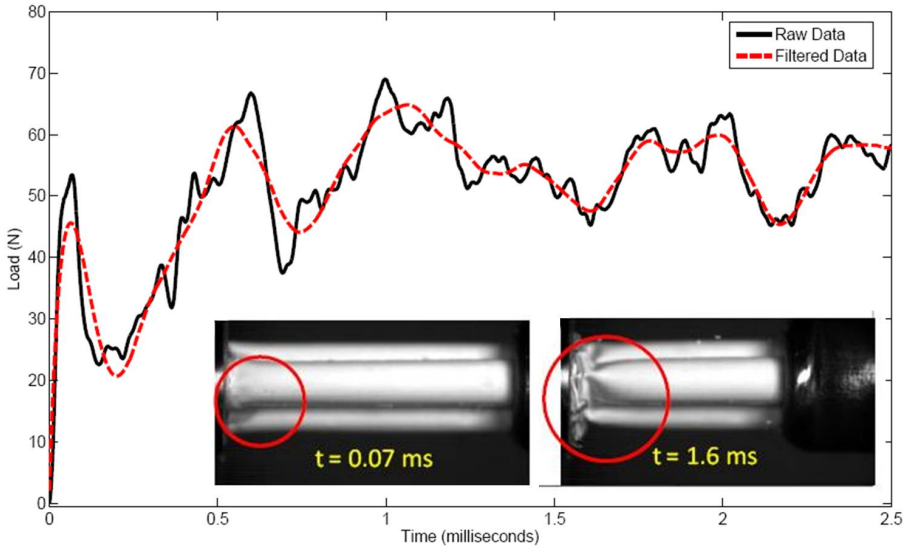

Figure 3.14: Load-time plot of a 3-cell specimen when directly impacted by a striker bar. There is no prominent peak. The first fold starts soon after the linear region ends (t = 0.07 ms) at the far end of the specimen. Folds continue to form progressively from the far end of the specimen.

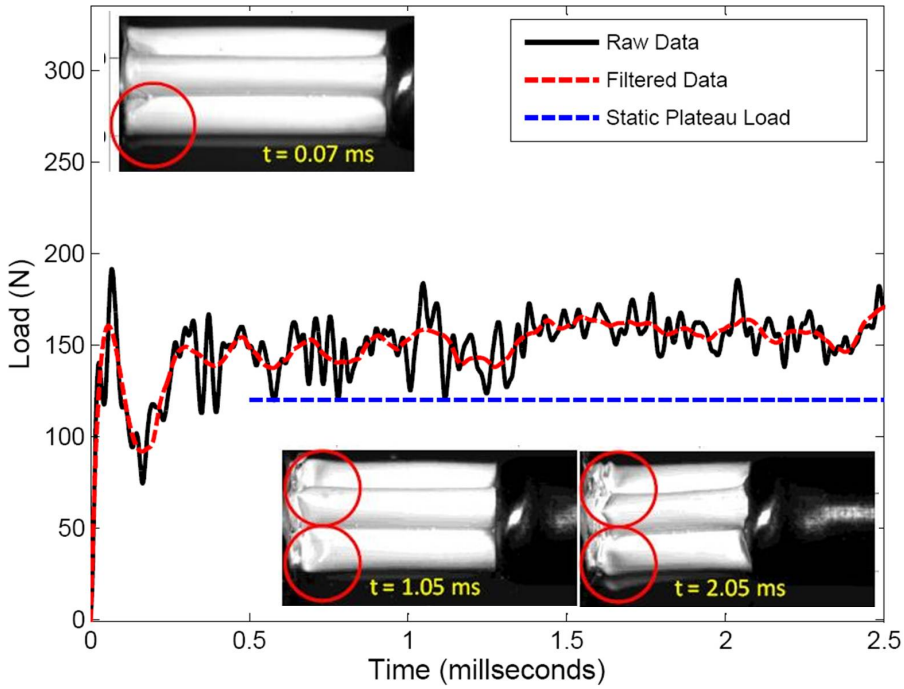

Figure 3.15: Load-time plot of a 7-cell specimen when directly impacted by a striker bar. The first fold starts soon after the linear region ends (t = 0.07 ms) at the far end of the specimen. Folds continue to form progressively from the far end of the specimen.

3.6 Finite Element Model

3.6.1 Introduction

Finite element (FE) analysis was conducted using the commercially available software ABAQUS® to simulate the dynamic axial crush response of the 3-cell and 7-cell honeycombs in the out of plane direction. 3-cell and 7-cell honeycomb specimens were modeled as uniform circular shells with the average measured cell dimensions. In the honeycomb specimens, each cell is in contact with its neighbor through outer wall to wall adhesion. Assume that during dynamic crushing, there is no delamination at the contact surfaces. Therefore, the FE model considers the contact site to be composed of a single unit of adhesion length (l) 250 μm with double wall thickness (t_D) 160 μm. A uniform finite element mesh was generated using linear 4-noded S4R elements with the elements having an aspect ratio $\approx$ 1. A convergence study (with respect to

the plateau load) was conducted and the results presented use the converged mesh. The model contained 125 elements along the axial length and 60 elements along the circumference. The 3-cell model contained 22,696 elements and the 7-cell model contained 52,959 elements.

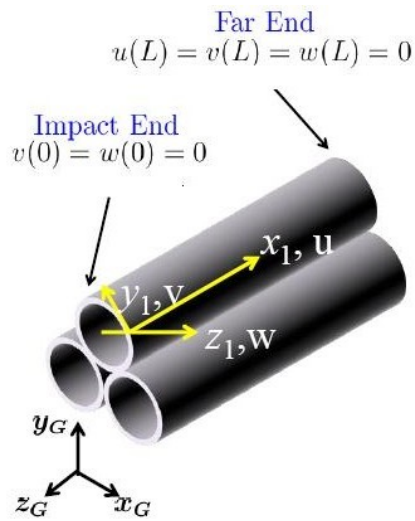

Figure 3.16: Diagram showing the boundary conditions used on the honeycomb during eigenbuckling analysis. These boundary conditions are also used for crush simulations. x_1, y_1 and z_1 are the local shell co-ordinates on a single cell corresponding to axial (u), circumferential (v) and radial (w) displacements. x_G, y_G and z_G are the global co-ordinates for the model.

3.6.2 Eigenbuckling Analysis

Shell structural response is influenced by unintended geometrical imperfections, such as out-of-roundness, non-uniform wall thickness and uncertain boundary conditions that produce non-uniformities in load. Amongst these, geometrical imperfections play a major role as is well established in the shell buckling literature (Babcock 1983, Brush & Almroth 1975). Therefore, our model must account for geometric imperfections present in the honeycomb specimens. The imperfect geometry is modeled as perfect cylinders that have been perturbed by a linear combination of the eigenbuckling modes of the honeycomb. Mathematically, if the buckling mode shapes are represented as $u_n(x_l, y_l) = \phi_n(x_l, y_l)$, $v_n(x_l, y_l) = \psi_n(x_l, y_l)$ and $w_n(x_l, y_l) = \chi_n(x_l, y_l)$ (where u, v and w denote displacements along the axial, circum-

ferential and radial directions respectively), then the location of a point on the perfect shell mid-plane with coordinates, $(X_l, Y_l, 0)$ is perturbed to new coordinates (X_l^P, Y_l^P, Z_l^P) where $X_l^P = X_l + \sum_{i=1}^{N} A_i\phi_i$, $Y_l^P = Y_l + \sum_{j=1}^{N} B_j\psi_j$ and $Z_l^P = \sum_{k=1}^{N} C_k\chi_k$. The shell local axes, x_l, y_l and z_l are indicated in Figure 3.16, and the symbols A_i, B_j and C_k are the amplitudes of the perturbations. Linear buckling analysis was conducted in ABAQUS/Standard to extract the eigenbuckling mode shapes for the 3-cell and 7-cell models. The purpose was to use these modes to seed the perfect geometry to arrive at a model with geometrical imperfections, as the specimens used in the experiment are not geometrically perfect and also their initial shape cannot be measured with sufficient ease and accuracy. The boundary conditions (Figure 3.16) imposed here are as follows. The impact end surface of the cell was constrained in translation along the in-plane direction (x and y) and the far end surface of the cell was constrained in displacement along all three translational degrees of freedom (x, y and z directions). Lanczos algorithm was used as it is most suited for solving large sparse generalized eigenvalue problems (Morris 1990) such as linear buckling problems. Note that all analyses reported here have used only a single eigenmode to perturb the initial geometry and therefore, strictly, one must not expect the imperfections in the model to resemble geometrical imperfections that may be present in the real structure. For every eigenmode chosen to seed the perfect geometry, define quantity called as the *imperfection amplitude* (δ). If a specimen of wall thickness t is seeded with a mode shape of maximum radial amplitude (Δw_{max}), the imperfection amplitude is defined as

$$\delta = \frac{\Delta w_{max}}{t} \tag{3.2}$$

The upper limit of imperfection amplitudes are obtained from the deviation from the perfect circular geometry (15% of wall thickness) in the radial direction of the specimen. The maximum values of δ are chosen such that the initial linear slope of the crush response is not significantly different from that measured from the experiment. Two eigenmodes for each of the 3-cell and 7-cell specimens were chosen as the seeding modes to perturb the perfect geometry (Figure 3.17).

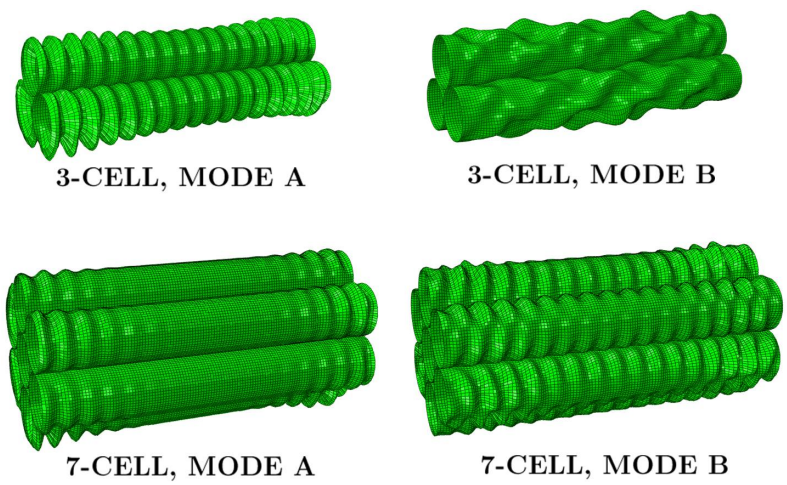

Figure 3.17: Eigenmodes for 3-cell and 7-cell honeycomb models that are chosen to perturb the mesh for explicit FE simulations. Mode A corresponds to the lowest eigenmode and Mode B is chosen corresponding to higher buckling load.

3.7 Dynamic Crush Simulation

3.7.1 Introduction

The dynamic crush FE simulation of 3-cell and 7-cell specimens was carried out in ABAQUS/Explicit. The displacement-time information for the WLD and DIM cases was taken from the experiment using the high speed images. The explicit integration algorithm is ideal for solving large problems because the cost of computation increases linearly with problem size.

Polycarbonate is a strain rate dependent material and this dependency is incorporated in the numerical crush simulation. Mulliken & Boyce (2006) have provided the rate dependent compressive behavior of polycarbonate for strain rates 10^{-4} s$^{-1} \leq \dot{\epsilon} \leq 10^{4}$ s^{-1}. From their work, the values of true yield stress (σ_y) for various compressive strain rates were tabulated and used in the dynamic crush simulations. The initial yield stress (σ_0) was taken to be 66 MPa under static loading ($\dot{\epsilon} \approx 10^{-4}$ s^{-1}). Note that from the $\sigma_y - \dot{\epsilon}$ plot in Figure 3.18, there are two distinct regions - Region I (10^{-4} s$^{-1} \leq \dot{\epsilon} \leq 10^{2}$ s^{-1}) and Region II ($\dot{\epsilon} > 10^{2}$ s^{-1}). In Region II, the yield strength increases much faster with strain rate when compared to that in Region I. Polycarbon-

ate does not exhibit strong strain-hardening response (for $\epsilon \leq 0.4$, which is much larger than the local strain values at cell walls during crushing). Therefore, for given strain-rate, the response past the elevated yield stress is modeled as perfectly plastic. The viscoelastic properties are not modeled because it is assumed that the stress relaxation effects are small to negligible owing to the small time duration in which the crushing takes place.

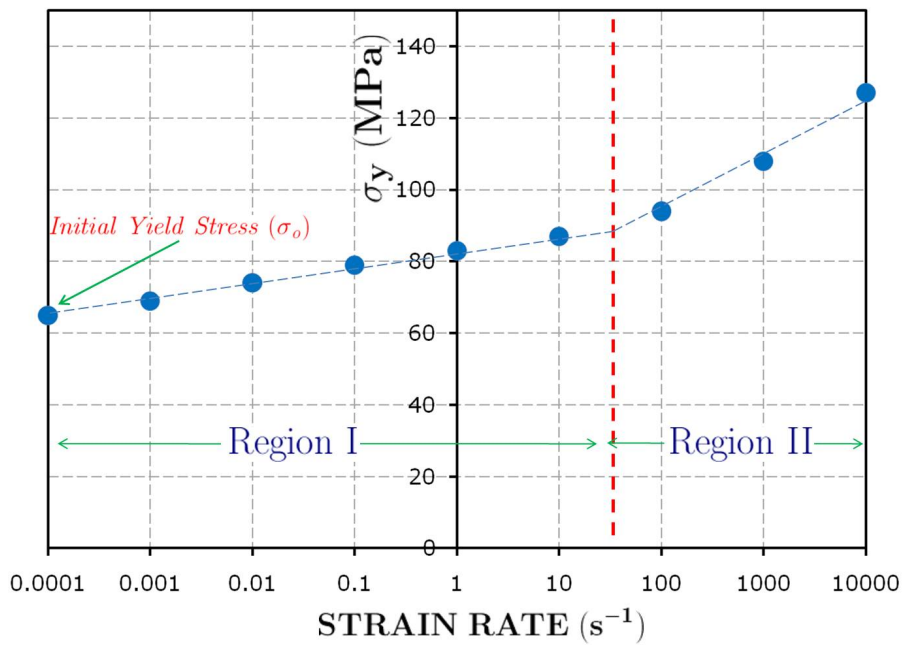

Figure 3.18: The rate dependent compressive behavior of polycarbonate taken from Mulliken & Boyce (2006). Note the two regions where polycarbonate exhibits different rate dependent behavior.

Friction coefficient of $\mu = 0.31$ was used for both polycarbonate-polycarbonate contact and polycarbonate-steel contact to simulate sliding behavior between these two types of surfaces during crushing. For each type of imperfections discussed in the previous section, simulations were conducted for imperfection amplitudes ranging from $\delta = 0.1\%$ up to 5%. The imperfection was applied to the shell geometry at the start of the ABAQUS/Explicit run. In the experiment, the specimen ends were held by frictional contact and this effect is neglected in the FE model. The boundary conditions used in the dynamic run were as follows: only axial movement was allowed and no rotation constraints were applied on the impact face; whereas

the far end of the specimen was only constrained in translation. For the crush simulations, the incident bar (WLD test) and the striker bar (DIM test) were modeled with with coarse mesh using hexahedral solid elements (C3D8R) with material properties of hardened steel. In the WLD simulation, the striker bar was not modeled because, (1) the displacement information from the high speed camera is known and (2) the wave propagation effects of the specimen are not significant due to high impedance mismatch between hardened steel incident bar and polycarbonate honeycomb at the interface.

In the WLD simulation, the input for the displacements prescribed for the incident bar end was a sequence of near perfect ramp-rest inputs. The actual ramp displacement measured from the experiments strictly did not vary linearly with time. Moreover, the displacement-time input for various experiments varied slightly in displacement values, but the duration of the ramp for each loading cycle was consistent. To reduce the simulation run-time, the start and end points of each ramp were averaged and only values at the end points were provided in the displacement-time input for the 3-cell and 7-cell FE simulations. Representative crush velocity of 5,000 mm/s was used as input to the striker bar for all the 3-cell and 7-cell FE models simulating the DIM experiments. The center node along each contact strip was constrained against out of plane motion to prevent beam-like global buckling. This point constraint is valid as it does not over-constrain the structure and does not interfere with the physics of axial crushing.

3.7.2 Simulation Results and Discussion: Wave loading device (WLD) method

In the initial stages of loading, the deformation in the 3-cell and 7-cell specimens was purely axial and the load rose linearly to a peak. This type of behavior agreed well with that seen in the experiments. Thereafter, folds appeared on either sides and the load dropped. The folds disappeared at the far end of the specimen and the folding progressed at the impacted end. Fold

formation took place as long as the impacted end was in motion and the load rose again in the process. During the rest period, the cells were shown to exhibit hoop-like modes, similar to the ones observed in the experiment. Here, the load fluctuated about a value lower than that when the impacted end was in motion. When the next ramp step occurred, the load rose again with more fold formation. The load dropped again when the impacted end was at rest. This cycle continued and the simulations ran for a crush length of approximately 10 mm. For the 3-cell model, the crush load obtained from the simulation was 50.45 $\pm$ 12 N when compared to the mean crush load of 54 N measured from the experiment. The images from the simulations for 3-cell and 7-cell models are shown in Figure 3.19. For the 7-cell model, the crush load obtained was 158.8 $\pm$ 12.2 N compared to the experimental mean crush load of 159 N. The load-time and displacement-time plots for 7-cell specimen for varying imperfection amplitudes are shown in Figure 3.20. The average and standard deviation calculation for the plateau load from FE simulations was performed only during the ramping motion of the incident bar. The mode of collapse was by concertina-diamond fold formation which was similar to the mode of collapse seen in the experiments. It is not possible to do a side by side comparison of the experiment and the simulation, since the FE analysis uses a rendition, based on initial eigenmode shaped geometrical imperfections, of the actual model. It was observed from the simulation results that the type and amplitude of imperfections had no effect on the collapse mode and little effect on the peak and crush loads. Also, irrespective of the severity of imperfections with regard to the type of modes considered, the fold initiation took place at either end soon after the peak load was attained. These observations are encouraging and lends credence to the method of analysis that has been adopted.

3.7.3 Simulation Results and Discussion: Direct impact method

During the initial stages of loading, the load rose to a peak (maximum) load. The deformation in the specimen was only axial up to this point. Folding initiated near the ends of the specimen

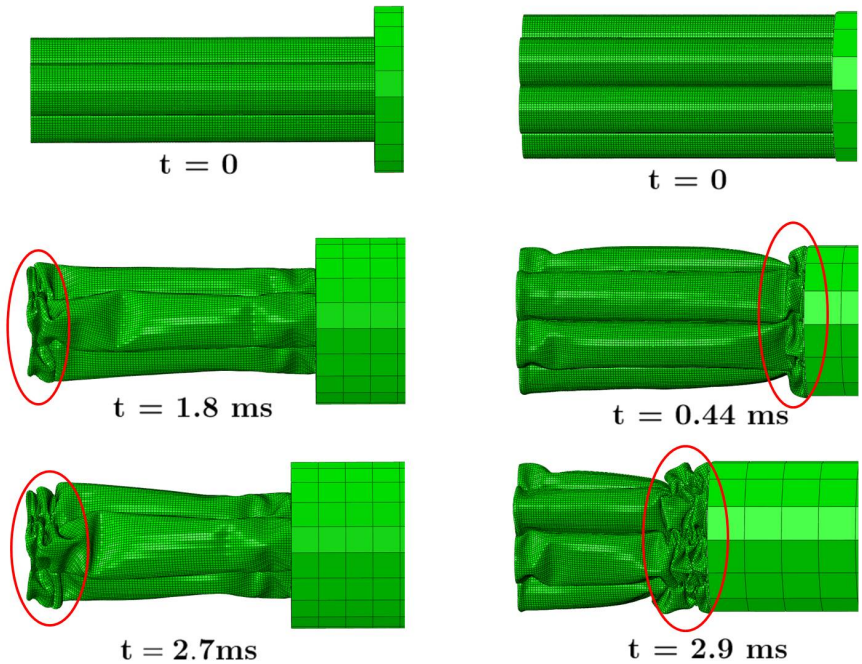

Figure 3.19: Images from the FE dynamic crush simulation of 3-cell and 7-cell models with WLD inputs. The folds appear soon after the peak load is attained. The collapse occurs through the localized concertina-diamond mode.

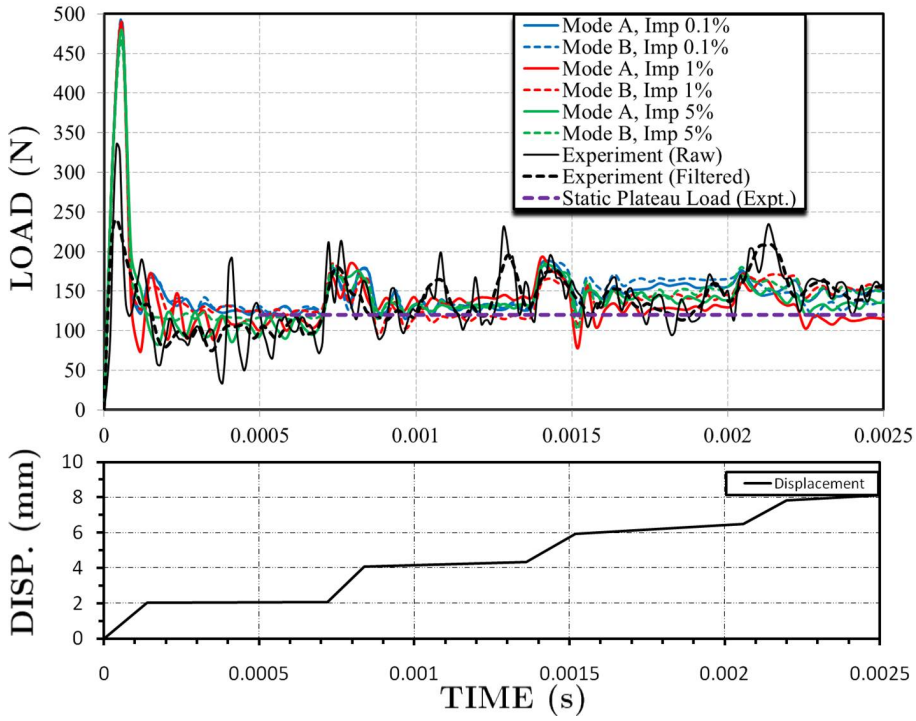

Figure 3.20: Load-time plot for 7-cell specimen FE simulation with the ramp-rest WLD input. The mean plateau load level (120 N) for static crush of 7-cell honeycomb is shown for comparison.

and the load dropped quickly. New folds were formed due to the constant rate of crushing and the load stabilized at an approximately constant level, which is referred to as the crush load. In the 3-cell model, it was observed that the impact end of the specimen which showed localized deformation, recovered elastically nearly to the original shape. The load decreased for a while immediately after the peak and stabilized at the crush load. The folding progressed from the region where fold initiation took place towards both the sides of the specimen. The images from the simulations for 3-cell and 7-cell models are shown in Figure 3.21. The load-time and displacement-time plot for a 7-cell model for various imperfection amplitudes are shown in Figure 3.22. For the 7-cell model, fold initiation took place at both ends and the specimen progressively crushed from these ends. The crush load observed for the 3-cell specimen was 50.54 ± 8.4 N compared to the experimentally measured mean crush load of 51.5 N. For the 7-cell specimen, the crush load obtained from the simulation was 148 ± 14.2 N compared to the crush load value of 157 N seen in the experiments. Hence, the estimate of crush loads during progressive collapse is close to that measured from the experiment.

It is noted that the difference in peak collapse load between simulation and experiment is large, especially in the case of the DIM study. The peak loads measured from the experiment varied significantly among specimens (from no noticeable peak, to about 190 N as seen in Fig. 12 for the 7-cell specimen) whereas the crush load was consistent. In contrast, in the WLD case with 7-cells, the variation in the measured peak load was somewhat consistent between 330 - 400 N. One of the reasons for this difference in the peak value is due to unknown and unintended geometrical imperfections present in the sample. Furthermore, in the DIM experiment, there is uncertainty as to the angle of the striker bar with respect to its "straightness" in trajectory. This reduction in the peak collapse load due to misalignment in loading (as shown by Wilbert *et al.* (2011) for hexagonal aluminium honeycomb system) is another reason for large difference in the initial peak load value.

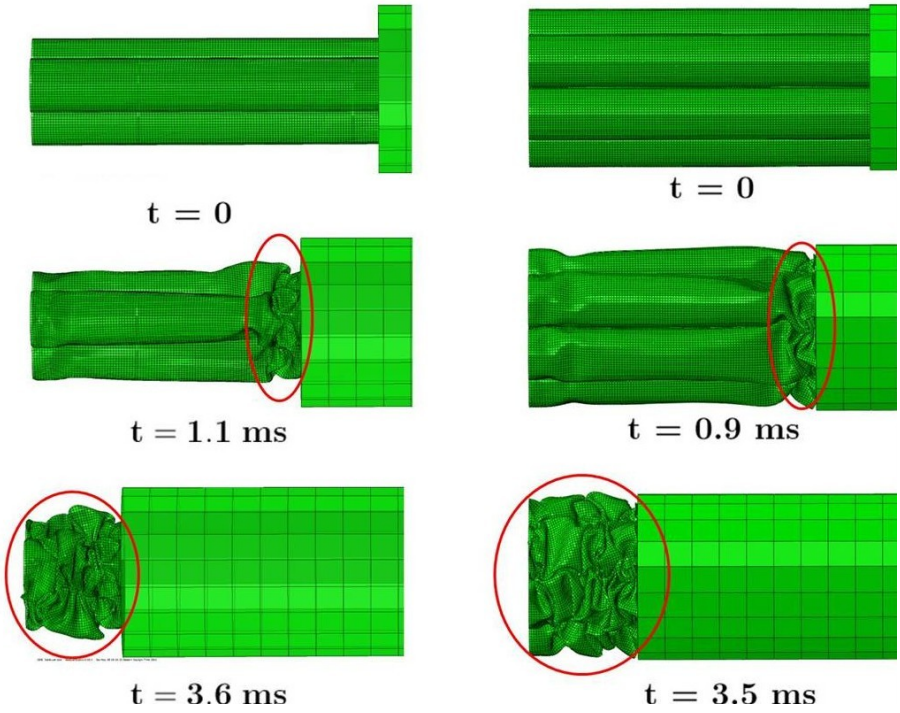

Figure 3.21: Images from the FE dynamic crush simulation of 3-cell and 7-cell models with loading velocity 5,000 mm/s (DIM simulation). Crushing occurs through the concertina-diamond mode.

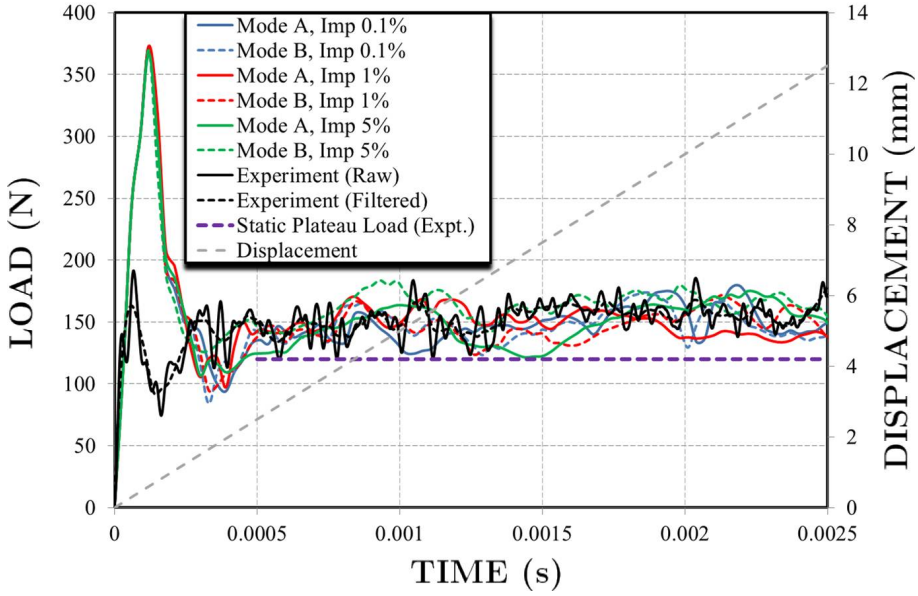

Figure 3.22: Load-time plot obtained from FE simulation for 7-cell specimen being crushed at the rate of 5,000 mm/s (DIM simulation). The mean plateau load level (120 N) for static crush of 7-cell honeycomb is shown for comparison.

3.7.4 Variation of local strain rates and plateau stress with crush velocity

Next, variation of local strain rates with the crush velocity for the 3-cell and 7-cell models is discussed. When the honeycomb crushing occurs, the strain rates experienced by the honeycomb walls are different for varying crush velocities. From the explicit FE simulations that were carried out on the 3-cell and 7-cell models, several locations were monitored on the cell walls where severe fold formation occurred. For a given model and crush velocity, strain rates were found to not differ by a significant amount in magnitude. At a typical such location, the time histories of these quantities were averaged, and the variation of (averaged) strain rates and plateau stress with various crush velocities are provided in Figure 3.24, along with the maximum amplitudes of strain rates over the time history. The results show that with an increase in crush velocity, strain rate and crush loads increase. At such locations, the bending and membrane strains were found to increase with increase in crush velocity. Furthermore, the model predictions are seen to agree with the experimental data corresponding to the crush velocity of 5,000 mm/s. It is also observed that for a given crush velocity, the strain rate values for a 3-cell and 7-cell model are not significantly different, suggesting that results for specimens with a larger number of cells would be similar. We have verified this with DIM simulations of 3-cell, 4-cell, 7-cell, 13-cell and 19-cell models that were each crushed at a velocity of 5,000 mm/s. A plot showing normalized values (i.e. load per cell) of the crush and peak loads for the mentioned cell numbers, is shown in Figure 3.23. It is observed that the plateau load per cell for the 7-cell model is higher than that for the 3-cell model by $\approx 40\%$ Ḟor the 13-cell and 19-cell specimens, the plateau load per cell is $\approx 8\%$ and $\approx 20\%$ respectively higher than the 7-cell specimen, suggesting that this load asymptotes to a constant value of $\approx$ 24 N as can be seen in Figure 3.23.

With reference to Figure 3.24, note that for an increase in crush velocities, the normalized plateau stress (calculated as $P_{plateau}/NAE$ where $P_{plateau}$ is the average plateau load, $A = 2\pi Rt$ is the true contact area, E is the static Young's modulus of polycarbonate and N is the

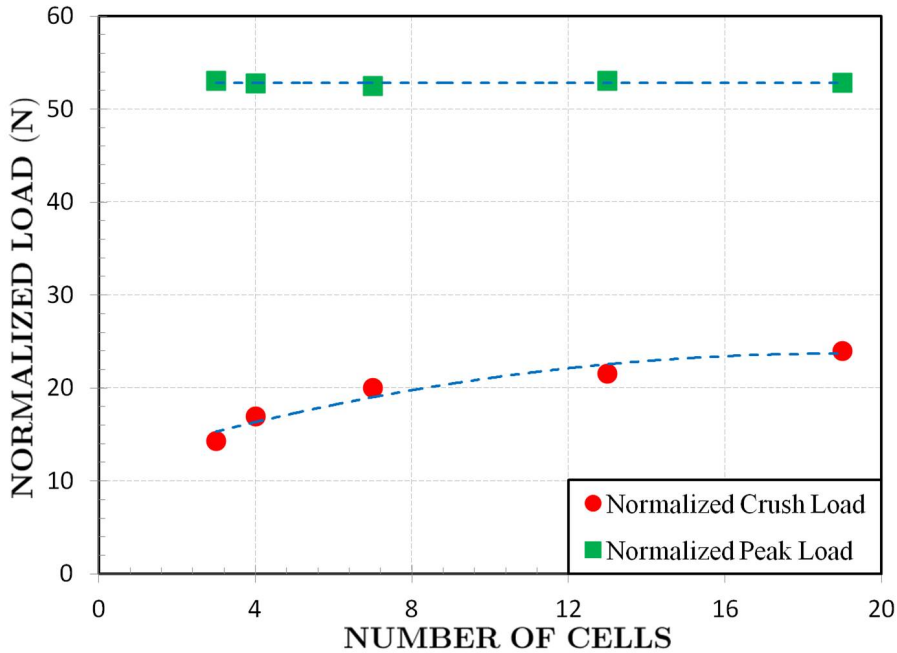

Figure 3.23: Plot showing the FE simulated crush and peak load values that are normalized by number of cells for 3-cell, 4-cell, 7-cell, 13-cell and 19-cell specimens. Each of the specimens were crushed at the rate of 5,000 mm/s (DIM simulation) to study the effect of cells-per-specimen on the crush and peak load.

number of cells in the specimen) slightly increases indicating that rate effects do play a role in the axial crush response. The normalized plateau stress calculated from the static 3-cell and 7-cell experiments are also provided in Figure 3.24 to enable comparison with the dynamic crush experiment DIM. The normalized plateau stress values for static crush experiments are lower than the DIM experiment (at crush velocity 5,000 mm/s) and FE predictions provided, thus indicating the presence of rate effects. More specifically, comparing the dynamic crushing (at 5,000 mm/s to the static crushing), the Figure 3.24 shows only a slight increase for the 3-cell specimen, i.e. an increase of about 5% compared to an increase of about 10% for the 7-cell specimen. The comparatively higher increase in load for the 7-cell specimen is due to the higher degree of lateral constraint that is provided to the cells as the number of cells increase. Figure 3.25 shows the contribution of a single cell in a 3-cell model and an outer layer and innermost layer cell in a 7-cell model when these corresponding 3-cell and 7-cell specimens were crushed at a uniform velocity of 5,000 mm/s. Amongst the three types of cells

distinguished here, the plateau load levels is largest for the innermost cell in the 7-cell model (most constrained with 6 double wall sites along the circumference) and is lowest for a cell in the 3-cell model (least constrained with 2 double wall sites along the circumference). Moreover, the lateral constraint has the effect of slightly delaying the first failure event as can be seen from the peak loads in Figure 3.25.

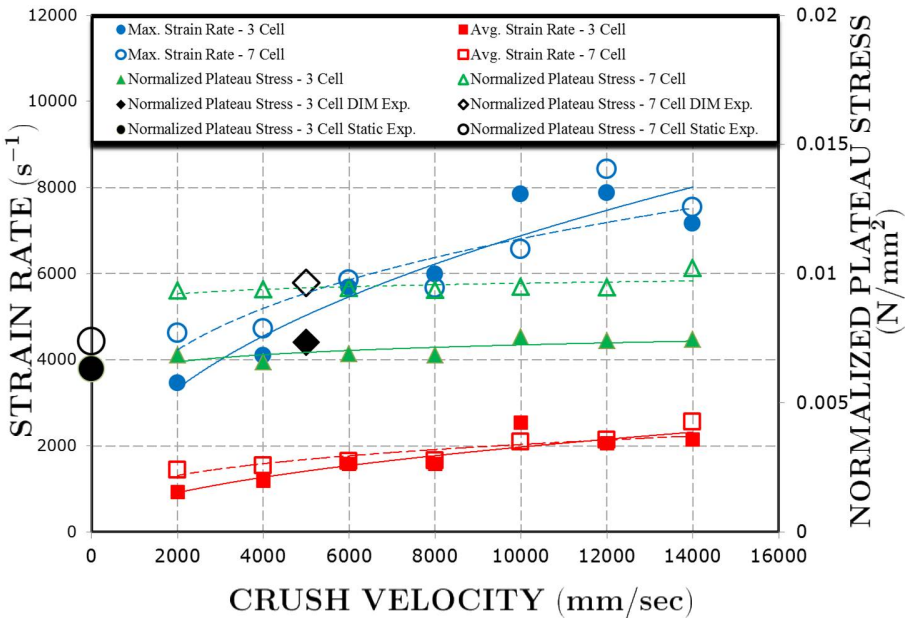

Figure 3.24: Plot showing the variation of material strain rate and normalized plateau load per cell with crush velocity for 3 and 7-cell models. For crush velocity of 5,000 mm/s (Direct impact method), the experimental normalized plateau stresses for the 3 and 7-cell are also shown. The normalized plateau stress, a non-dimensional quantity, is calculated as $P_{plateau}/NAE$ where $P_{plateau}$ is the plateau load, $A = 2\pi Rt$ is the true contact area and E is the polycarbonate Young's modulus for an N-cell honeycomb. Also shown is the normalized plateau stress for 3-cell and 7-cell static crush experiments.

3.8 Conclusions

The crush response of 3-cell and 7-cell circular cell honeycombs was studied using two methods - the wave loading device (WLD) method and the Direct impact method (DIM). The crush velocities seen in the WLD method are higher ($\approx$ 12,000 mm/s) compared to those in the DIM ($\approx$ 5,000 mm/s). The collapse of 3-cell and 7-cell specimens occurred over a constant state of crush

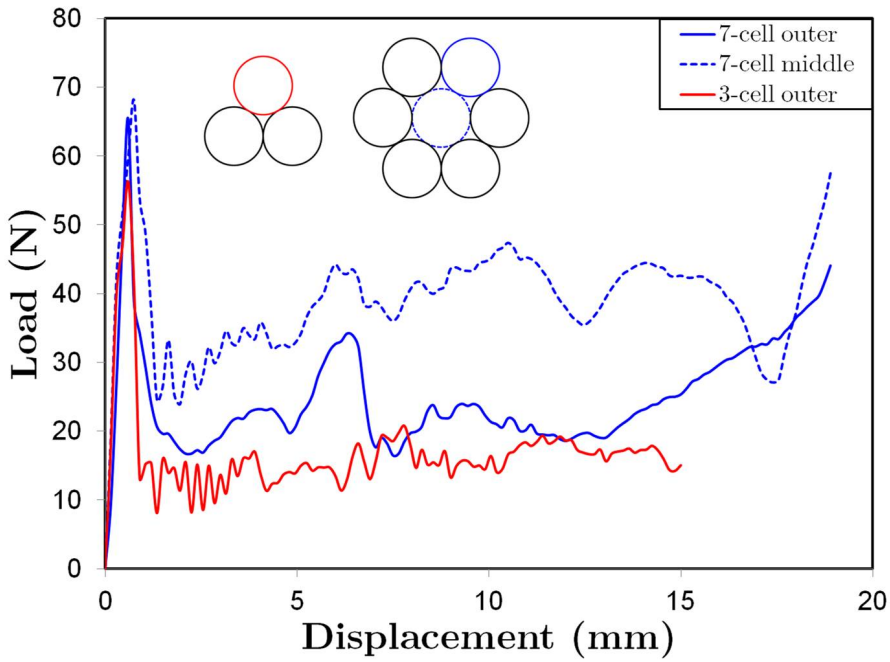

Figure 3.25: Plot showing the load response for the outer cell for a 3-cell model and outer and innermost cells in 7-cell model and pointing towards the influence of lateral constraints at the double-wall site on the plateau load.

load at these crush velocities. Mean crush loads for the specimens measured from the WLD experiments were slightly higher compared to that measured from DIM experiments. Moreover, higher crush load levels were measured in the DIM experiment for 3-cell and 7-cell honeycombs compared to corresponding static crush experiments, thus clearly showing the presence of rate effects in the crush response. The peak load measured from the WLD experiment was higher than that from the DIM. This is evident because the deceleration force upon impact increases when the crush velocity is larger. The crush initiation took place at one or both ends of the specimen. The mode of collapse of the honeycombs was through localized concertina-diamond fold formation that progressively propagated from the specimen ends until the entire specimen had crushed. A series of FE simulations were conducted using eigenbuckling modes to approximate the imperfect geometry of the honeycomb. These simulations satisfactorily captured deformation features observed in the experiment, thus providing a meaningful way to estimate the energy absorption of clusters of cells. Beyond the stiff initial response, the load at which

progressive collapse took place was found to be fairly close to that measured from the experiments. Moreover, the plateau load occurring with the concertina-diamond mode of collapse was found to be insensitive to the type and amount of geometrical imperfections.

Chapter 4

Static out-of-plane crush response of filled honeycomb

4.1 Introduction

Several studies have been conducted in addressing the problem of static axial crush of honeycombs. In particular, Mellquist & Waas (2004) have studied the static, crush response of circular cell polycarbonate honeycombs in the out-of-plane (axial) direction. They reported that after the initial collapse (corresponding to the *peak load*), folding initiates in the structure accompanied by drop in the load. The sudden load drop is termed as *unstable collapse*. Thereafter, the cell continues to carry load at a fairly constant state of load which is referred to as the *plateau load*. They concluded that the localized concertina-diamond fold formation was the dominant mode of failure in these structures. They also reported that scaling, in terms of the number of cells per specimen, has no influence on the plateau load. The out-of-plane static crush response of hexagonal cell aluminum honeycombs have been examined through experiments and explicit finite element simulations by Wilbert et al. (2010). In these honeycombs, the cell walls are flat

plates, and the plates are joined along some of the walls, to neighboring cells, a result of the efficient manufacturing process of these honeycombs as described in Gibson and Ashby (1997).

In this chapter, the out-of-plane axial crush response of filled polycarbonate honeycombs are studied, motivated by our earlier work (D'Mello et al., 2012) on high rate axial crush response of unfilled circular honeycombs. The main objective of this study is to investigate the influence of the filler on the load response and mode of failure. In particular, we show a synergistic energy absorption phenomenon, leading to an amplification of energy absorption, as a direct result of the filler material influencing the mode of cell deformation, compared to the corresponding, unfilled honeycomb deformation mode. 3-cell, 7-cell and 19-cell polycarbonate honeycomb microstructures, both, unfilled and filled, are used in the experimental studies. Polyurethane, a soft elastomer is used as the cell filler material. A representative diagram of the 3-cell honeycomb with contact sites is shown in Figure 4.1.

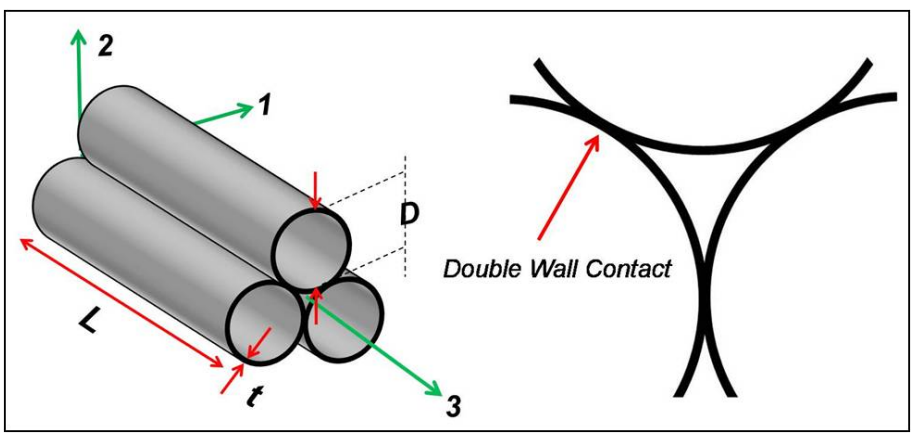

Figure 4.1: Schematic of a 3-cell specimen showing the cell length (L), wall thickness (t) and cell diameter (D) is shown to the left. The out-of-plane loading direction is in the 3-direction. The double wall contact over a line is shown in a diagram to the right.

4.2 Sample preparation & test setup

The honeycomb specimens were procured from Plascore Inc., Zealand, MI. The physical dimensions of the honeycombs were measured using a low-magnification optical microscope study. The out-of-plane length was 24.5 mm, the cell wall thickness was 0.065 $\pm$ 0.005 mm and the cell radius was 2.108 $\pm$ 0.39 mm. Each cell is in contact with its neighbor at through an area contact. The double wall thickness and the cell adhesion length measured 0.133 $\pm$ 0.006 mm and 0.227 $\pm$ 0.027 mm respectively. The material properties of the polycarbonate material were assumed to be isotropic. A single cell was crushed in a uniaxial testing machine and the load response was backed out by simulating this experiment in ABAQUS/Standard and matching the slope of the load-deflection curve. The Young's modulus of the specimen was found to be 2600 $\pm$ 200 N/mm. Polyurethane solution is first prepared and poured into a cylindrical mold (diameter 22.8 mm and length 25.4 mm) containing the honeycomb. The polyurethane-honeycomb sample is cured at room temperature for 5 days. A schematic in Figure 4.2 shows the cross-section of the filled 3-cell, 7-cell and 19-cell specimens.

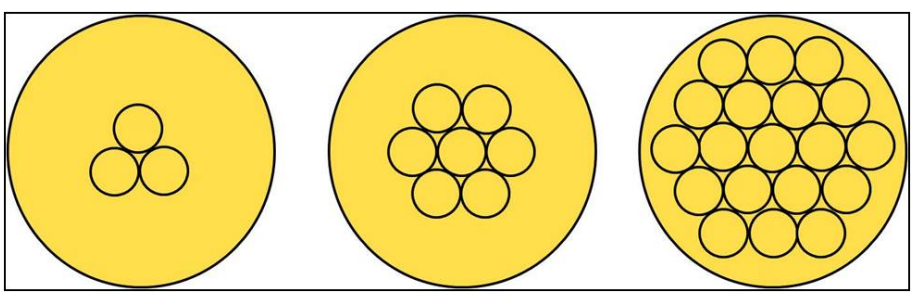

Figure 4.2: Cross section of the 3-cell, 7-cell and 19-cell specimens filled with polyurethane.

4.3 Experiments: Polyurethane as the Filler Material

4.3.1 Static Uniaxial Compression of Polyurethane

The polyurethane block having the same dimensions as the mould was tested under similar loading conditions as mentioned above. Lubricating oil was applied at the loading surfaces to reduce the influence of friction on the test specimen. A set of images taken from the experiment are provided in Figure 4.3. For the macroscopic strain (end crushing over initial length) of 0.25 onwards, prominent barreling was observed. The specimen was compressed up to 90% of its length. Upon unloading, the specimen regained nearly to its original length. The load increases at a lower rate up to macroscopic strain of 0.5 and thereafter rises rapidly with increased crushing. The uniaxial loading-unloading plot is shown in Figure 4.4 shows some hysteresis in the specimen. This information from this experiment is crucial for characterizing the hyperelastic properties of polyurethane for use in the finite element crush simulation. Moreover, this test also will also serve to compare the contribution of the filler material when filled honeycomb specimens are subject to uniaxial static compression loading.

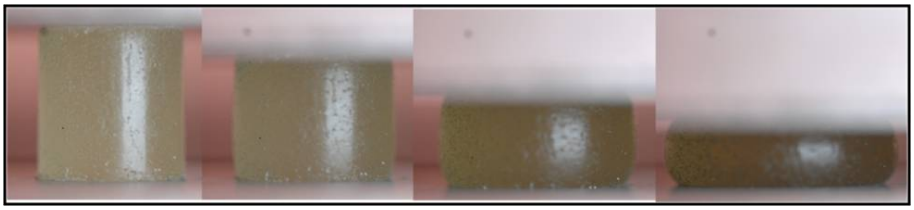

Figure 4.3: Image sequence taken from the quasi-static uniaxial compression test of polyurethane block corresponding to macroscopic strains of 0, 0.22, 0.48 and 0.70.

4.3.2 Static crush response of filled honeycombs

Static axial crushing experiments on filled 3-cell, 7-cell and 19-cell specimens were conducted under similar testing conditions described in the previous section. Here, the main features of response pertaining to the three types of filled specimens under study is discussed. The

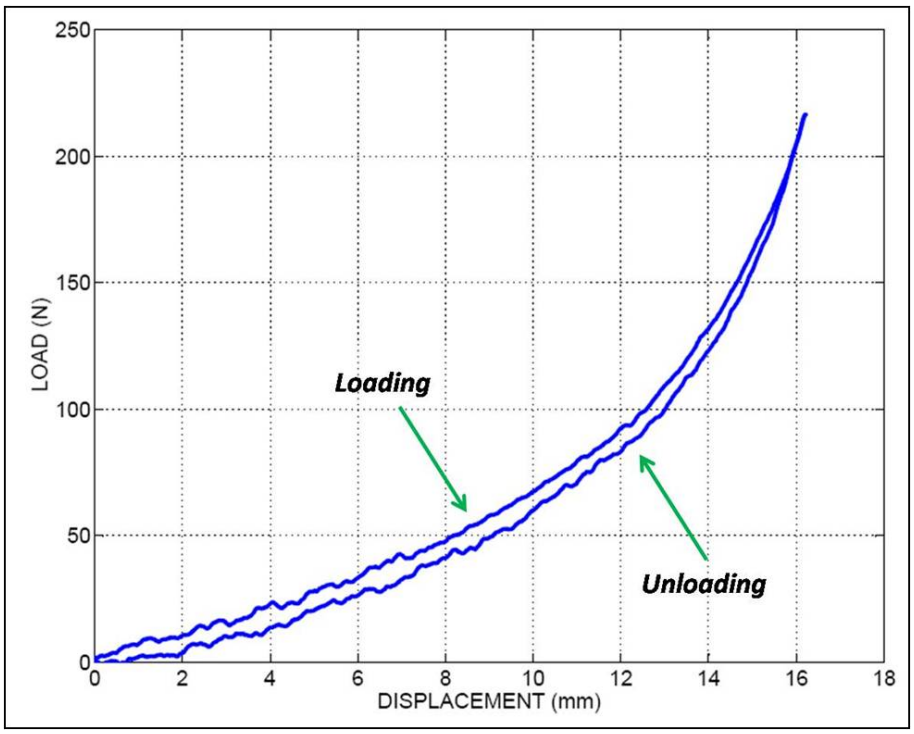

Figure 4.4: Load-deflection curve of polyurethane sample undergoing compression loading followed by unloading.

load-displacement plots for the 3-cell, 7-cell and 19-cell specimens are shown in Figure 4.5, Figure 4.6 and Figure 4.7 respectively. These figures also contain the crush response plots of corresponding unfilled honeycombs and that of the polyurethane block to enable comparison of filled and unfilled honeycomb response and assess the contribution of the polyurethane material during various stages of loading. During the initial stages of loading, typically up to crush distance of less than 1 mm (corresponding to a macroscopic strain of 0.04), the load response was fairly linear. The contribution of the polyurethane material to the total load response up to this point was marginal and the confined honeycomb carried majority of the load. The filler material is colored and therefore, this phenomenon is not captured clearly in the images. However, upon inspection of the failed specimen, we concluded that folds were the first to form before another type of failure - longitudinal tearing, which will be described subsequently. (The circumferential folds were continuous across the region where longitudinal tearing had occurred thus suggesting that folds were indeed the first to form. Moreover, the macroscopic strain value

at first failure was very close to the macroscopic strain corresponding to the first localized failure of the unfilled specimens.) The structure still carried load and catastrophic failure was not observed at first failure. Hence, the first failure can be described as a stable collapse. Unlike the case of unfilled honeycombs, the stable collapse that is seen in the filled crushing is because localized folds are not completely formed at once due to the presence of the filler material; hence the drop in load is less. In other words, the filler material acts as a cushion in the event of localized collapse. From the load-response plots, the crush distance where the initial failure took place is fairly close to that for the unfilled honeycomb. As loading progressed, localized folds continued to form at a near-constant load value. The load level beyond the initial stable failure is much higher compared to the plateau load of the unfilled honeycomb specimen. This suggests that the load carrying ability of the cells has been vastly enhanced when they are confined with a soft filler material.

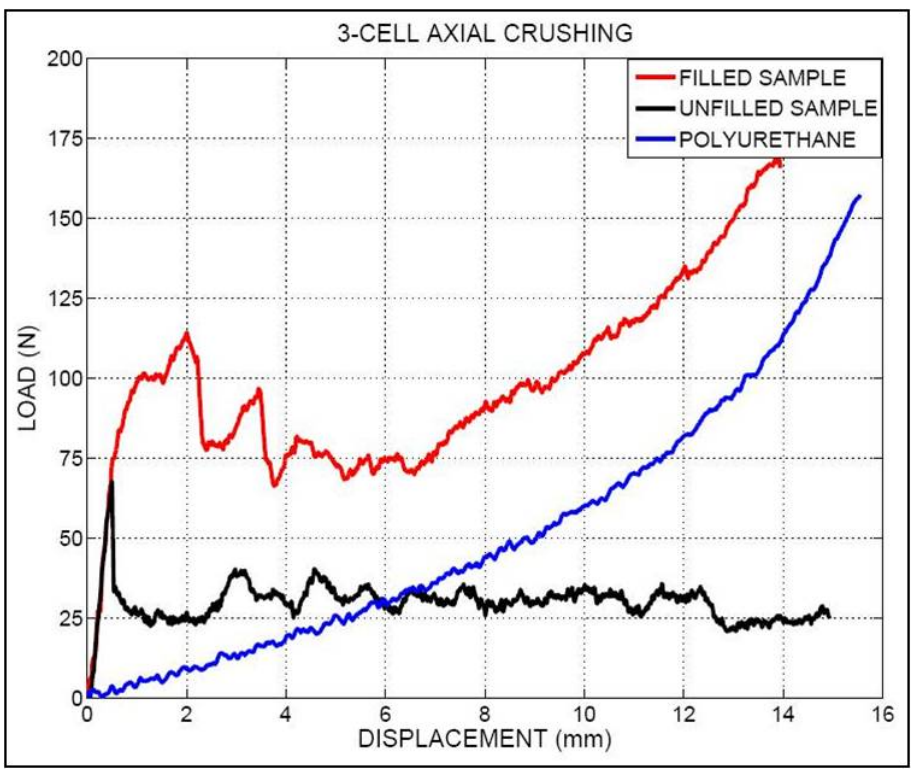

Figure 4.5: Load response of a filled 3-cell specimen shown against that of an unfilled 3-cell specimen. The crush response of the polyurethane block is also shown.

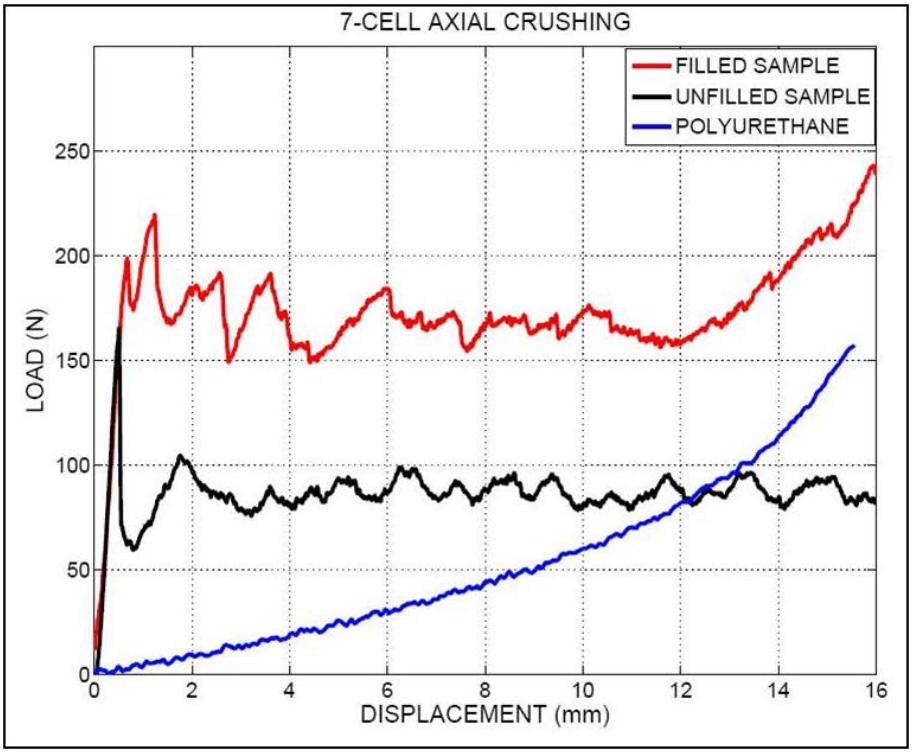

Figure 4.6: Load response of a filled 7-cell specimen shown against that of an unfilled 3-cell specimen. The crush response of the polyurethane block is also shown.

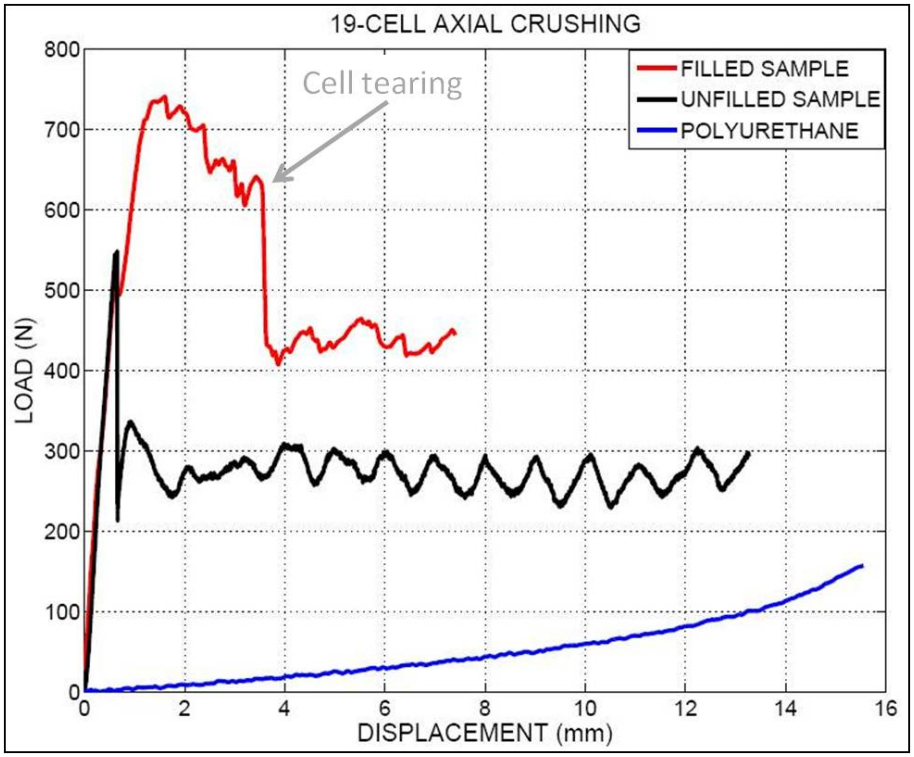

Figure 4.7: Load response of a filled 19-cell specimen shown against that of an unfilled 3-cell specimen. The crush response of the polyurethane block is also shown.

With increase in the end-shortening distance, the nearly incompressible filler material began to exert force in the radial direction of the cylindrical block, thus initiating longitudinal tearing of the honeycomb cells, especially those that were present in the outermost layer. Therefore, the longitudinal tearing was more prominent in the 19-cell samples compared to the 3-cell and 7-cell cases. In contrast to the stable failure corresponding to fold formation, the tearing was characterized by a sudden drop in the load and is therefore an unstable failure. With increase in deformation, more tearing was observed and this failure had the effect of lowering the ability of the filled specimen to carry compressive load.

Beyond the initial stable collapse, another type of failure pattern was observed prominently in the 3-cell specimens and mildly in the 7-cell specimens - that of *beam-like* global buckling. This global buckling also leads to longitudinal tearing characterized by fairly sharp drop in the load as can be seen in the load response plot of a 3-cell specimen that is shown in Figure 4.5. However, for specimen with low aspect ratio, 19-cell specimens, global buckling was not observed upon inspection of the damaged honeycomb after the test was complete.

With further increase in crushing, the contribution of polyurethane material to the total load increased and that of the crushing honeycomb decreased. It is also seen that the filled honeycomb that is partially damaged to global buckling and longitudinal tearing, continues to carry load. The shape of the load-response curve is similar to that of the polyurethane filler material, but has a vertical offset which indicates the load carried by the damaged honeycomb.

The deformed specimens of the filled and unfilled 7-cell and 19-cell specimens are shown in Figure 4.11. The localized folds formed were formed at discontinuous sites along the length of the specimen. This behavior is different from the fold formation in unfilled honeycombs where folds typically appeared at one end and propagated sequentially to the other end. Moreover, due to the presence of the filler material on both surfaces of the cell, the localized folds were not completely formed at the crushed end, unlike in the case of unfilled honeycombs. This constrained deformation at the cell walls resisting the fold formation and instead distributing the

folds along the length of the cells (i.e. diffused folding) enables the honeycomb to collapse at a much higher load, in contrast to the unfilled honeycombs where deformation is more localized at the crush end. Therefore, this phenomenon, which is responsible for significant enhancement in the load carrying capacity beyond the initial stable failure, leads to increased energy absorption.

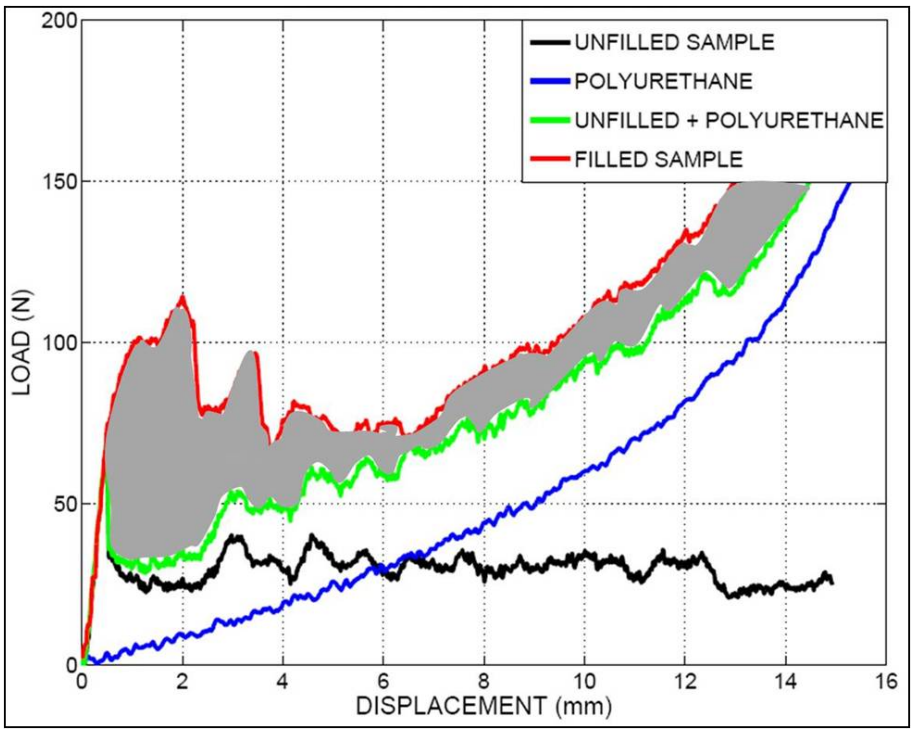

Figure 4.8: The green curve shows the response of the polyurethane block added to the response of the 3-cell unfilled honeycomb. The shaded portion shows synergy in load response for the filled specimen.

It is instructive to compare the load response of the filled specimen with the sum of the responses of the polyurethane block and the unfilled honeycomb. The total response of the block (filled specimen) is greater than the sum of the load responses of the honeycomb and the polyurethane block. This synergetic load enhancement for 3-cell, 7-cell and 19-cell filled specimens is shown in the shaded portions in Figure 4.8, Figure 4.9 and Figure 4.10 respectively. This behavior suggests that the response of the filled specimen is not linear with respect to the individual responses of the unfilled honeycomb and the filler material block. This phenomenon arises due to the fact that the confined honeycomb crushes in a manner differently compared to the case when it is not filled. In the filled case, the filler material interferes with the fold formation,

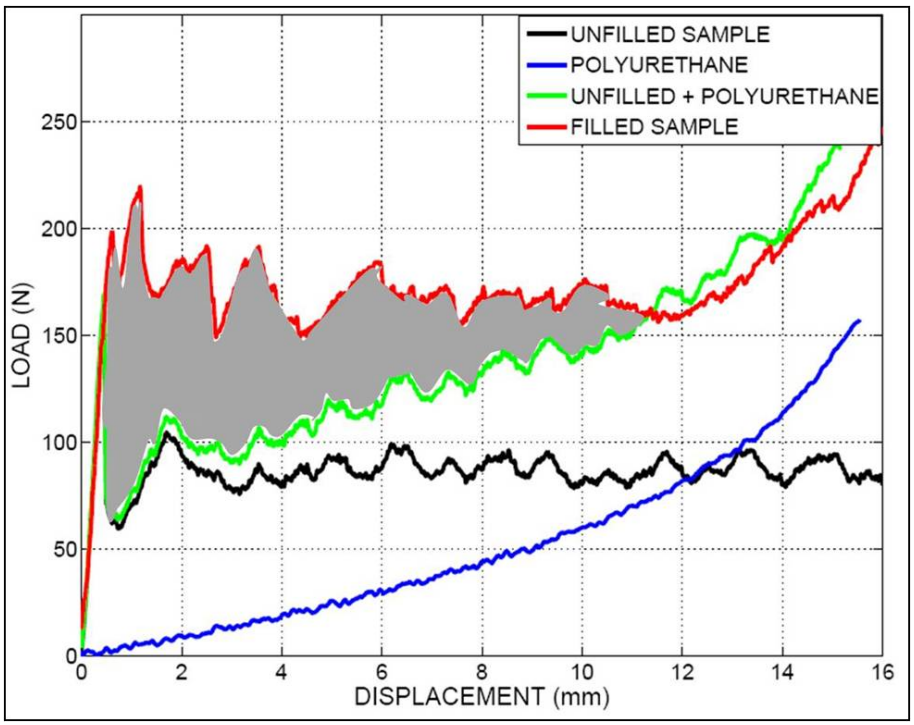

Figure 4.9: The green curve shows the response of the polyurethane block added to the response of the 7-cell unfilled honeycomb. The shaded portion shows synergy in load response for the filled specimen.

making it more difficult for the folds to form.

4.3.3 Load contribution of the honeycomb-infill cylinders

The 3-cell, 7-cell and 19-cell filled honeycombs were prepared in equal sized molds. It is necessary to separate out the contribution of the honeycomb-infill cylinders (HIC) from the total load response. For the filled honeycomb specimen used in this study, the HIC is defined as that part of the specimen that consists of each cell and filler material which lies inside. Therefore, the remaining part of the specimen is the outer layer composed of the filler material. For example, in a 3-cell filled specimen, the HIC consists of three cells and the filler material that lies inside each of the cells. For a given filled specimen consisting of n cells, if $P_T^{(n)}$ is the total response at a particular crush distance, then this total response is a contribution of the load response of the HIC denoted by $P_{HIC}^{(n)}$ and that of the remaining portion of the filler material which is denoted by

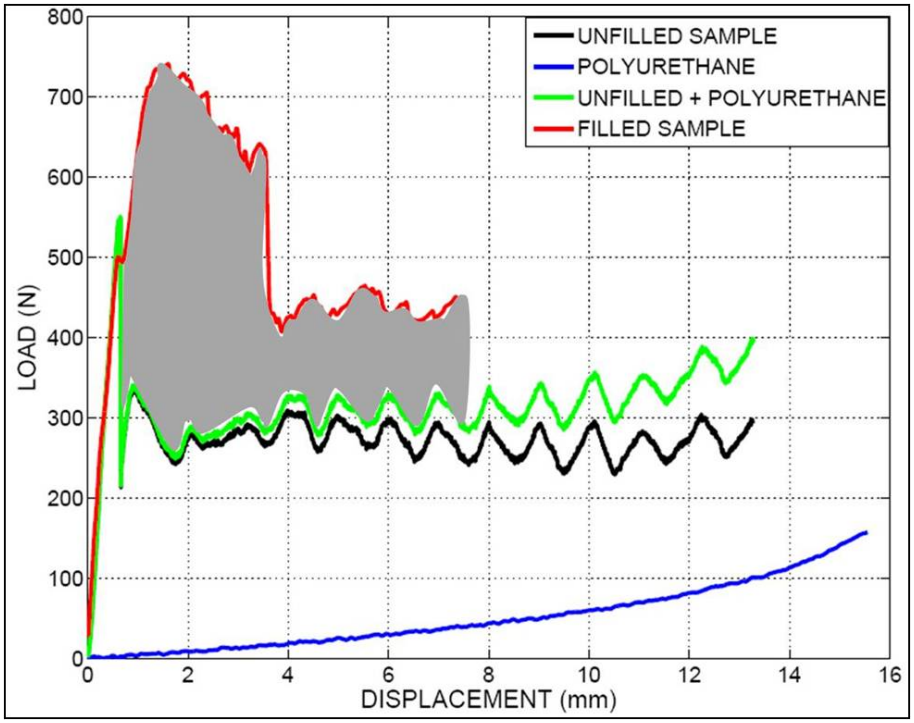

Figure 4.10: The green curve shows the response of the polyurethane block added to the response of the 19-cell unfilled honeycomb. The shaded portion shows synergy in load response for the filled specimen.

Figure 4.11: The images comparing the deformations of filled and unfilled 7-cell and 19-cell honeycombs. The unfilled specimens are shown on the left column and the filled specimens on the right column. Notice the progressive localized failure spread over a continuous region in the unfilled specimens. In contrast, the localized folds in the filled specimens occur in a random fashion. Longitudinal tearing is seen in both the filled honeycombs. In the filled 7-cell specimen, notice some global deformation that is not present in the filled 19-cell specimen due to lower aspect ratio.

$P_R^{(n)}$. Therefore, $P_T^{(n)} = P_{HIC}^{(n)} + P_R^{(n)}$. The response of the outer layer can be obtained from the load-response plot of polyurethane block (P_{fill}), which is of the same size as those of the filled honeycomb specimens. If $V_f^{(n)}$ is the volume fraction of the outer layer, then $P_R^{(n)} = P_{fill}V_f^{(n)}$. Therefore, the response of the HIC is given by $P_{HIC}^{(n)} = P_T^{(n)} - P_{fill}V_f^{(n)}$. The normalized response is then given by $F_{HIC}^{(n)} = P_{HIC}^{(n)}/n$. The normalized load $F_{HIC}^{(n)}$ enables us to compare the amount of load carried by the HIC per cylinder across specimens having different number of filled cells and is shown for 3-cell, 7-cell and 19-cell specimens in Figure 4.12. With reference to Figure 4.12, one observes that the load carried by the all three kinds of specimens considered does not significantly different. The slightly higher response of the 19-cell specimen can be explained due to the fact that it more stable and is not prone to global buckling when compared to the response of 3-cell and 7-cell specimens. Therefore, this plot suggests that scaling in terms of number of cells has no significant influence on the load carrying capacity of the HIC per cylinder of these specimens. Here, it is instructive to recall a similar result for unfilled honeycombs that was reported for static crush response of unfilled specimens by Mellquist & Waas (2004).

4.3.4 Finite Element Simulation

This section presents finite element simulation of a representative filled 7-cell specimen. Here, 7-cell is chosen as a representative sample and simulations described shortly would hold good for specimens with any number of cells. First, the polyurethane compression experiment was validated using hyperelastic model in ABAQUS/Standard. A cylindrical model with dimensions of the polyurethane test specimen was created with reduced integration eight node brick solid brick elements (C38DR). The nominal stress-strain data of the polyurethane sample obtained from the uniaxial crush experiment was used as an input in hyperelastic material definition. Marlow's hyperelastic model was chosen to simulate the hyperelastic behavior of polyurethane. The Marlow's hyperelastic model is best suited when only limited type of test data are present

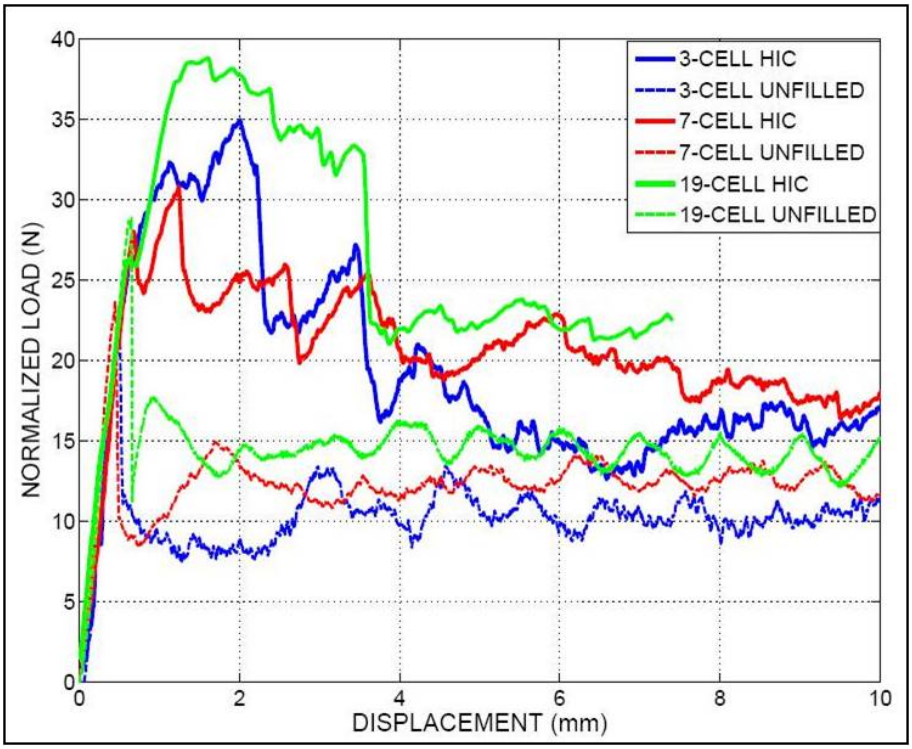

Figure 4.12: Plot showing the normalized load response of honeycomb-infill cylinder for a 3-cell, 7-cell and 19-cell specimens. The normalized load per cell for the corresponding unfilled honeycomb is also shown.

- in our case, being the uniaxial test data. Before proceeding with the simulation of the filled honeycomb, it is instructive to understand how the boundary conditions at the top and bottom conditions influence the uniaxial compression response of polyurethane. For the first set of simulations, the top and bottom faces of the model were held against movement in the radial direction. The bottom face was fixed in the axial direction and displacement was specified at the top face. The stress-strain plot was backed out and the result was in close agreement with that observed in the experiment. Owing to the incompressibility of the polyurethane material, the onset of barreling was seen for macroscopic strain of 0.25. For the next set of simulation, the top and bottom surfaces were assumed to be frictionless. The stress-strain plot backed out was again, in close agreement with the experimental data and was negligibly lower than that from the first simulation set. Since in the experiment, the constraint at the top and bottom faces of the specimen lie in between these two extreme cases considered in the simulation, the data obtained from the uniaxial compression test is assumed characterize the polyurethane closely.

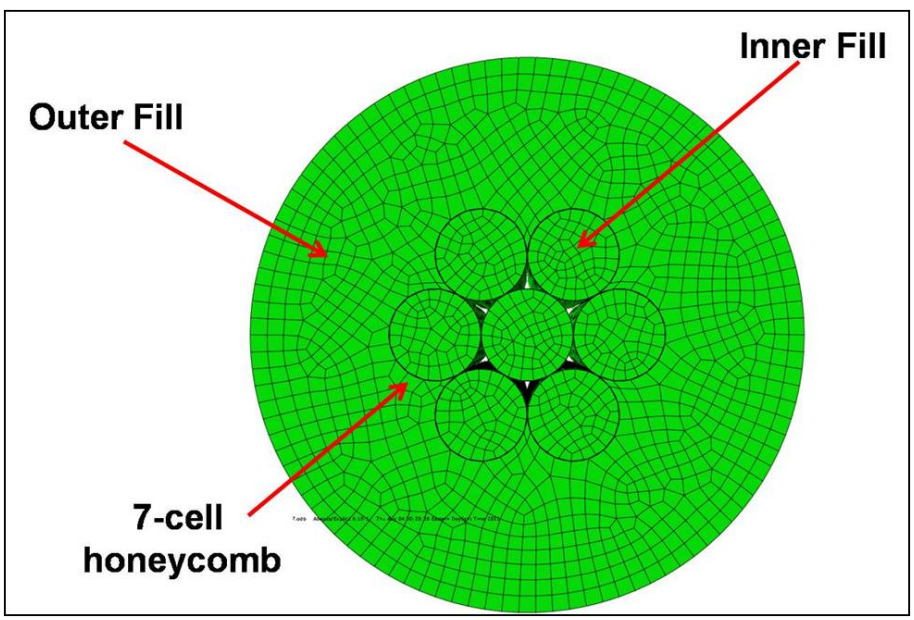

Figure 4.13: The finite element mesh (top view), showing the honeycomb filled with polyurethane (Inner Fill) and surrounding it (Outer Fill). The space formed where three cells meet is not filled to make the explicit crush simulation more computationally affordable by reducing the surface-to-surface constraints.

Finite element model of a 7-cell honeycomb was created using S4R shell elements using the dimensions of the honeycomb microstructure. The mesh contained 12, 928 nodes and 13, 482 elements. In this model, ideal shell-to-shell contact was assumed, i.e. each cell was in contact with its neighbor through point contact. The real honeycomb cell deviates from the perfect geometry due to presence of localized geometrical imperfections, non-uniform wall thickness, out-of-roundness and non-uniform cell-to-cell contact. Out of these, the crush response is most influenced by the presence of geometrical imperfections (Babcock, 1983). Linear eigenbuckling analysis was conducted and the first eigen mode was chosen to seed the honeycomb structure in the filled specimen model. Geometrical imperfections were added to perturb the perfect geometry of the shell elements with imperfection amplitudes. The method adopted to arrive at determining imperfection levels that were representative of geometrical imperfections of real honeycombs was as follows: The maximum deviation from perfect circular shape was calculated using measured cell dimensions. The maximum deviation in cell radius value was 0.36 mm, which corresponded to approximately 5.5 times the wall thickness. Using this estimate, the imperfection amplitude of 0.128 and 0.194 (corresponding to 200% and 300% of the shell wall thickness) were chosen such that the initial slope of the resulting unfilled crushing simulation was not significantly different from the initial slope measured from the unfilled static crush experiment. The inner filling and outer cover containing polyurethane was created using reduced integration eight node solid brick elements (C38DR). The top view of the finite element model is shown in Figure 4.13. In order to simulate the bonding between the filler material and the shell, the surface nodes of the shells were tied to those of the surrounding solid elements using the surface-to-surface tie constraint. Hence, through this constraint, perfect bonding was assumed between the honeycomb and filler material interface. ABAQUS/Explicit was used to simulate the crushing response because it is computationally efficient, given the complexity and the interactions present in the model. The boundary conditions were specified as follows: the top and bottom surfaces of the model were constrained in the radial direction. The bottom surface was constrained in the longitudinal direction and crush velocity of 10 mm/sec was specified

at the top surface. The kinetic energy of the structure was much smaller compared to the strain energy of the structure and therefore, the use of such prescribed velocity to mimic the quasi-static response was justified. Rate dependent data for the polycarbonate material was taken from Mulliken & Boyce (2006) with the initial yield stress of 66 MPa. However, due to the low local values of strain-rate, the rate effects have marginal influence on the crush simulation. The crush simulation of unfilled 7-cell honeycomb model was also performed with inputs similar to the one described above for the case of filled honeycomb. Next, we describe in parallel the crush simulation response of filled and unfilled 7-cell models.

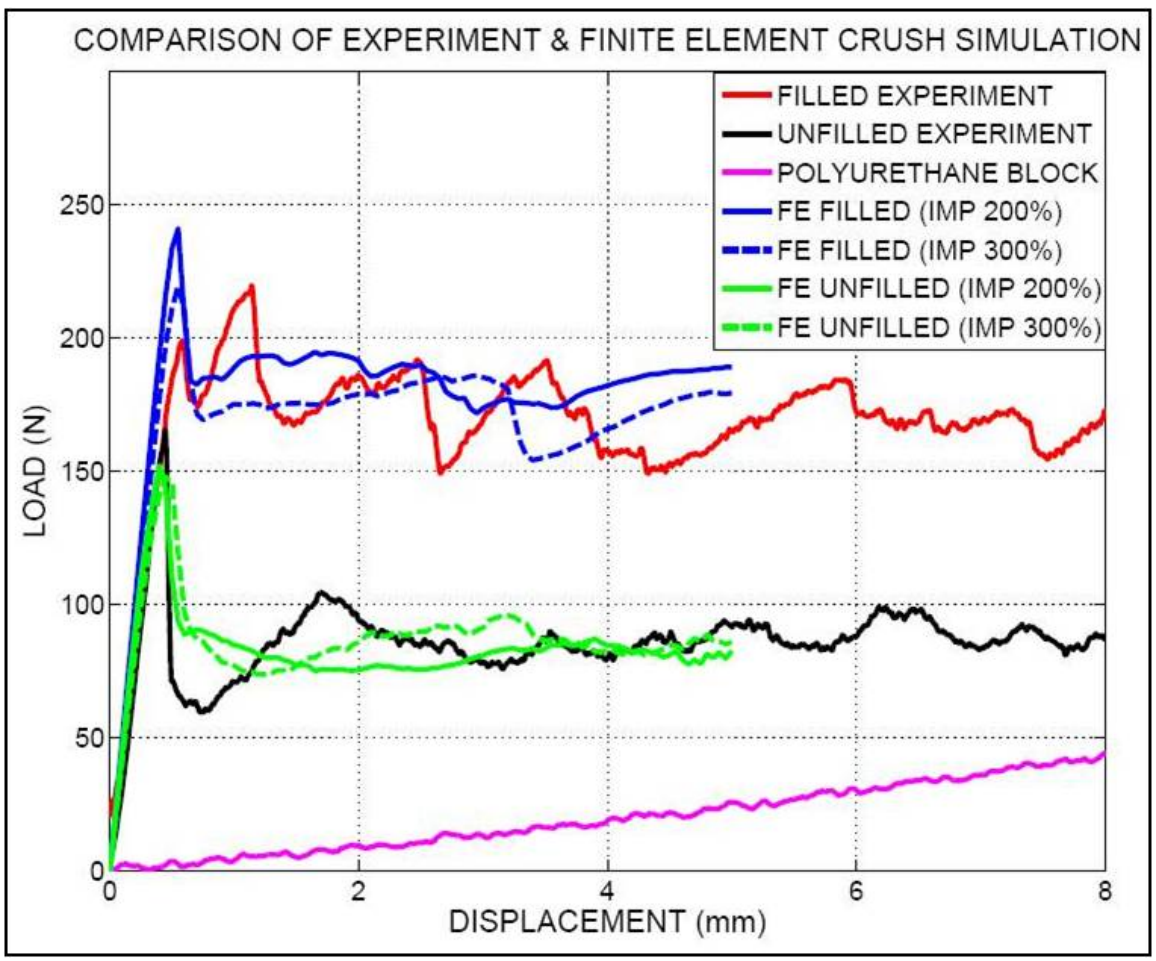

Figure 4.14: Plot showing the comparison of the load response of 7-cell honeycomb experiments and finite element simulation for both filled and unfilled honeycombs.

The load vs. end-shortening plot of the two models is shown in Figure 4.14. The load response

of the 7-cell filled honeycomb model was linear during initial stages of loading and the load peaked to a maximum (peak load) and dropped. This load drop was accompanied by localized fold formation near one of the ends. The unfilled model also showed a linear regime with slope very close to that of the filled model. However, here, the peak load was lower than that of the filled model and was accompanied by localized fold formation with folds being localized at the ends, whereas the buckling pattern is diffused in the case of the filled honeycombs. Thereafter, the load response for both the models was fairly constant (plateau load) where more folds were formed. New folds were completely formed once the previous folds were nearly complete. In the case of the filled model, folds were formed only partially before the next folds began to completely form. This is attributed to the fact that the shell was undergoing constrained deformation, due to the lateral support of the filler material, with the ability of fold formation being inhibited due to the presence of the filler material. Furthermore, because the filler hardens non-linearly (that is, its stiffness increases with axial deformation) the lateral support provided by the filler to the buckling cell walls increase (this effect is similar as a beam in a non-linear elastic hardening foundation) as the loading increases. Consequently, the plateau level of the filled model was much higher compared to that of the unfilled model. Of course, during the plateau level, the filler lateral stiffness stays constant. Overall, the predicted response of both the models was in fairly good agreement with the experimental data with the exception of the peak load for the crush simulation of the filled model. A series of images of the deformation response of filled and unfilled models are shown in Figure 4.15. Individual cells in the filled model also showed signs of global deformation and this phenomenon was also observed in the experiment. Note that in the above crush simulation, there was no mechanism to accommodate longitudinal tearing of the honeycomb. This aspect is beyond the scope of the present investigation and is relegated to a future study.

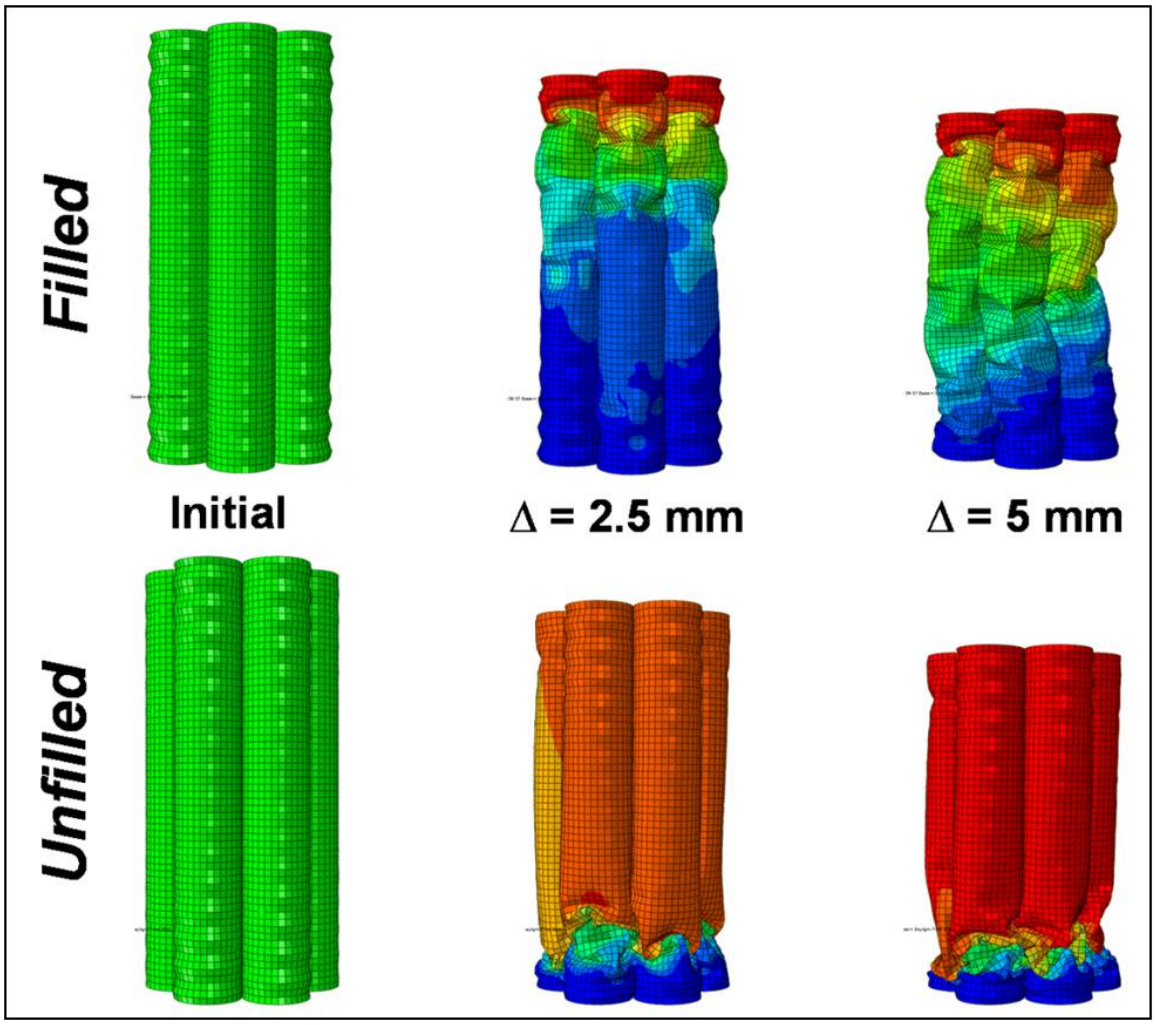

Figure 4.15: Deformation of filled and unfilled 7-cell honeycombs obtained from explicit finite element simulation. The folding in the filled model is more spread out in a random fashion compared to the unfilled model where the failure is localized near an end. Also, the filled model shows cells deforming globally and this behavior is not present in the unfilled specimen. Overall, the deformations seen for filled and unfilled models are in good agreement with the deformation observed from experimental images.

4.4 Effect of filler stiffness on the crush response

In the previous section, we have shown that the presence of the filler material changes the mode of deformation in the honeycomb when compared to the unfilled case. This change in deformation is due to the stabilizing effect of the filler material. This is related to the response of the beam on an elastic foundation. It is seen that an increase in the foundation stiffness has an effect on decreasing the wavelength of the eigenmode of the beam. Now, in our present problem, Keeping the honeycomb base system fixed, let us compare the effect of the stiffness of the filler on the response of the filled structure. This analysis has been performed via finite element simulations similar to that described in the previous study. We have considered 5 curves for the elastomers. Curve B is that of polyurethane that has been described in the earlier experimental study, curve D is PDMS (polydimethysiloxane). The curves A, C and D are created such that the polymer stiffness increases from curves A to D as shown in Figure 4.16. The load-displacement response of composite honeycombs filled with these elastomers is shown in Figure 4.17. We see that with increase in the stiffness of the filler material, the collapse changes from unstable to stable behavior. Moreover, the load at which first collapse occurs shifts to a higher load with increase in the filler stiffness. The contribution of the honeycomb component to the load response is shown in Figure 4.18. Again, it is noticed that the peak load increases and tends to become more stable when the surrounding elastomer stiffness increases. The mode of collapse associated with these cases is shown in Figure 4.19. For curve A that has low stiffness, the mode of collapse is dominated by the diamond shape with larger-wavelength (diffused). Recall that in the extreme limit with no filler, the collapse shape would be dominated by the diamond pattern. Now, with increase in the foundation stiffness the diffused folds tend to be dominated by the concertina (axisymmetric) pattern with decrease in the fold wavelength.

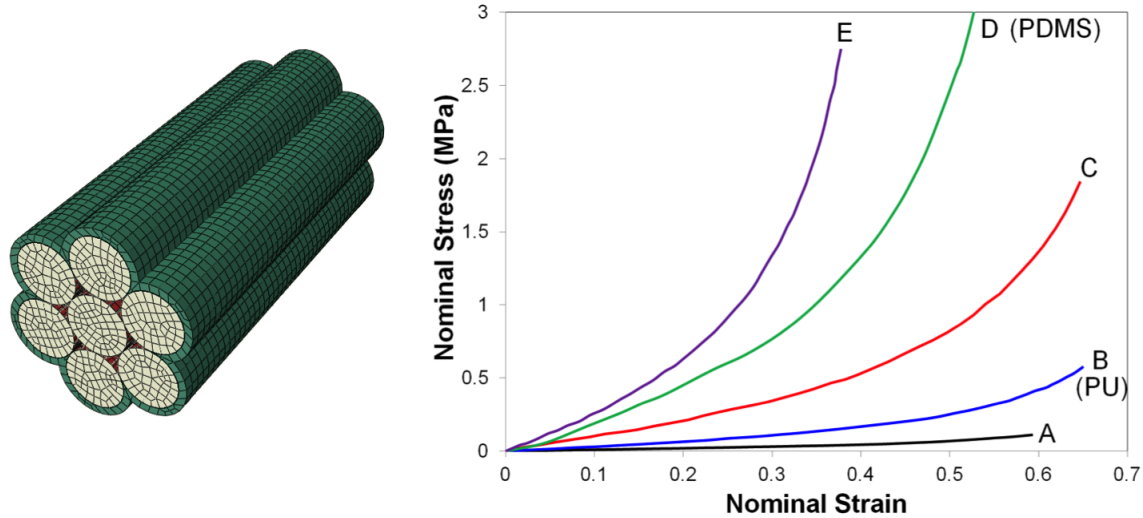

Figure 4.16: Finite element model of the filled honeycomb (left). Nominal stress vs. strain curves of elastomers considered in the study. The curve B corresponds to polyurethane and curve D corresponds to PDMS.

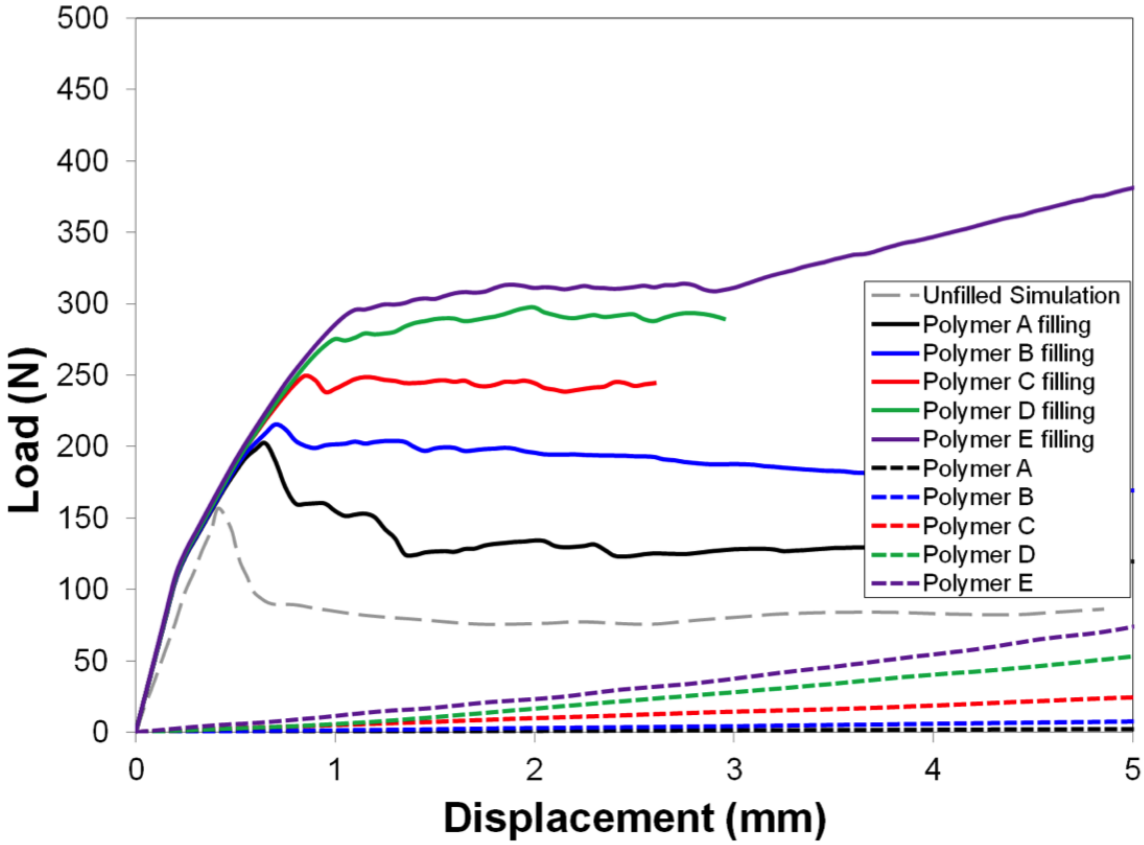

Figure 4.17: Load response of filled honeycomb with varying elastomeric properties and corresponding response of an equal sized elastomer.

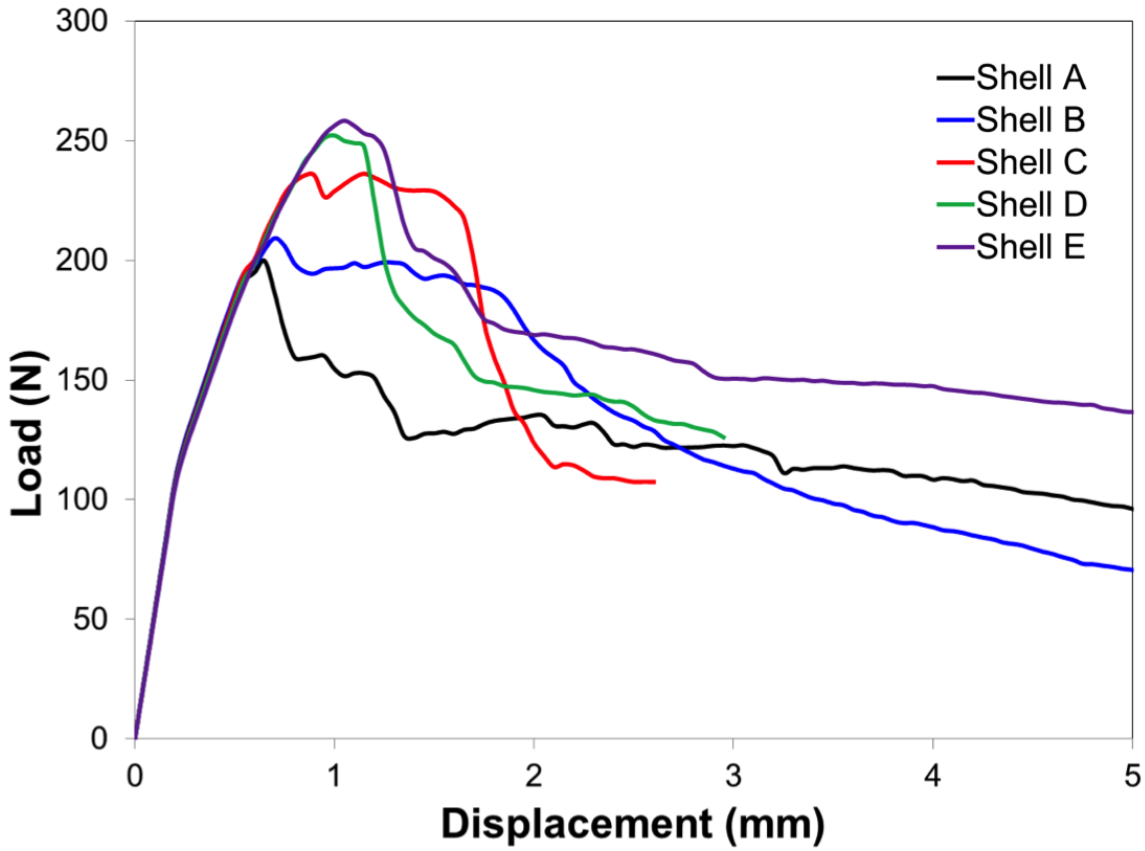

Figure 4.18: Load carried by the honeycomb during the axial crushing of the filled honeycomb for varying filler stiffness

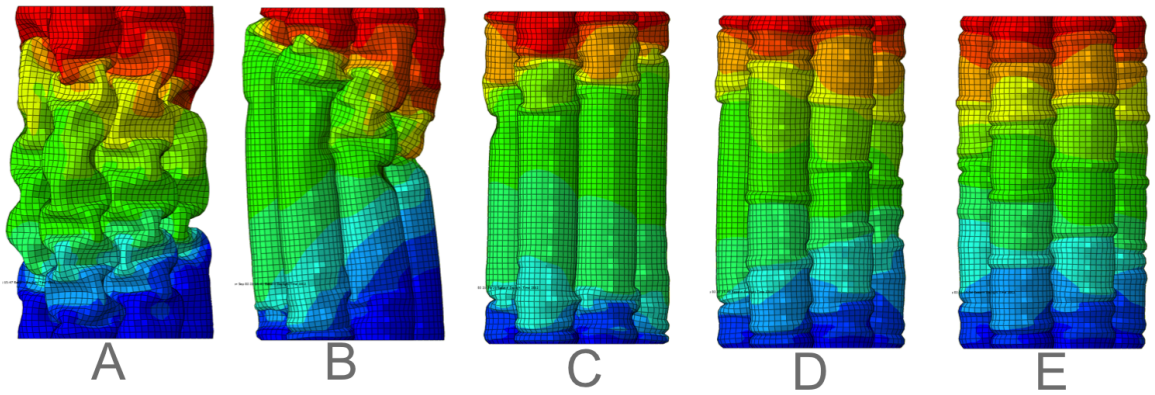

Figure 4.19: The mode of collapse in the honeycomb for the five cases considered.

4.4.1 Summary & Conclusion

In this chapter, we investigated the axial crush response of filled 3-cell, 7-cell and 19-cell specimens through uniaxial quasi-static crush experiments, motivated by prior work reported in Mellquist & Waas (2004). Soft elastomer polyurethane was used as the filler material. Explicit finite element modeling was used to simulate the crush behavior of a representative 7-cell filled honeycomb. The main findings of this work are as follows

1. Beyond the initial failure, the filled honeycombs had greater load carrying capacity compared to the unfilled honeycombs, due to the lateral wall support provided by the filler.

2. Initial failure in filled honeycombs was a stable failure in contrast to unfilled honeycombs, where the catastrophic failure was accompanied by a large and instantaneous drop in load.

3. Initial failure was characterized by fold formation. With increase in the load, the folds appeared at disconnected regions along the length of the individual cells, which is referred to as distributed fold formation. In contrast, folds in the unfilled honeycombs usually propagate from one end to the other via concertina-diamond mode, thus localizing the area of dissipation. These experimental observations were reproduced by the finite element crush simulation, lending credence to the developed model and the modeling strategy for future studies

4. The normalized load carrying capacity of the filled honeycomb was more or less similar for 3-cell, 7-cell and 19-cell specimens, reinforcing a similar result for unfilled honeycombs reported in Mellquist & Waas (2004).

5. Apart from fold formation, other failure modes were observed which contributed to reducing the load carrying capacity of the specimen, such as global buckling and longitudinal tearing. These mechanisms, if suppressed, can lead to even better mechanical performance.

6. The honeycombs having high aspect ratio (such as the 3-cell specimen) were prone to global buckling even under confinement with the soft polyurethane material. This effect was not observed for comparatively low aspect ratio honeycomb specimen (such as the 19-cell specimen).

7. From the parametric study conducted on the filler material, the relative stiffness of the filler material controls the mode of deformation and the wavelength of the diffused folds. Especially, stiff filler material would result in a lower wavelength diffused folding in the cell walls of the honeycomb.

4.5 APPENDIX: Axial crush of filled hexagonal aluminum honeycomb

In this appendix, we report results of another honeycomb-filler combination, namely 7-cell aluminum honeycomb filled with PDMS elastomer. Aluminum honeycombs (alloy 3003) with hexagonal microstructure are used for the static out-of-plane crush response study. The out-of-plane length of the honeycomb is 12.7 mm, the edge length is 4.45 mm and wall thickness is 0.09 mm. Specimens are placed in a cylindrical mould of height 25.4 mm and diameter 22.8 mm and PDMS resin + hardener mix is poured over. Next, the air bubbles are removed using a vacuum chamber. The sample is heated at 100°C for 45 minutes and left to cool. The excess PDMS filler is carefully cut and the top surface is ground using an emery paper. The sample is placed in an INSTRON machine and loaded quasi-statically at a crush rate of 0.033 mm/sec. Data is acquired at the rate of 10 Hz and images are acquired every 5 seconds. Test was also conducted on 7-cell unfilled samples and an equal sized PDMS specimen. The load vs. end-shortening plot of these specimens are shown in Figure 4.20.

With reference to this plot, the unfilled specimen response is nearly linear where axial crushing

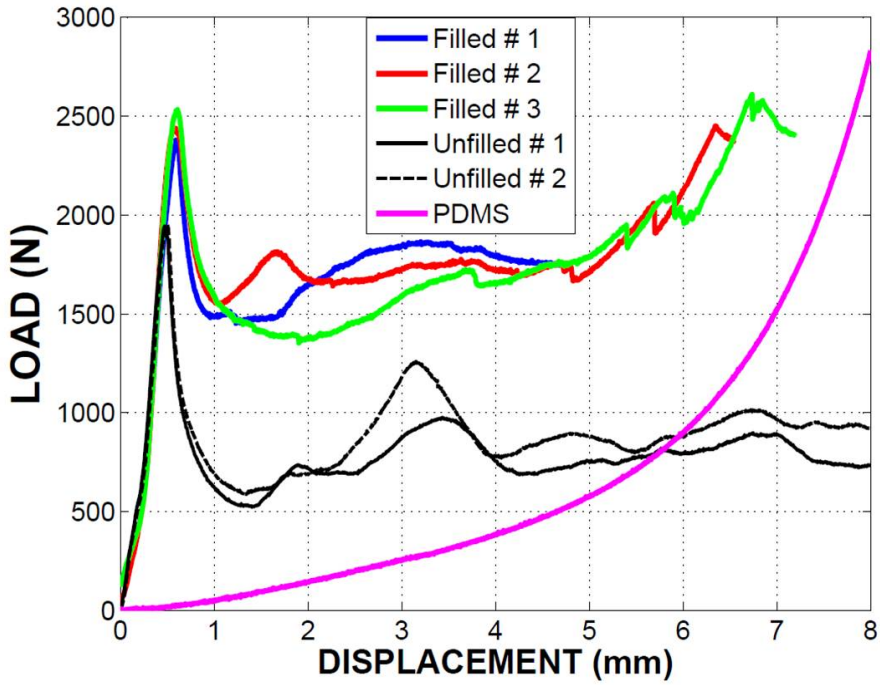

Figure 4.20: Load-deflection plot of 7-cell filled and unfilled hexagonal aluminum honeycomb. The load response plot of PDMS is also shown for comparison.

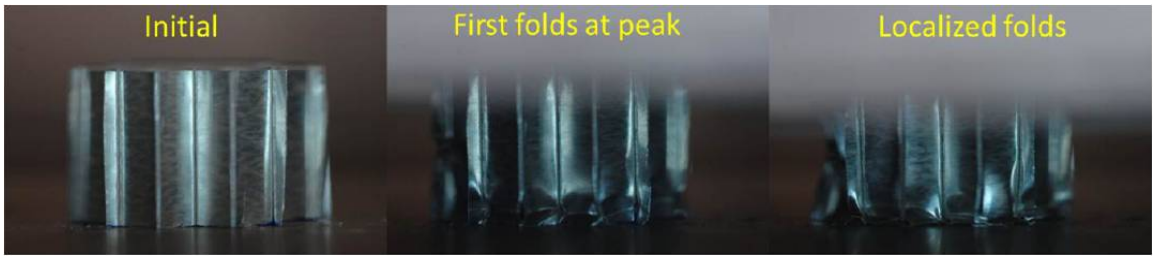

Figure 4.21: Image showing first fold formation at first peak (center) and localized folding (right) at the bottom of the specimen, beyond the peak in the unfilled honeycomb experiment.

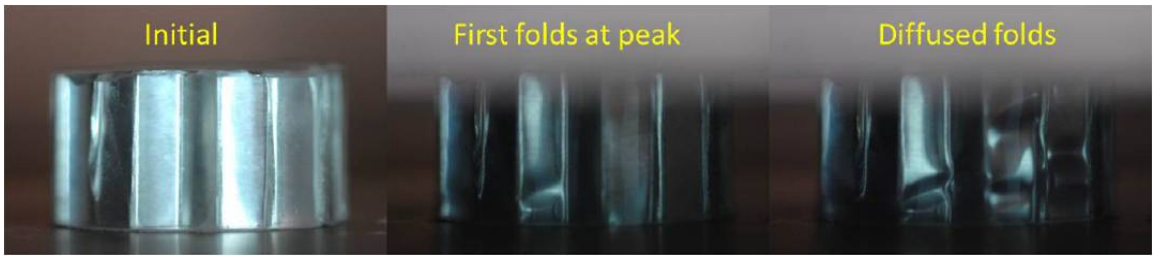

Figure 4.22: Image showing first fold formation at first peak (center) and diffused folding (right) beyond the peak in the filled honeycomb experiment.

takes place with no fold formation. The load rises to a peak load of 1900 N. At the peak, folding is seen at one end of the specimen and the load drops to approximately 550 N. This first collapse is unstable where stiffness becomes negative and a sharp drop in load ($\approx$ 1350 N) is seen over a relatively small crush distance. Thereafter, the load maintains a relatively constant value where new folds are formed. This plateau load is close to 800 N. The folds are localized and progressively form from one end to the other. The deformation sequence of the unfilled specimen is shown in Figure 4.22. In the case of the filled specimen, there is an initial linear region where the load peaks to a value of approximately 2450 N compared to peak value of 1900 N for the unfilled specimen. Up to this point, the crushing in the sample is mainly axial with no visible folds. By comparing with the PDMS response curve in Figure 4.20, the contribution of the PDMS to the total load is marginal and the honeycomb carries majority of the load. Moreover, due to marginal contribution of PDMS here, the slope of the linear region for the unfilled and filled samples is similar. Beyond the peak, the load drops to nearly 1500 N and the first folds appear immediately after the peak. The drop in load in the filled specimen is 950 N compared to load drop of 1350 N in the unfilled specimen. This reduction in load drop immediately after the peak indicates that the filler material has partially stabilized the first failure event. Thereafter, the load is at fairly constant value of 1700 N, again plateau load value higher than its unfilled counterpart. The folds formed are diffused and not localized as seen in the unfilled honeycomb. The deformation sequence of the filled specimen is shown in Figure 4.21. This feature is identical to that in our study with polycarbonate-polyurethane out-of-plane crush experiments, which was reported in the previous sections. Apart from diffused folding, longitudinal tearing was another failure that was observed in the honeycomb specimen.

Synergistic response of the filled honeycomb is shown in Figure 4.23. In the plateau region marked in the figure, the load in the filled specimen is nearly constant (plateau load). Thereafter, the filled response curve rises and takes the shape of the PDMS response at the given end-

shortening value. The end-shortening value (Δ_C) where the unfilled response changes from near constant plateau to a rise, roughly corresponds to the point where the PDMS load value is higher than the plateau load of the unfilled honeycomb specimen[1]. This behavior suggests that as long as the PDMS load level is lower than the plateau load value of unfilled specimen, the corresponding filled specimen exhibits plateau (dissipates the additional external work done by loading). As soon as the PDMS load level is higher than the unfilled plateau, the filled honeycomb starts to store energy. In other words, beyond (Δ_C), the additional external work done in loading is now stored in the structure as elastic strain energy. This feature was also observed in our study with polycarbonate honeycomb filled with polyurethane filler reported in earlier sections of this chapter.

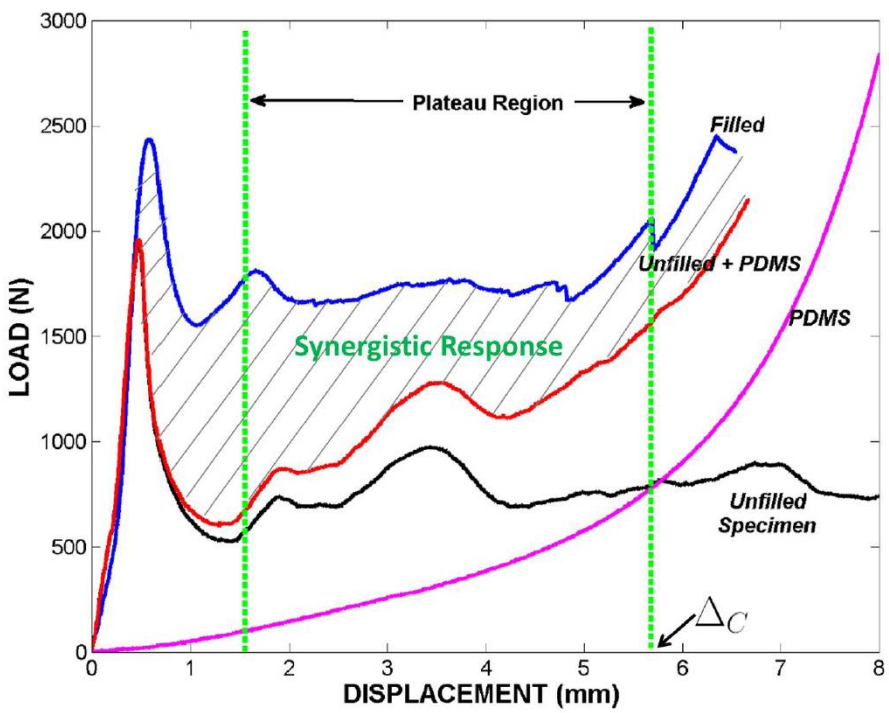

Figure 4.23: Plot showing the synergistic response of the filled honeycomb. The end-shortening value (Δ_C) is at the end of the plateau region, where filled load response rises with further increase in end-shortening.

[1]Recall that in the case of the 3-cell and 7-cell honeycomb filled with polyurethane, similar trend was observed

Chapter 5

Static inplane crush response of circular cell honeycomb filled with elastomer

5.1 Introduction

Honeycombs absorb energy during progressive localized collapse. The onset of collapse is controlled by both material and geometrical instabilities. A representative sketch of a 11×11 size circular cell polycarbonate honeycomb that is used in the present work is shown in Figure 5.1. The progressive localized collapse occurs over a fairly constant state of load called *plateau load*. This plateau occurs over a lengthy region, that begins with the onset of collapse until the progressive collapse has propagated through the entire structure. The mode of collapse under inplane compression is progressive row-wise collapse whereas, the mode of collapse under out-of-plane compression is diamond-concertina buckling – that is closely associated with the traditional axial shell buckling problem. To understand the crashworthiness of circular cell honeycombs, researchers (Papka & Kyriakides 1998, Chung & Waas 1999) have studied the static crush of circular cell polycarbonate honeycombs via experiments and finite element computa-

tions. With increasing understanding of the mechanics, primarily in the static regime, there is a strong interest amongst researchers to provide a continuum level description for such structures. Such equivalent continuum representation of a periodic structure must include higher order effects such as microrotations (Ostoja-Starzewski 2008). For instance, Chung & Waas (2009) have modeled the circular cell honeycomb as a micropolar solid.

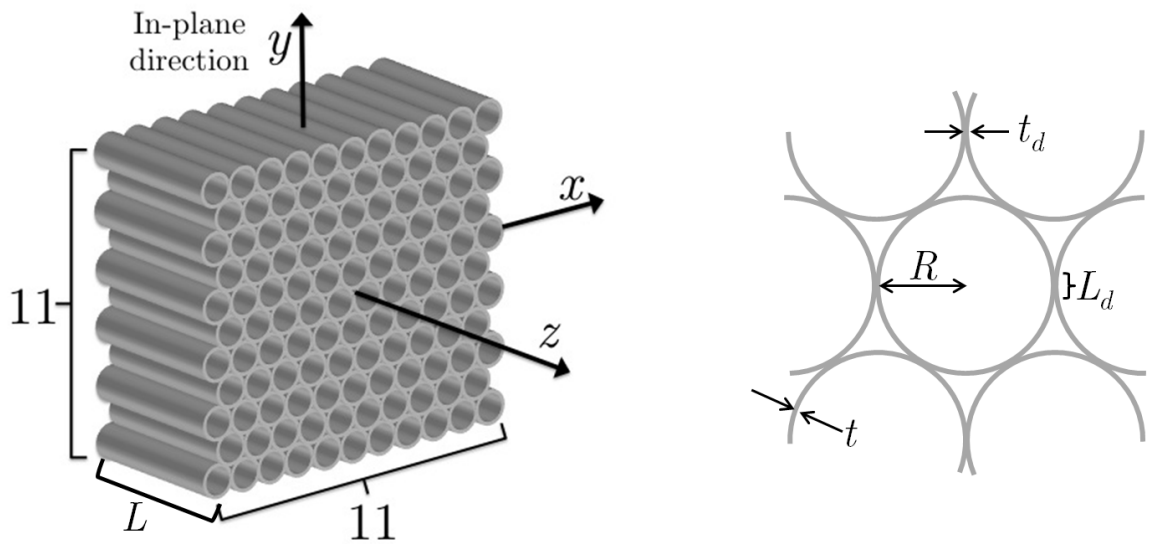

Figure 5.1: Sketch of a 11×11 size circular cell honeycomb (left). Details of the microsection with relevant dimensions, R: cell radius, t: wall thickness, L: cell length, t_d: double-wall thickness, L_d: bond length (right).

The focus of this work is the study of failure mechanisms under uniaxial inplane compression of a “composite" circular cell honeycomb. In the composite honeycomb, the base honeycomb structure is filled with an elastomer and these specimens will be referred to as *filled specimens* to distinguish these from the base structure which we call *unfilled specimens*.

5.2 Material Properties

5.2.1 Polycarbonate properties

The circular cell polycarbonate honeycomb panels were obtained from Plascore Inc., Zealand, MI, USA. We measure the dimensions of the honeycomb cell using an optical study. First, a cluster of seven cells is carefully removed from the honeycomb panel and placed in a cylindrical mold. Next, epoxy resin is poured over and the sample is cured overnight. The top ends of the cured sample are polished with emery papers of increasing grit sizes. Next, the microsection of the cell is studied under an optical microscope. The average dimensions measured are: cell radius (R) 2.03 mm, wall thickness (t) 0.063 mm, double-wall thickness (t_d) 0.0135 mm, wall-to-wall bond length (L_d) 250 mm and out-of-plane length (L) 25.4 mm. Here, the double-wall thickness t_d is the effective thickness of the wall at the contact site of two cells, the contact site having bond length L_d along the cell circumference (Figure 5.1). With the knowledge of the cell dimensions, we perform inplane compression test on individual cells to obtain the elastic modulus of the polycarbonate material (E). This value is obtained by matching the load vs. crush distance curve from this experiment and that in the finite element simulation (FE) in ABAQUS/Standard. The elastic modulus thus obtained is 2600 MPa $\pm$ 200 MPa. Here, the first number corresponds to the mean value and the second value is the standard deviation of 10 samples.

5.2.2 Filler Properties

The filler material used in this study is polydimethylsiloxane (PDMS) elastomer (Dow Corning Sylgard 184). A sample of PDMS is cast in a cylindrical mold of length 25.4 mm and diameter 22.8 mm. The prepared PDMS specimen is subjected to a uniaxial compression test at crush rate of 0.033 mm/sec using an INSTRON machine. The top and bottom loading surfaces are

lubricated to reduce the frictional effects on the compression response. This test enables characterization of the polymer through an appropriate hyperelasticity model, that is subsequently used in finite element simulations described later. The sequence of images showing PDMS deformation along with the load vs. displacement plot is shown in Figure 5.2. To illustrate the vast difference in stiffness of the filler (PDMS) and the honeycomb base material (polycarbonate), the elastic modulus of the PDMS in the small strain regime is about 1.42 MPa in contrast to that of the polycarbonate material having mean elastic modulus of 2600 MPa.

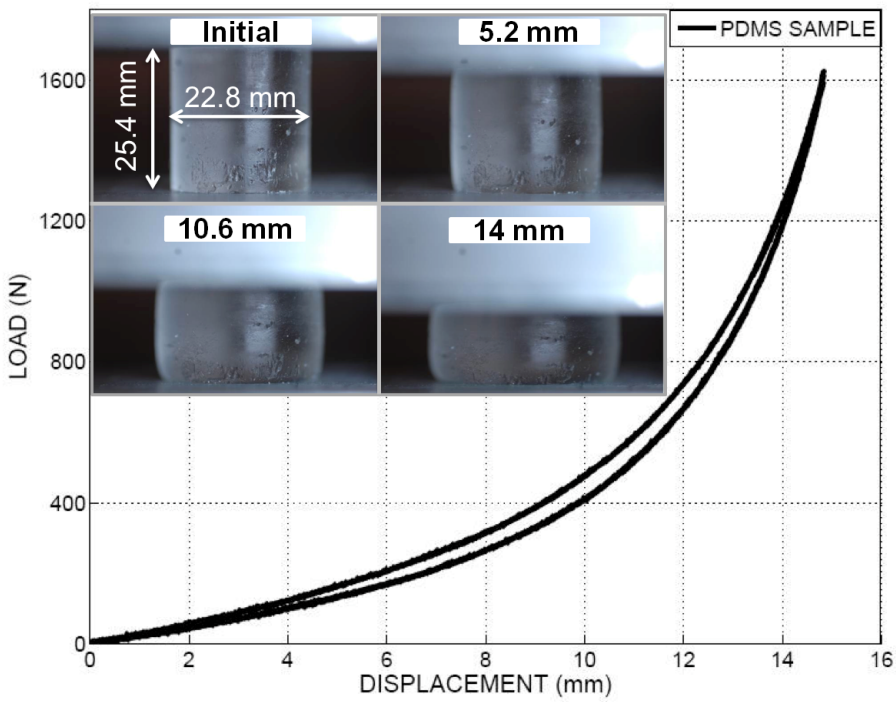

Figure 5.2: Load vs. displacement curve for PDMS cylindrical block along with images during compression.

5.3 Inplane crushing of unfilled honeycomb

We discuss the static crush response of unfilled 11×11 honeycomb specimens. The mode of failure and crush load from this experiment is used for comparison purposes with the filled crush

response to follow. Unfilled honeycombs of size 11×11 are subjected to inplane compression at a loading rate of 0.033 mm/sec in an INSTRON machine. The load vs. displacement plot along with the deformed shape is shown in Figure 5.3. The circular honeycomb cells ovalize during the initial stages of compression. The load response in this region is linear and corresponds to the *prebuckling* response of the structure. We define *ovalization* as the process whereby the initial circular geometry of the cell increasingly tends towards a smooth rectangular shape with increase in crush distance. The ovalization occurs somewhat uniformly in all the cells in the sample.

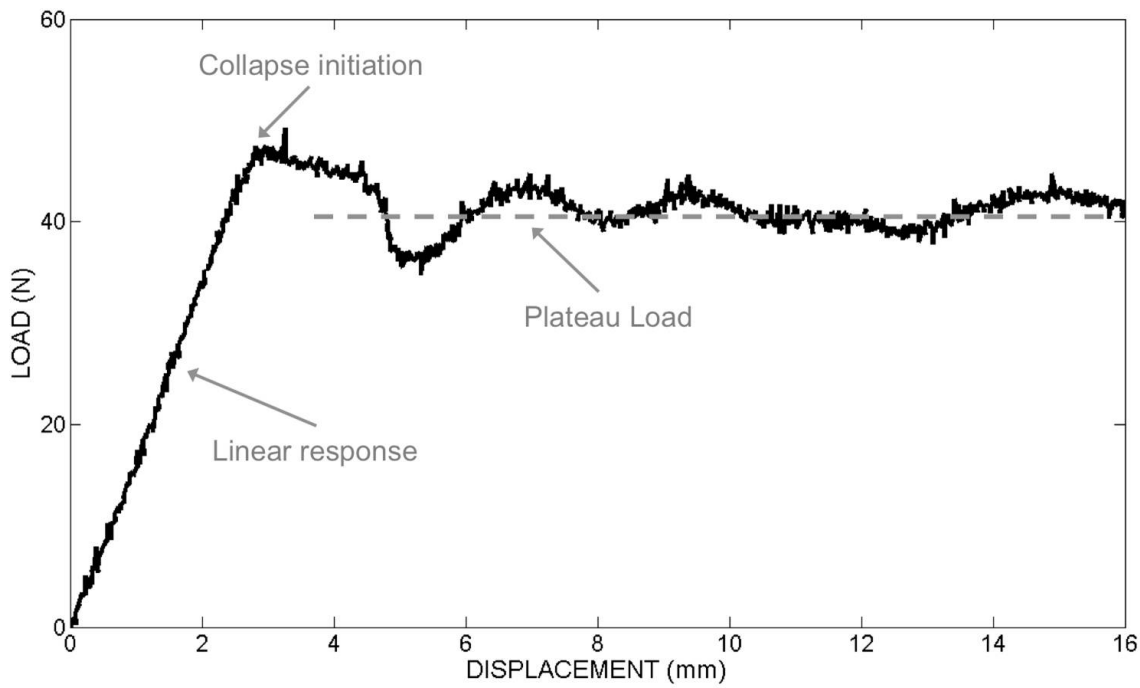

Figure 5.3: Load-displacement plot obtained from the static inplane compression of an 11×11 size unfilled honeycomb specimen.

At a crush distance of 2.8 mm (equivalent to a macroscopic strain value of 0.07), localization in the form of row-collapse initiates across two rows. The first localization zone varies with one sample to another, and is controlled by the severity of unintended geometrical imperfections present in the structure. The load drops slightly until complete collapse of the layer is complete. The load slightly rises and starts to drop once again when the localization spreads to the

adjacent row. Similarly, new rows progressively collapse and this process occurs over a fairly constant load called the *plateau load*. The plateau region occurs in the *postbuckling* regime of the compression response. The row-wise collapse of the unfilled honeycomb is shown in Figure 5.4. The plateau load is found to be approximately 42 N. The plateau load is calculated using integral average of the load vs. displacement response in the plateau regime. The lengthy plateau region enables large amount of energy absorption, thus making these materials attractive for energy absorption. For an in-depth explanation of the mechanics of in-plane crushing of circular cell polycarbonate honeycomb, refer to the works of Papka & Kyriakides (1998) and Chung & Waas (1999).

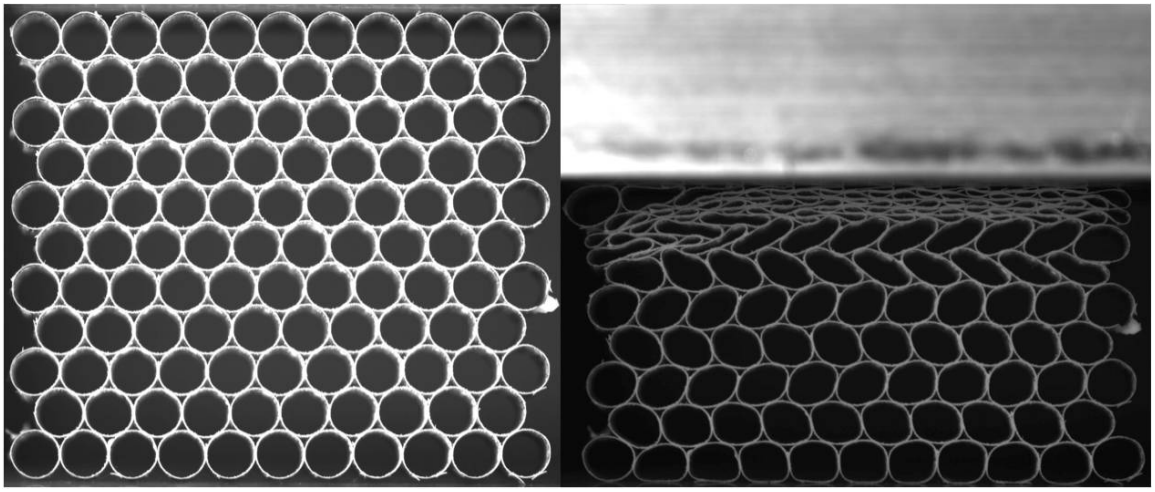

Figure 5.4: Row-wise collapse (right) mode in inplane compression of unfilled honeycomb (left).

5.3.1 Inplane crush response of filled honeycomb

5.3.2 Introduction

Using the unfilled honeycomb as a benchmark, we investigate if filling honeycombs with soft elastomer would increase the load carrying capacity; and also the energy absorption capability. This section describes the inplane compression of polycarbonate honeycomb that is filled with

PDMS elastomer. First, honeycomb specimens of size 11×11 are filled with the PDMS mix and the air bubbles removed in a vacuum chamber. Next, the sample is heated at 100°C for 45 minutes and left to cure for two days at room temperature. Inspection of the cured specimens reveals that no adhesion exists between the PDMS filler and the surrounding polycarbonate cell walls. The weight of the filled 11×11 size specimen is 43.5 g and is approximately 13-fold higher than the weight of the unfilled 11×11 size specimen. The filled specimens are subjected to inplane compression (crush rate of 0.033 mm/sec) using an INSTRON machine. Here, the load is recorded at 10 Hz using a 1000 lbf capacity load cell. The experiments conducted on several samples were consistent in the load response. The load vs. displacement plot obtained from these uniaxial compression experiments is shown in Figure 5.5. Two deformation regimes are identified with regard to Figure 5.5 - the pre-failure and failure regime that are described next.

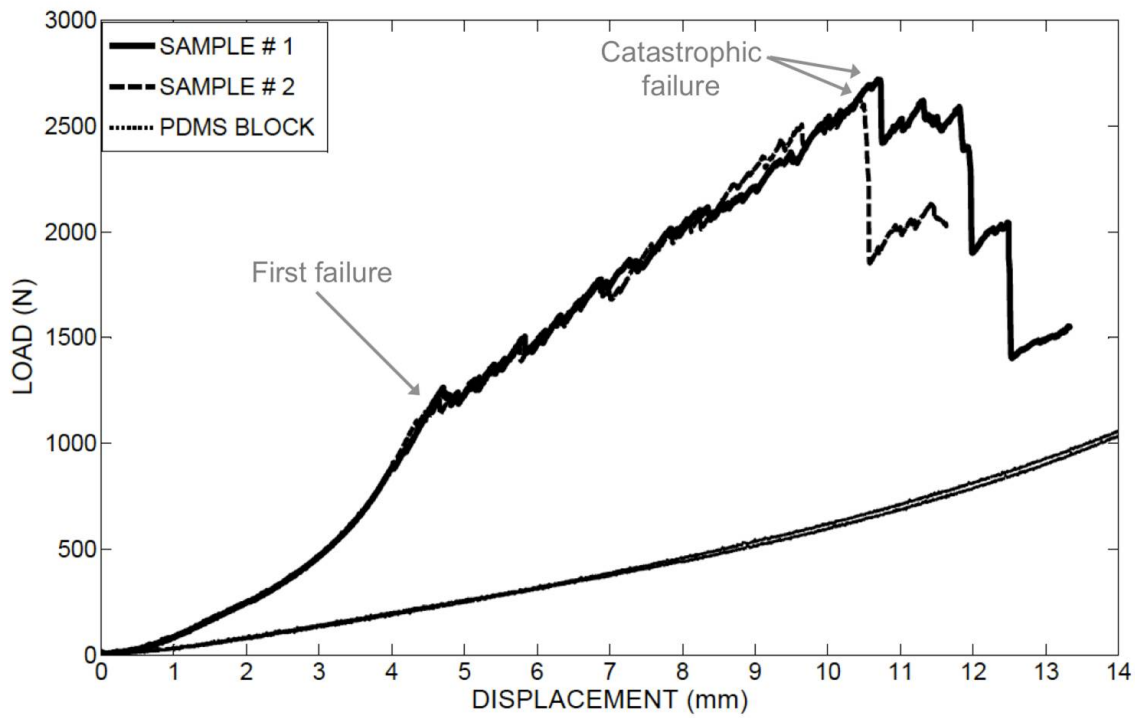

Figure 5.5: Load vs. displacement plot of the compression response of 11×11 size filled honeycomb. Also shown is the load response of a PDMS block of identical size. To make a comparison, the plateau load in the 11×11 size unfilled honeycomb is approximately 42 N.

5.3.3 Pre-failure regime

During the initial stages of loading, cells ovalize and this deformation pattern is fairly homogeneous across all the cells. Note that cell ovalization is similar to that seen in the prebuckling regime of the unfilled specimen. The ovalization takes place up to a crush distance of approximately 4.5 mm, which shall be referred to as the *pre-failure region* (before the onset of failure). In the pre-failure region, the specimen response is non-linearly elastic unlike that observed in the unfilled honeycomb where the response was linear. This observation suggests that the non-linear response of the filler polymer strongly influences the overall non-linear behavior of the filled specimen. From the images, we observe that with increase in crush distance, the PDMS filler bulges outwards along the out-of-plane direction owing to the incompressibility property of the polymer and due to lack of axial constraints on the honeycomb face.

5.3.4 Failure regime

The presence of the filler prevents the row-wise collapse of cells. This resistance to cell wall collapse delays the onset of failure in the filled honeycomb by mechanism different from row-wise collapse that was observed in the unfilled honeycomb. The onset of failure occurs at a crush distance of approximately 4.5 mm with localization near center of the specimen. The first and second localization sites for a specimen are shown in Figure 5.6. Cells near the localization site rotate (Figure 5.6). The behavior of cells in the vicinity of first failure is discussed later using a digital image correlation study. The localization is triggered by longitudinal wall tearing (Mode I crack) near the double wall contact site and is accompanied by an audible click. On few samples, cell wall-to-wall debonding was also observed along with the predominant wall tearing failure. The load vs. displacement plot shows significant reduction in the stiffness. Across various experimental trials, the first localization site varies from sample to sample but is predominantly seen near center rows of the specimen. With increasing crush distance, the

localized cell-to-cell failure and longitudinal tearing spreads to several disconnected regions in the specimen. Each localized failure is characterized by a slight drop in the load and is seen in Figure 5.5, for displacement values of 4.5 mm and higher. During the spread of damage across the specimen, the stiffness is fairly constant. As seen from the images, the fillers do not relax considerably, thereby maintaining the overall positive stiffness in this regime.

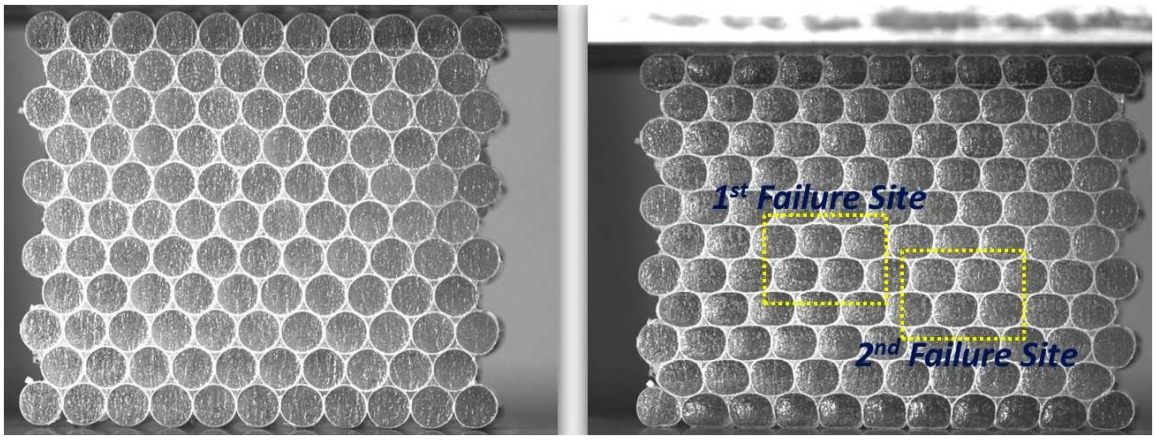

Figure 5.6: Undeformed filled specimen (left). Image prior to first failure showing first and second localization sites (right). Notice the ovalization in the cells (right).

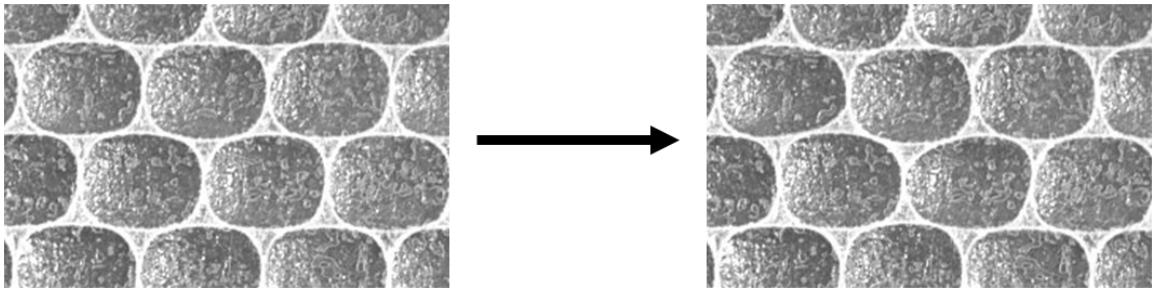

Figure 5.7: Images showing the first localization site prior to localization (left) and at the onset of localization (right).

Thereafter, these localized failure regions spread across the specimen until a weak-plane (oriented at 60° with the horizontal) is formed that is favorable for global failure in shear. The specimen fails catastrophically with prominent failure planes forming an X shape. An image of the failed specimen is shown in Figure 5.8. The catastrophic failure event is accompanied by a sharp load drop and this event occurs at a crush distance of 10.8 mm (macroscopic strain value

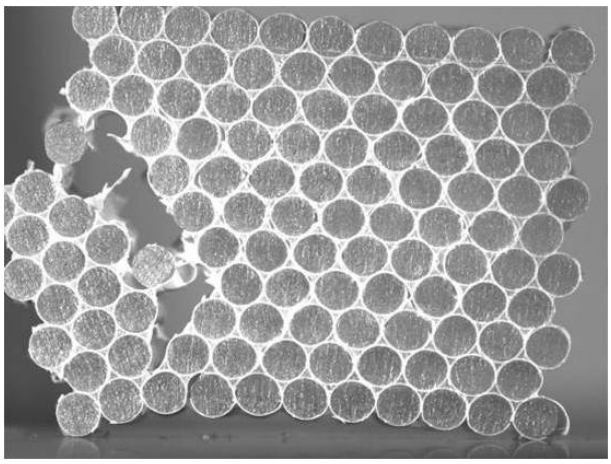

Figure 5.8: Specimen unloaded immediately after catastrophic failure. Notice the global shear-like failure to the left.

of about 0.28). The test is terminated soon after the large drop in load. The individual PDMS fillers relax to their undeformed configuration.

5.3.5 Synergistic response

We now discuss the fundamental differences in energy dissipation mechanisms between the filled and unfilled specimens. In the unfilled specimen, once localization due to row collapse starts, the energy dissipated is independent of crush distance as collapse occurs at somewhat constant load level (Figure 5.3). However, in the filled sample, after the onset of failure, the energy is effectively stored in the filler (stiffness is positive) even though some dissipation occurs during progressive damage in the cells (Figure 5.5). Thus, the rate of energy stored in the filler material is greater than that dissipated in wall fracturing and due to relaxation in the filler material as a consequence of localization. Therefore in the filled specimen, large amounts of strain energy is first stored in two stages (a) from start to first failure (nonlinear stiffness region) and (b) first-failure regime to catastrophic regime (stiffness is constant). A major portion of the stored energy is at once dissipated during catastrophic failure.

Compare the load response of the individual components as a function of the end-crushing

distance up to catastrophic failure. The load carried by the filled specimen is much higher compared to the sum of the loads carried by the unfilled honeycomb specimen and a PDMS block of the same volume as that of the filled specimen. This behavior points towards a synergistic effect in the load carrying capability in the filled honeycomb. The load at onset of failure is 1100 N, roughly 24-fold higher when compared to unfilled first failure load of 41 N. Also, the load at catastrophic failure is approximately 2600 N that is 58-fold higher than plateau load of a similar 11×11 sized unfilled honeycomb. This observation strongly suggests that the confinement of PDMS filler within the individual cells and the inability of the cells to collapse are mechanisms responsible for the attainment of very high load levels in the filled specimen. A table comparing some of the features of the unfilled and filled response is summarized in Figure 5.9.

Initial Stiffness	**N/mm**
Unfilled	16.8 (baseline)
Filled Initial Slope	176.6 (11×)
PDMS Initial Slope	62.7 (4×)

Load	**N**
Unfilled Plateau	41 (baseline)
Filled Honeycomb at First Failure	1100 (27×)
Filled Honeycomb at Global Failure	2600 (63×)

Weight	**grams**
Unfilled Honeycomb	3.4 (baseline)
Filled Honeycomb	43.5 (13×)

Figure 5.9: Tables comparing some average statistics between the unfilled and the filled honeycomb specimens under static inplane loading.

5.4 Digital image correlation study

5.4.1 Introduction

To understand the mechanisms of deformation in the pre-failure and the failure regime in the filled honeycomb, it is necessary to have the knowledge of the strain distribution across the $x-y$ plane of the deforming specimen. We use digital image correlation (DIC) technique to study the strain and displacement fields in the specimen. The images obtained are analyzed using commercially available DIC software called ARAMIS. First, the front face $(x, y, z = 0)$ of a filled honeycomb specimen is coated with a thin layer of white paint. Next, a uniform black speckle pattern is created on the white colored back-ground. The speckles serve as markers to track relative displacements on the flat surface of solids undergoing deformation. The displacement information is used by the software to generate strain maps. Note that the strain maps obtained from such an analysis is only a reflection of the strains that are present at the planar surface of the specimen. The nonlinear and large deformation response of the elastomeric filler suggests that in general, the stress distribution at inner sections are expected to be higher than those at the free boundaries located at $(x, y, z = 0)$ and $(x, y, z = L)$.

The speckled specimen is loaded quasi-statically in compression using an INSTRON machine at crush velocity of 0.033 mm/sec. Images are taken at the rate of 1 frame per second. Test data (load and crush distance information) was acquired at the rate of 10 Hz. Owing to large amounts of inplane deformation, there exists de-correlation that deters a unified DIC analysis of the entire deformation sequence, that is, from the initial undeformed reference state all the way up to the first failure event. Therefore, the DIC analysis is conducted in two stages, *Stage I* and *Stage II* that are described below.

5.4.2 Stage I: Initial up to pre-failure regime

The reference configuration for this stage is the undeformed specimen. The end-shortening value at the end of this stage is 2 mm (macroscopic strain value of 0.05). As seen earlier, the behavior of the honeycomb is largely that of cell ovalization. The deformation field Δ_x along the x-direction is shown in Figure 5.10. Here, regions located near the center (along the y-direction), the Δ_x value is close to zero. However, for regions from the center of the specimen to the outer edges, this value gets larger. The contours of Δ_x bow inward due to frictional constraints along the x-direction at the top and bottom edges and free surface at the left and right sides. The normal strain field (ϵ_x) along the x-direction is shown in Figure 5.11. Within a cell, the strain field is non-uniform, with strain concentration being dominant near the center of the cell. The nature of strains in the center of the cells is tensile, whereas that at the cell-cell contact site is compressive. This pattern is more or less uniform across the face of the specimen in all of the cells. The strain values near the center of the specimen are relatively higher than those at the edges; this is due to higher degree of lateral constraint within the center of the cells. The normal strain (ϵ_y) field along the y-direction (the loading direction) is provided in Figure 5.12. The strain map shows strain concentration near the center of the cells; and once again, this pattern is more or less similar across the specimen. However, the strains are purely compressive. In summary, the observations from ϵ_x and ϵ_y strain maps point to a biaxial state of compression provided by the cell to the filler material, that is, the filler is undergoing constrained deformation and hence, is a chief mechanism controlling the synergistic load response in the filled specimen. We next examine the shear strain (ϵ_{xy}) map in the pre-failure regime as provided in Figure 5.13. The shear strain field is not pronounced during the initial stages of compression, but increases with increase in ovalization of the cells. Unlike strain concentrations seen in ϵ_x and ϵ_y strain maps, diagonal bands develop at 60° with horizontal and passing through the points where two cells are in contact. This band formation is a consequence of the circular cells changing towards an oval geometry. One can also observe some pockets of high shear strains

at the corners of the strain map which is an edge effect owing to rotations of corner cells at the loading/reaction platens.

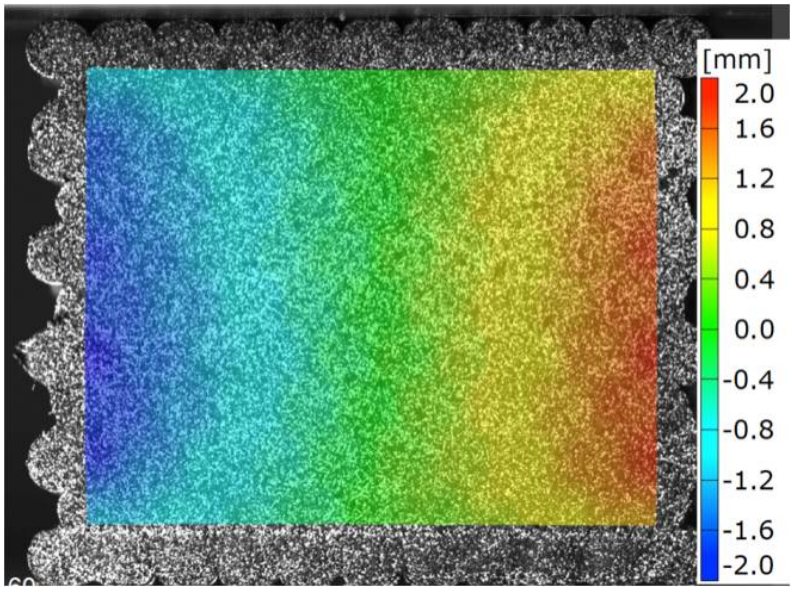

Figure 5.10: Displacement field along the x-direction.

5.4.3 Stage II: In the vicinity of first failure

Next, the DIC analysis was carried out in the vicinity of first failure. The reference state for shear strain (ϵ_{xy}) map calculation is 8 frames before failure. Note that the specimen is loaded through a crush distance of 0.033 mm between two frames. The shear strain field at the onset of failure is shown in Figure 5.14. The sense of rotation is shown to the bottom-left in Figure 5.14. Adjacent rows located to the left and right sides of the failure site have more or less similar magnitude of shear strains. The cells in these two rows tend to move sideways towards the free edge of the specimen, thereby relieving the compressive stresses in the sample. The localization also alters the shear strain field across the entire specimen as well. At the first failure site, de-correlation is noticed due to large displacements and rotations. We have not looked at subsequent localized failure events owing to cracking of the paint surface. Further study is necessary to overcome this issue.

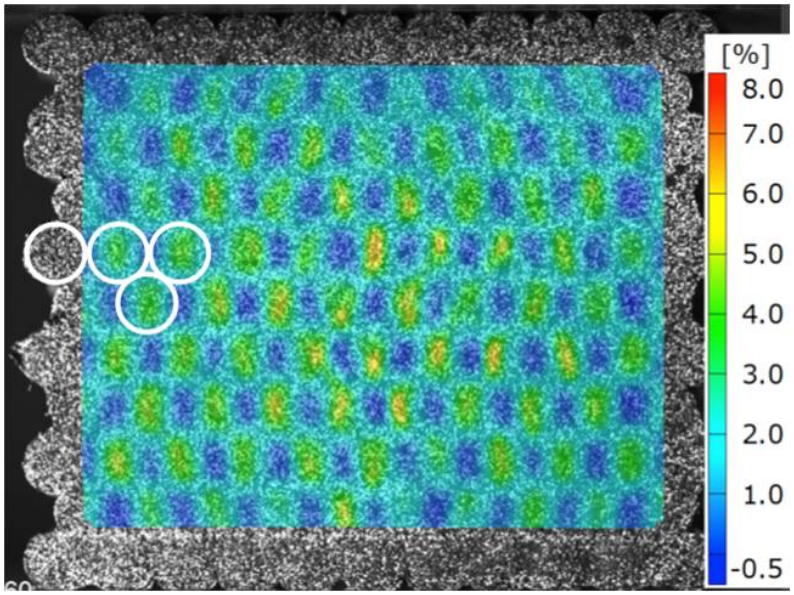

Figure 5.11: Normal strain field along the x-direction.

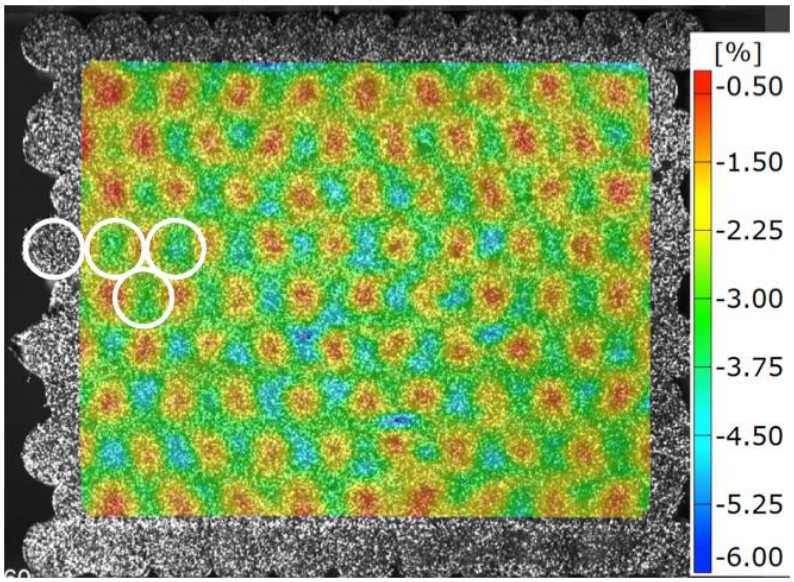

Figure 5.12: Normal strain field along the y-direction.

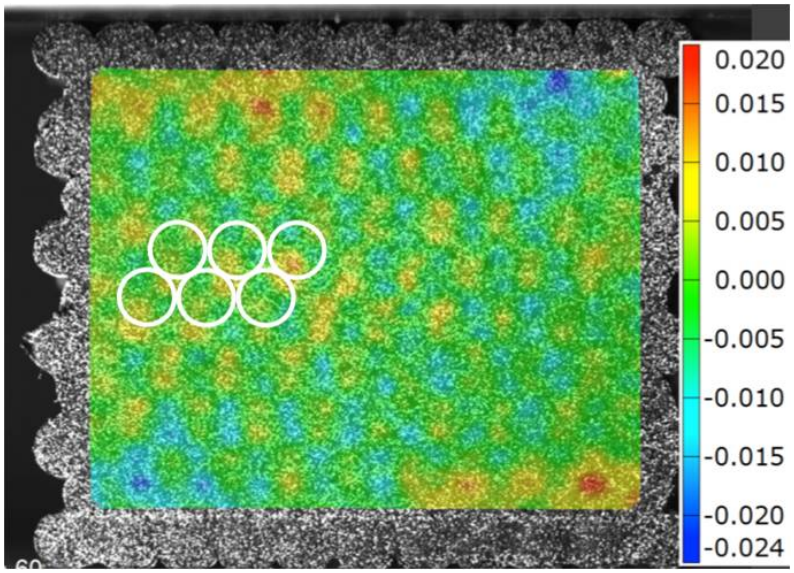

Figure 5.13: Shear strain field showing diagonal band formation.

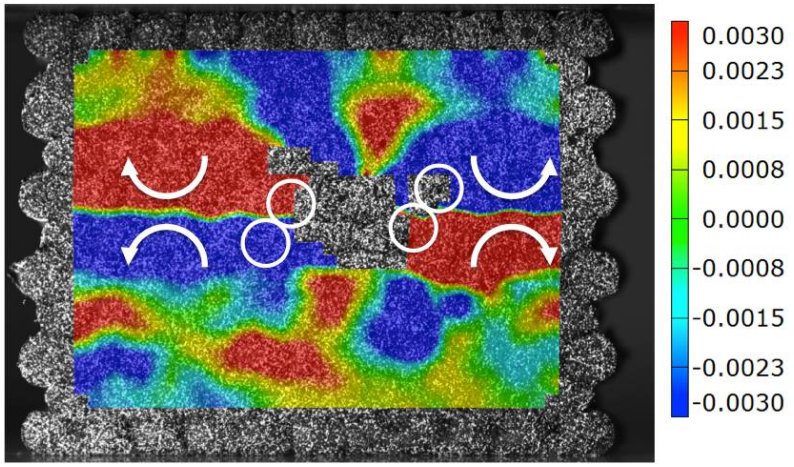

Figure 5.14: Shear strain field at first failure. The arrows show sense of rotation of two adjacent rows near the failure site.

5.5 Finite element simulation of the experiment

5.5.1 Model Description

The inplane crush of filled honeycomb is simulated using commercially available finite element (FE) software ABAQUS®. The finite element model was created using the measured dimensions of the honeycomb microsection. The honeycomb cells are modeled using four-node linear S4R shell elements. The circumference of the cell is discretized with 30 elements and the axial direction is discretized with 6 elements. The nonlinear behavior of the composite honeycomb that we had observed from the experiments requires that the entire specimen be modeled in this numerical study. The filler is modeled using a mixture of eight node C3D8R and six node C3D6R solid elements. Since compression of the specimens in the experiment occurs via steel plates, at the top and at the bottom, the plates are modeled in the FE model via solid C3D8R elements with standard properties of steel. The triangular regions between any three cells are modeled with C3D8R elements. The FE model is shown in Figure 5.15.

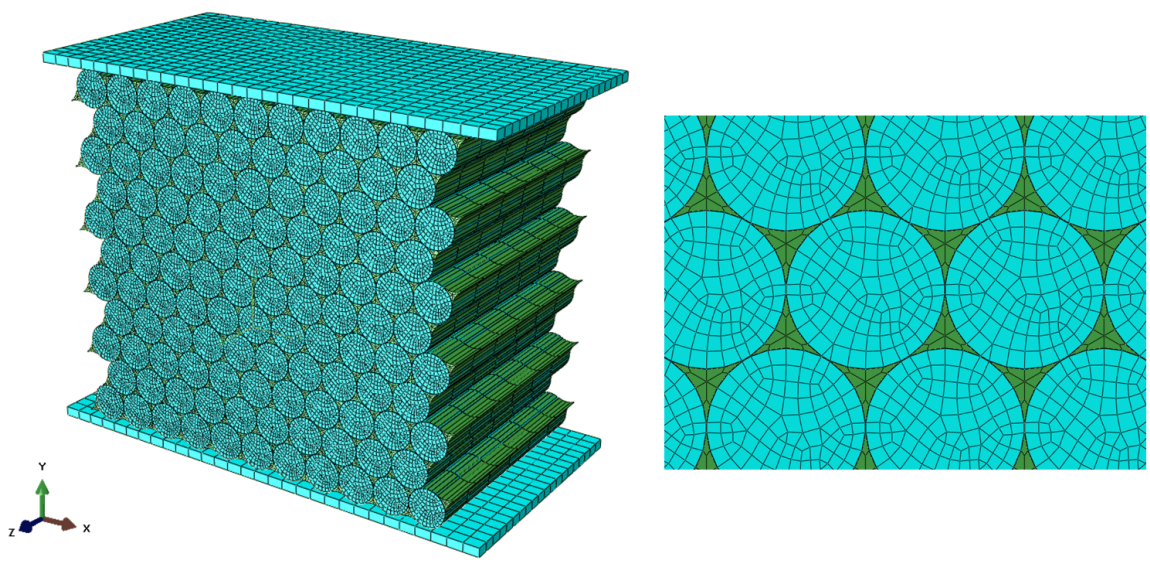

Figure 5.15: Finite element model of the filled honeycomb specimen is shown along with the top loading plate and bottom plate (left). The portion of the front view (right)

The polycarbonate material is modeled with plasticity (`*PLASTIC` card with Young's modulus taken as measured value of 2600 MPa. The plastic portion of the polycarbonate stress-strain curve in the static regime has been taken from Figure 15 from the paper by Mulliken & Boyce (2006). For the PDMS elastomer, the uniaxial compression test data (nominal stress-strain curve) from the experiment is used as input using the Marlow model option in ABAQUS. As mentioned in earlier sections, the PDMS filler does not stick to the cell walls in the filled specimens. Therefore, the contact between the outer curved surface of the in-filled filler material and the inner surface of the honeycomb was assumed to be resisted only by friction. Hence, general contact algorithm was used with (a) "`HARD`" contact to avoid penetration of surfaces during normal contact, and (b) tangential frictional contact with coefficient of friction $\mu = 0.3$. Similarly, since in the experiment, the bottom and top faces of the honeycomb are not restrained along the x-direction, the contact between the honeycomb and top/bottom loading plates are also modeled using (a) "`HARD`" normal contact and (b) tangential contact with assumed coefficient of friction $\mu = 0.3$.

The filler material property is incorporated using Marlow's model option in ABAQUS through the `*HYPERELASTIC` card. The Marlow model is based on the first invariant and is used when limited type test data are available, for instance uniaxial compression data in the present case. Alternatively, the hyperelastic behavior can be modeled using the common Arruda-Boyce 8-chain model Arruda & Boyce, 1993) by matching the model parameters to fit the uniaxial compression experimental response. Assuming incompressibility, the standard parameters for the PDMS elastomer are: (a) Initial shear modulus μ_0 = 0.474 MPa (b) Locking stretch λ_m = 1.27.

The crush simulation is conducted using ABAQUS/Explicit. A crush velocity of 10 mm/s is applied to the top plate. The bottom plate is constrained in rotation and translation and the top and bottom nodes, near the plates are constrained in the x-direction. We use the dynamic explicit solver to simulate the static experimental problem because explicit simulation is compu-

tationally more efficient than using static implicit solver due to the numerous surface-to-surface contact definitions involved between the polymer and shell surfaces.

5.5.2 Application of the Smeared Crack Approach

The smeared crack approach (SCA) is used in the finite element model to simulate fracturing of the cell walls. The SCA was first formulated by Bažant & Oh (1983) as the crack band model and later modified by Rots et al. (1985). The SCA code used for this study follows from the work of Heinrich & Waas (2012), who studied the progressive damage and fracture in laminated composites and extended the Rots model to include non-isotropic fracture. First, the code is specialized for isotropic material behavior under plane stress conditions. Secondly, plasticity (using $J2$ deformation theory) prior to softening response is incorporated as shown in Figure 5.16. These modifications are carried out to take into account plasticity of polycarbonate material; and due to the nature of planar state of stress in the cell walls that are modeled as S4R shell elements in the simulations to follow. The SCA is advantageous over other fracture models in that the crack site/path need not be known *a priori*. This method guarantees mesh objectivity after the onset of failure. Mesh objectivity is ensured due to the post failure region being governed by traction-separation laws that include a *characteristic length scale*. The SCA is incorporated in ABAQUS/Explicit solver through the user sub-routine VUMAT. The important parameters in the SCA are: σ_{cr}, the critical stress to initiate tearing; and G_{IC}, the Mode I fracture toughness, incorporated through an exponential softening curve. Here, σ_{cr} controls the first failure point whereas G_{IC} influences the behavior after the onset of failure (that is, the ease at which crack can form and amount of energy dissipated locally in the softening material).

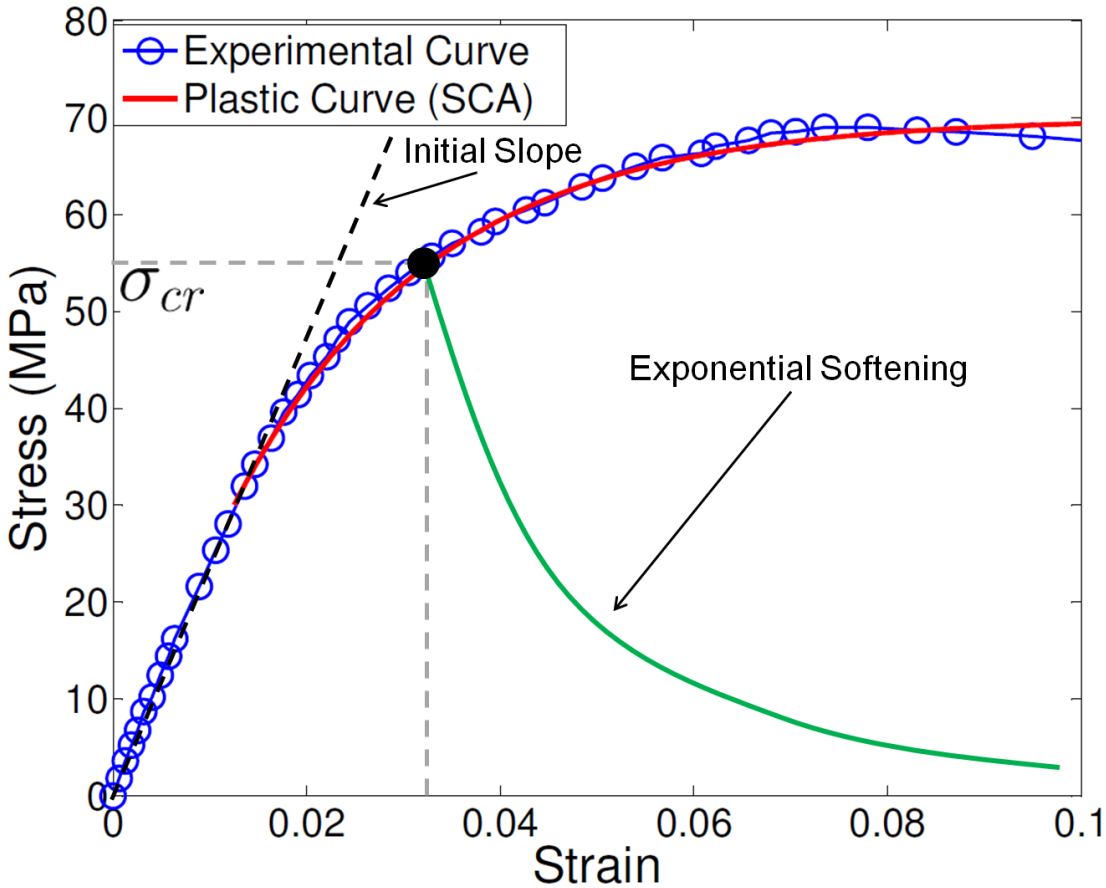

Figure 5.16: Stress strain curve for polycarbonate (Ref: Mulliken & Boyce, 2006) shown against exponential curve fit for the plastic part to be used in SCA model. Also shown is the critical stress value σ_{cr} = 55 MPa, and exponential softening curve that is a function of Mode I fracture toughness G_{IC}.

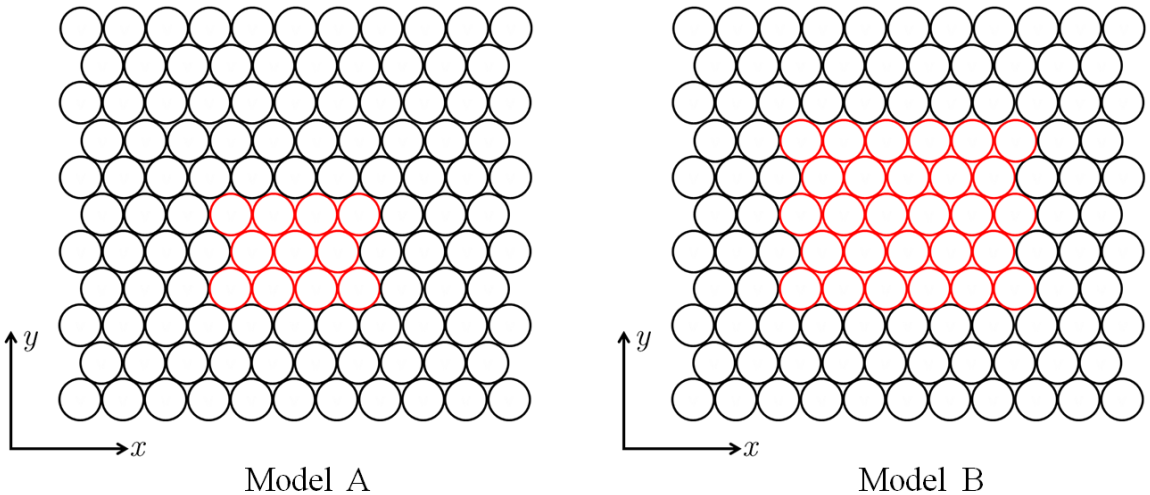

Figure 5.17: Schematic showing 11×11 honeycomb model with crack band (shown in red) being applied in Model A and Model B.

5.5.3 Simulation Results

Recall that in the experiment, the onset of localization was observed near the center of the specimen. Hence, two types of simulations were performed with: (1) *Model A*, with smeared crack band being applied over 11 cells around the center (2) *Model B*, with smeared crack band being applied over 28 cells around the center. A schematic showing the crack bands in the honeycomb in Model A and Model B is shown in Figure 5.17. For the cells with no crack band, the regular polycarbonate stress strain curve was applied.

The load vs. displacement plot is shown in Figure 5.18. For the pre-failure region, the load response from both the models compare well with the experimental curve as seen in Figure 5.5. In the pre-failure region, the cells gradually ovalize and the load response is non-linearly elastic. Strain concentration is seen around the center of the filled cells. To enable qualitative comparison with the DIC analysis, the normal strains distribution along the x and y directions is shown in Figure 5.19 and Figure 5.20. From these strain maps, observe the biaxial state of compression of the filler material in each of the cells. This behavior is consistent with the strain maps obtained from the DIC analysis that has been reported in the previous section. The stress

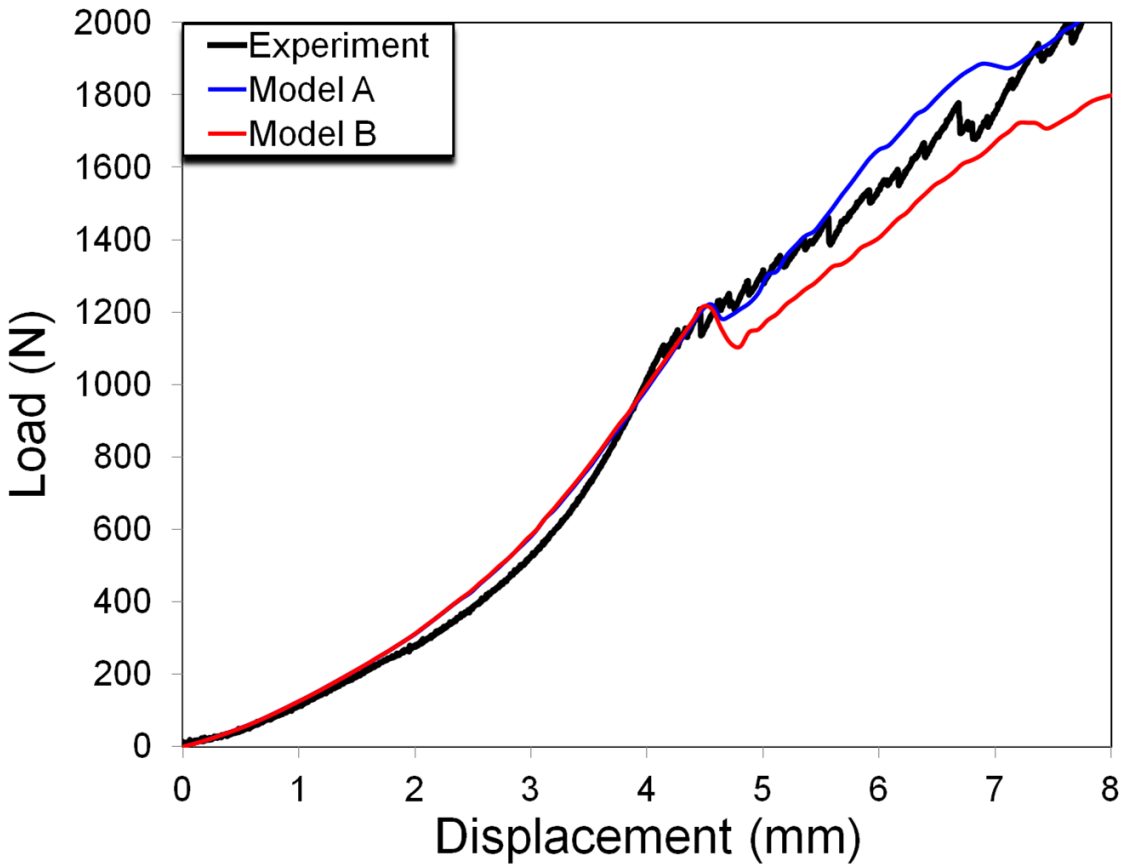

Figure 5.18: Load vs. displacement curve of the simulations and the experiment. Simulations for Model A is shown in red, whereas that for Model B is shown in blue.

distribution along the x and y directions for the filler located near the center of the model is shown in Figure 5.21. The stresses vary along the length and is lowest at the free ends. The compressive stresses are dominant even along the direction perpendicular to loading direction, i.e. along x-direction. This “constrained deformation state" is responsible for the attainment of high levels of load in the model.

In the pre-failure region, the cells around the center of the model experience higher stresses compared to those away from the center; hence, the localization occurs near the center of the specimen due to wall cracking of the cells around this region. The critical stress (σ_{cr}) value for the tearing failure to be initiated was found to be approximately 55 MPa. The value of fracture toughness G_{IC} is taken as 2 N/mm. In the case of Model B, the localization phenomenon is showed in Figure 5.22 and observe the similarities with the onset of localization seen in the experiment (Figure 5.7). These features are similar for both models considered in this study. The strains in the cell walls are shown in Figure 5.23. This observation confirms that the tearing of the cell walls triggers localization in the specimen.

The simulations have been able to capture many important features seen in the experiment such as localization at first failure due to wall tearing and load response especially until the onset of failure. Therefore, the SCA approach is a promising tool that could be used to model wall cracking in the filled honeycombs. However, some differences do exist, especially with regard to the simulation response at the onset of localization. Recall that in the static experiment, there is no load drop during the onset of failure and the localization is restricted to smaller regions around the center of the specimen. Thereafter, in the experiment the localized failure is seen to spread to other regions in the model with increase in crushing. This progression of failure occurs at almost constant value of stiffness. In contrast, in the simulations performed, the load momentarily drops at the onset of localization. The drop is more for Model B where damage

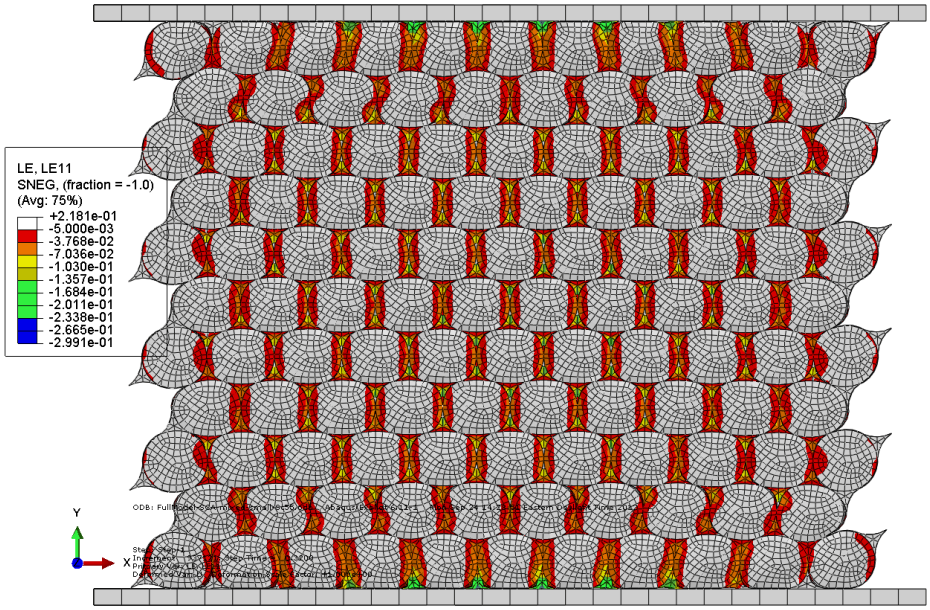

Figure 5.19: Compressive normal strain (ϵ_x) map along the direction perpendicular to the direction of loading. The nature of strains along the center of the cells in the filler is tensile.

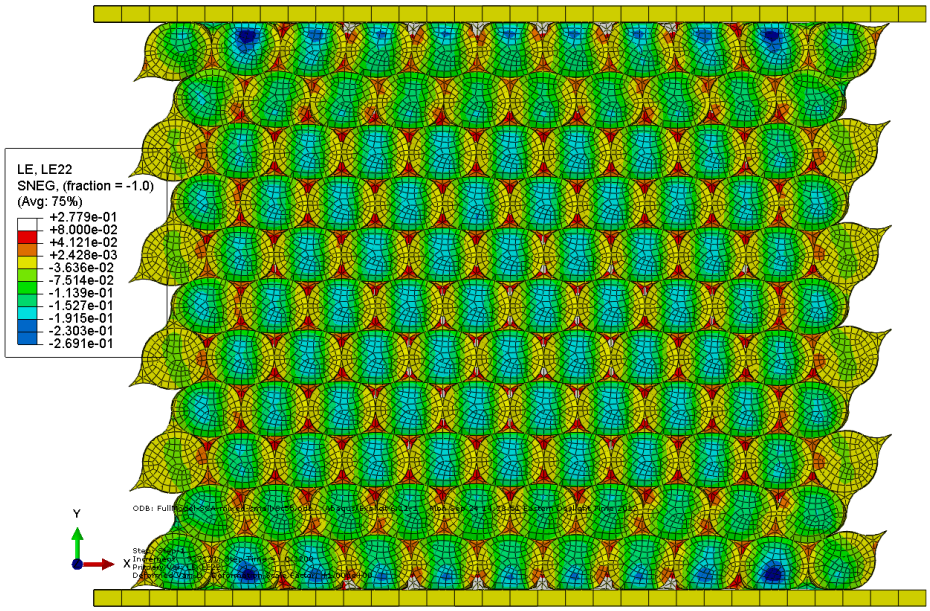

Figure 5.20: Normal strain (ϵ_y) map along the direction of loading.

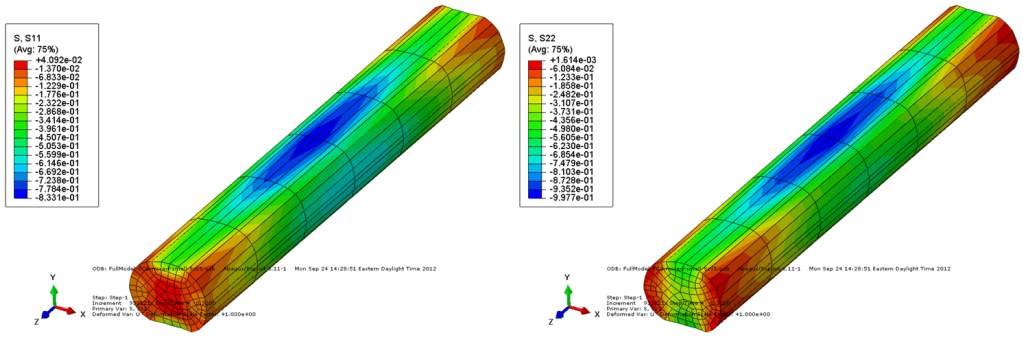

Figure 5.21: Normal stress distributions S_{11} (left) and S_{22} (right) along the x and y directions respectively, for the filler located at the center of the model. Units are in MPa.

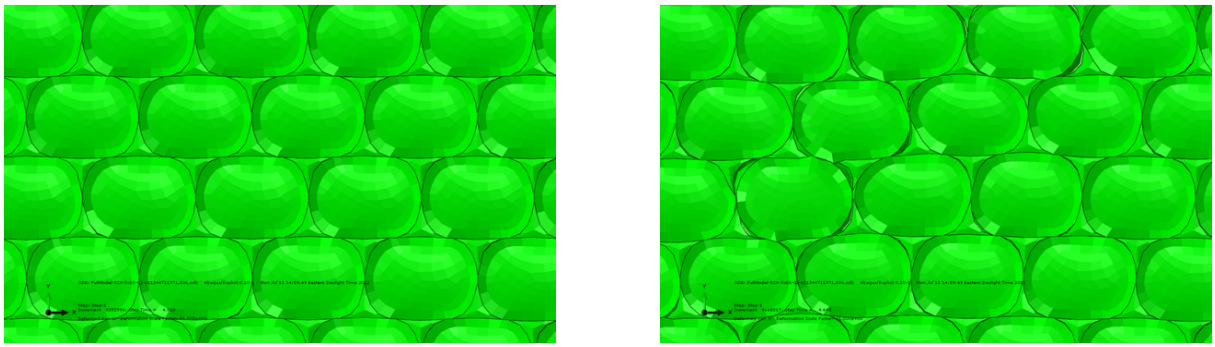

Figure 5.22: Image showing events (a) prior to localization (left), (b) onset of localization (right)

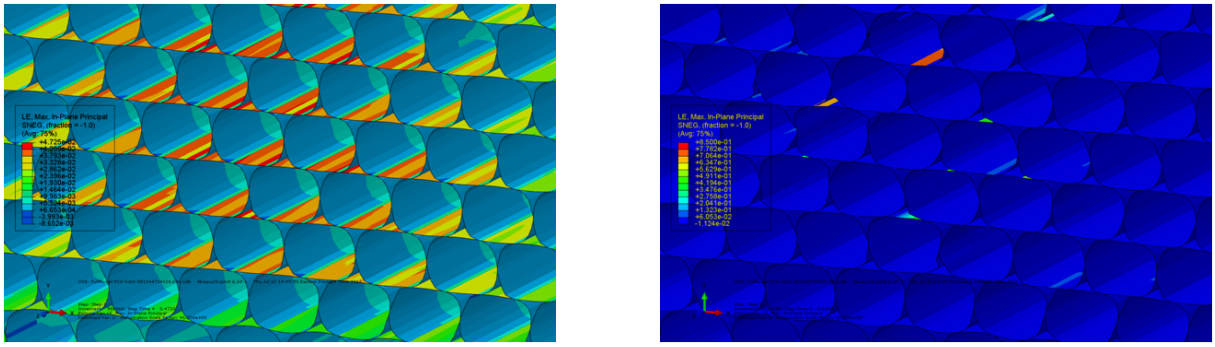

Figure 5.23: Image showing strains in the honeycomb walls (a) prior to localization (left), (b) onset of localization (right)

is seen to spread to a much larger region compared to Model A. Moreover, the post failure stiffness in the experiment lies between that of Model A and Model B. Therefore, for Model B, the larger drop in load at first failure and subsequent reduction in stiffness is attributed to the dynamic nature of the simulation. When tearing is initiated near the center of the model, the energy released due to the artificial release of kinetic energy (note that, the kinetic energy is not suppressed totally in a mass-scaled explicit analysis that aims to simulate a static test) causes surrounding regions to be loaded in excess of the critical stress for tearing. These over-stressed regions initiate premature tears, triggering failure at many points away from the center. This numerical effect can be avoided by applying the crack band scheme selectively to a smaller sized region in the model, effectively compensating for the artificial overstress condition.

5.6 Conclusion

In this work, we investigated the quasi-static crush response of a composite circular cell honeycomb. PDMS was used as the filler material in this study. Two important deformation regimes are distinguished in this study (a) the pre-failure regime (b) failure regime. In the pre-failure regime, the specimen exhibited nonlinear response that was controlled by the filler phase of the composite honeycomb. Moreover, synergistic effect was observed in the load response which was explained by digital image correlation (DIC) analysis and finite element simulations. The synergistic effect arises out of highly constrained biaxial state of stress in the filler material. Unlike traditional honeycombs where buckling of the cell was is a primary mechanism of energy dissipation, the mechanism of energy dissipation in these honeycombs was due to Mode I fracture of the cell walls. The localized fracturing of the cell walls triggered localization in the specimen. Fracturing triggering localization in the failure regime was confirmed in the finite element (FE) simulation of the experiment. Here, a modified Smeared Crack Approach (SCA) was chosen to simulate cracking of the cell walls. SCA is advantageous in that the crack

path need not be prescribed at the start of the FE simulation. The load response between the experiment were in good agreement in the pre-failure regime.

Chapter 6

Summary & Future Work

The work described in the previous chapters concerns with the understanding of failure mechanisms of circular cell polycarbonate honeycombs under uniaxial compression along the in-plane and out-of-plane directions.

A major portion of this study was devoted towards the understanding of the mechanisms of collapse/crushing under static uniaxial compression, when these honeycombs are filled with soft elastomers. Second aspect was to check if filling honeycombs with soft elastomers is advantageous with respect to energy absorption, compared to their unfilled counterparts. From the static experiments and finite element simulations conducted, we report the presence "synergistic" effects in the uniaxial compression of filled honeycombs. Here, the word "synergistic" response implies that the load response (or energy absorption capability) of the filled specimen is greater than the individual responses of the honeycomb base material and the filler material. In particular, in the out-of-plane crushing, the synergistic effects are a consequence of altering the mode of collapse in the cell walls due to the hardening response of the surrounding elastomer; i.e. the mode of collapse has changed from progressive concertina-diamond to diffused folding. Another benefit of filling is that the first failure response is stabilized in contrast to unfilled honeycomb where a drastic reduction in load is seen with the onset of folding. For the

in-plane filled response, the polymer residing in each of the cells prevent the cells from collapsing. Consequently, synergistic effects leading to attainment of high loads are observed due to the biaxial state of confinement in the polymers within each of the cells during deformation.

Unlike the unfilled honeycomb response, where concertina-diamond folding of the walls (under axial crushing) or collapse of rows (under in-plane crushing) were the crush mechanisms, the crushing of filled honeycomb shows an additional failure mechanism - *wall tearing* (Mode I crack). The wall tearing plays important role in energy dissipation, especially in the case of in-plane filled specimen response, where large amounts of energy is first stored due to the constrained deformation of the polymer (simultaneously preventing cell rows from collapsing). Here, the onset of energy dissipation starts with the onset of localized failure (triggered by longitudinal wall tearing). Therefore, numerical models must also incorporate damage/fracture models to accurately model the crush response of filled honeycombs. In this study, smeared crack approach (SCA) was used for the numerical study on the in-plane crush response of filled specimens. The advantage of SCA over other fracture models (such as cohesive zone models) is that, here, the wall tearing site need not be known *a priori*. Instead, the wall tearing site is predicted as an outcome of the simulation.

The ongoing work is focussed on studying the crush response of filled specimen under dynamic loading using a modified wave loading device (WLD) for the axial filled honeycomb response. The experimental results will be used to guide the modeling in order to design a honeycomb materials that has maximum energy absorption.

Bibliography

[1] C. D. Babcock, "Shell Stability," ASME Journal of Applied Mechanics, Vol. 50, pp. 935-940, 1983.

[2] Z. Bažant and B. Oh, "Crack band theory for fracture of concrete," Materials and Structures, Vol. 16, pp. 155-177, 1983.

[3] W.E Baker, T. C. Togami and J.C. Weydert, J. C. 1998, "Static and dynamic properties of high density metal honeycombs," International Journal of Impact Engineering, Vol. 21, No. 3, pp. 149-163, 1998.

[4] D. O. Brush and B. O. Almroth, "Buckling of bars, plates and shells," McGraw-Hill, NY, 1975.

[5] J. Chung and A. M. Waas, "The inplane elastic properties of circular cell and elliptical cell honeycombs," Acta Mechanica, 144 (1-2), pp. 29 - 42, 2000.

[6] J. Chung and A. M. Waas, "Compressive response of honeycombs under in-plane uniaxial static and dynamic loading, Part I: Experiments," AIAA Journal, Vol. 40, No. 5, pp. 966 - 973, 2002a.

[7] J. Chung and A. M. Waas, "Compressive response of honeycombs under in-plane uniaxial static and dynamic loading, Part II: Simulations," AIAA Journal, Vol. 40, No. 5, pp. 966 - 973, 2002b.

[8] J. Chung and A. M. Waas, "Compressive response of circular cell polycarbonate honeycombs under inplane biaxial static and dynamic loading, Part I: Experiments," International Journal of Impact Engineering, 27 (7), pp. 729 - 754, 2002c.

[9] J. Chung and A. M. Waas, "Compressive response of circular cell polycarbonate honeycombs under inplane biaxial static and dynamic loading, Part II: Simulations," International Journal of Impact Engineering, 27 (10), pp. 1015 - 1047, 2002d.

[10] J. Chung and A. M. Waas, "Elastic imperfection sensitivity of hexagonally packed circular cell honeycombs," Proceedings of the Royal Society London, A Mat., 458, pp. 2851-2868, 2002e.

[11] J. Chung and A. M. Waas, "The micropolar elasticity of circular cell honeycombs," Proceedings of the Royal Society London, A Mat., 465, pp. 25-39, 2008.

[12] L. J. Gibson and M. F. Ashby, "Cellular Solids: Structure and Properties," 2nd Edition, Cambridge University Press, 1997.

[13] W. Goldsmith and J. L. Sackman, "An experimental study of energy absorption in impact of sandwich plates," International Journal of Impact Engineering, Vol. 12, pp. 241-262, 1992.

[14] C. Heinrich and A. M. Waas, "Investigation of progressive damage and fracture in laminated composites using the smeared crack appraoch," 53rd AIAA/ASME/ASCE/AHS/ASC Structures, Structural Dynamics & Materials Conference, Honolulu, April 23-26, 2012.

[15] B. Hou, A. Ano, S. Abdennadher, S. Pattofatto, Y. L. Li and H. Zhao, H, "Impact behavior of honeycombs under combined shear-compression. Part I: Experiments," International Journal of Solids and Structures, Vol. 48, pp. 687-697, 2011.

[16] S.-T. Hong, J. Pan, T. Tyan and P. Prasad, "Dynamic crush behaviors of aluminum honeycomb specimens under compression dominated inclined loads," International Journal of Plasticity, Vol. 24, pp. 89-117, 2008.

[17] H. Kolsky, "Stress Waves in Solids," Dover Publications, 2003.

[18] R. K. McFarland Jr., "The development of metal honeycomb energy-absorbing elements," Technical Report No. 32-639, Jet Propulsion Laboratory, California Institute of Technology, 1964.

[19] E.C. Mellquist and A. M. Waas, "Size effects in the compressive crushing of honeycombs," 43rd AIAA/ASME/ASCE/AHS/ASC Structures, Structural Dynamics and Materials Conference, Denver, Colorado, 22-25 April, 2002

[20] E.C. Mellquist and A. M. Waas, "Size effects in the crushing of honeycomb structures," 45th AIAA/ASME/ASCE/AHS/ASC Structures, Structural Dynamics and Materials Conference, Palm Springs, California, 19-22 April, 2004

[21] D. Mohr and M. Doyoyo, "Large plastic deformation of metallic honeycomb: orthotropic rate-independent constitutive model," International Journal of Solids and Structures, Vol. 41, pp. 4435-4456, 2006.

[22] N. Morris, "Use of Lanczos algorithm in elastic stability," Journal of Structural Engineering, Vol. 116, Issue 7, pp. 2049 - 2054, 1990.

[23] A. D. Mulliken and M. C. Boyce, "Polycarbonate and a polycarbonate-POSS nanocomposite at high rates of deformation," ASME Journal of Engineering Materials and Technology, Vol. 128, pp. 543-550, 2006.

[24] M. Ostoja-Starzewski, "Microstructural randomness and scaling in mechanics of materials," Modern Mechanics and Mathematics, Chapman & Hall/CRC/Taylor & Francis, 2008.

[25] S. D. Papka and S. Kyriakides, "In-plane compressive response and crushing of honeycomb," Journal of the Mechanics and Physics of Solids, Vol. 42, No. 10, pp. 1499-1532, 1994

[26] J. G. Rots, P. Nauta, G. M. A. Kusters and J. Blaauwendraad, "Smeared crack approach and fracture localization in concrete," Heron, Vol. 30, No. 1, 1985.

[27] C. W. Schwingshackl, G. S. Aglietti and P. R. Cunningham, "Determination of honeycomb material properties: Existing theories and an alternative dynamic approach," ASCE Journal of Aerospace Engineering, Vol. 19, No. 3, pp. 177-183, 2006

[28] M. Vural and G. Ravichandran, "Dynamic response and energy dissipation characteristics of balsa wood: experiment and analysis," International Journal of Solids and Structures, Vol. 40, pp. 2147 - 2170, 2003.

[29] T. Wierzbicki and W. Abramowicz, "On the crushing mechanics of thin-walled structures," Journal of Applied Mechanics Trans ASME, Vol. 50, pp. 727-734, 1983.

[30] A. Wilbert, W.-Y. Jang, S. Kyriakides and J. F. Floccari, "Buckling and progressive crushing of laterally loaded honeycomb," International Journal of Solids and Structures, 48, pp. 803-816, 2011.

[31] E. Wu and W.-S. Jiang, "Axial crush of metallic honeycombs," International Journal of Impact Engineering, Vol. 19, Nos. 5-6, pp. 439-456, 1997.

[32] Z. Xue and J. W. Hutchinson, "Crush dynamics of square honeycomb sandwich cores," International Journal for Numerical Methods in Engineering, Vol. 65, pp. 2221-2245, 2006.